Dimensional Stability in Compression-Moulded Discontinuous Long Fibre Carbon/PEEK Composites

Caroline COLLINS

Department of Mechanical Engineering

MCGILL UNIVERSITY, MONTREAL

April 2018

A Thesis Submitted to McGill University in partial fulfilment of the requirements of the degree of Master of Engineering

© Caroline Collins, 2018

Abstract

There is growing interest within the aerospace industry regarding the use of Discontinuous Long Fibre (DLF) composites. Composed of randomly-oriented strands of chopped unidirectional pre-impregnated tape, these materials have been used to produce intricate, net-shape parts with complex features – replacing complicated metallic brackets with single, lightweight parts. DLF material has also proven its ability to maintain relatively high stiffness, particularly when made with advanced engineering thermoplastic matrices, like Polyether-ether-ketone (PEEK).

Carbon/PEEK DLF composites suffer from problems with warpage driven by their high processing temperatures. Cooling from high temperature generates high residual stress due to the mismatch in thermal expansion between fibre and matrix and the crystalline shrinkage of the matrix. Past research has focussed on the processing and mechanical properties of these composites, as warpage was not a critical deterrent in making compact, bulky parts using DLF material. As such, little is understood about the generation of residual stresses within DLF thermoplastic-matrix composites. To pursue the production of thin-gauge parts using compression moulded DLF, warpage must be better understood. The presented work aims to characterize warpage, and pursue means of mitigating warpage, in DLF composites through experimentation and simulation.

The first objective – warpage characterization – was pursued by making a series of thin, flat plates under consistent processing conditions. Trends between strand size used, plate thickness, and warpage were compared between small 101.6 mm x 101.6 mm plates and large 304.8 mm x 355.6 mm plates. It was apparent that the magnitude of warpage decreased with increasing strand size and was, in general, lower when smaller strands were used. The shape of the warped parts varied significantly between parts, indicating that the material orientation had a significant impact on final warpage. As well, there was not a clear relationship between warpage seen in small panels compared to large panels. A preliminary simulation of the applied process cycle for the 101.6 mm x 101.6 mm plates was created, incorporating temperature-dependent modulus properties and temperature-dependent part shrinkage. This simulation yielded similar trends to those seen experimentally, but did not replicate true warpage magnitude.

As a second objective, the introduction of small ribbed features to the thin, flat plates was explored as a means of mitigating warpage by increasing part stiffness. First, the trade-offs between rib dimensions, overall part weight, and part stiffness were observed. Then fill conditions and processing conditions were refined to produce parts with fully-filled ribs and visibly good surface finishes. Finally, parts incorporating evenly-spaced ribs running orthogonal to each other were assessed to determine the impact of small rib features on part warpage. There was not a significant impact on the magnitude of warpage within parts. However, the addition of ribs helped to control the warped shape of the part, with the same warpage pattern seen within fully supported sections of all manufactured ribbed panels.

Overall, it was found that warpage is significant within thin-gauge carbon/PEEK DLF parts and that the shape of the part warpage was highly varied. Warpage appeared relatively stable, levelling out below 0.01 mm of out-of-plane deviation per mm of part length for parts made with 6.35 mm x 3.18 mm strands at thicknesses greater than 2 mm. For thinner parts and parts made with larger strand sizes, warpage will be more significant. To pursue compression moulding with DLF carbon/PEEK material, the high degree of warpage must be understood. For part applications where dimensional stability is a critical factor, stiffening features like ribs, or stabilizing features like joints should be incorporated into the part design to better control final part shape.

Sommaire

L'industrie aérospatiale s'intéresse de plus en plus à l'utilisation de matériaux composites à fibres longues discontinues (FLD) afin de remplacer des pièces métalliques complexes. Ce matériau est composé de copeaux de ruban unidirectionnel préimprégné qui sont orientés de manière aléatoire. Ce matériau a également prouvé sa capacité à maintenir une rigidité relativement élevée, en particulier lorsqu'il est fabriqué avec des matrices thermoplastiques, comme le polyéther-éther-cétone (PEEK). Les copeaux à orientation aléatoire utilisées dans ces pièces contribuent à leurs nombreux avantages - leur excellente formabilité, leurs propriétés relativement isotropes et leur potentiel pour des temps de mise en œuvre courts. Cependant, cette méso-structure hétérogène crée également des défis, en particulier pour produire des pièces plats et minces.

La stabilité dimensionnelle est un défi pour toutes pièces composites, en raison de leur anisotropie inhérente et de la grande différence entre les coefficients de dilatation thermique dans les directions de la fibre et de la matrice. Les composites à matrice thermoplastique font face à des niveaux plus élevés d'instabilité dimensionnelle, en raison des contraintes résiduelles supplémentaires générées par des températures de mise en œuvre élevées et un retrait causé par la cristallisation de la matrice. Lorsque l'on considère la méso-structure intrinsèquement hétérogène des composites FLD, la déformation des pièces pose un défi complexe. Ce phénomène n'a pas été très étudié parce que les pièces composites FLD sont typiquement à paroi épaisse. Pour produire des pièces à paroi minces, la déformation doit être mieux comprise. Les travaux de cette thèse visent à caractériser la stabilité dimensionnelle des composites carbone / PEEK FLD et de diminuer le gauchissement des plaques en augmentant localement leur rigidité.

Le premier objectif, le gauchissement des pièces planes et minces a été mesuré expérimentalement et calculé par des méthodes numériques. Pour des conditions de moulage constantes, les effets de la taille des copeaux et l'épaisseur de la plaque sur le gauchissement ont été étudiés pour des petites plaques de 102 mm x 102 mm et des grandes plaques de 305 mm x 356 mm. De façon générale, le gauchissement diminue avec l'augmentation de l'épaisseur des pièces et la diminution de la taille des copeaux. La géométrie du gauchissement était aléatoire ce qui est relié à la distribution aléatoire des copeaux. Une simulation préliminaire pour prédire le gauchissement des petites plaques est également présentée. En prenant compte de la variation des propriétés du matériau en

fonction de la température, les simulations reproduisent les tendances observées expérimentalement.

Le deuxième objectif, de petites nervures ont été incorporées sur des plaques minces. Tout d'abord, les relations entre les dimensions des nervures, le poids total des pièces et la rigidité partielle seront observés. Ensuite, les conditions de remplissage et les conditions de mise en œuvre ont été définies pour produire des pièces avec des nervures entièrement remplies et un bon fini de surface. Enfin, les parties incorporant des nervures régulièrement espacées ont été évaluées pour déterminer l'impact des nervures sur le gauchissement des pièces. Il n'y avait pas d'impact important sur l'amplitude du gauchissement. Cependant, l'ajout de nervures a contribué à contrôler la forme de la déformation de la pièce, avec le même motif de déformation observé dans les sections entièrement supportées de tous les panneaux nervurés fabriqués.

Enfin, ce travail montre que le gauchissement est important pour les pièces en carbone / PEEK FLD minces et que la géométrie du gauchissement est très variable. Ce dernier est relativement stable avec une valeur de 0,01 mm par mm de longueur de pièce contenant des copeaux de 6,35 mm x 3,18 mm et d’épaisseur supérieure à 2 mm. Pour les pièces plus minces et les pièces faites avec des tailles de copeaux plus grandes, le gauchissement sera plus important. Afin de pursuivre l’amélioration du procédé de moulage par compression avec un matériau carbone / PEEK FLD, une compréhension approfondie des mécanismes de déformation est nécessaire. Dans les applications où la stabilité dimensionnelle est un facteur critique, des éléments raidisseurs telles que des nervures ou des éléments stabilisants comme des joints doivent être incorporés dans la conception de la pièce pour mieux contrôler sa forme finale.

Acknowledgements

The work presented in this thesis would not have been possible without the financial support provided by the Consortium for Aerospace Research and Innovation in Canada (CARIC), the Consortium for Research and Innovation in Aerospace in Quebec (CRIAQ) and industrial partners: Pratt and Whitey Canada Corp., Hutchinson Aerospace & Industry Ltd, and Dema Aeronautics. I would also like to thank CREPEC: Research Centre for High Performance Polymer and Composite Systems for their support.

Many thanks go out to the facilities which provided equipment for manufacturing as well. Thank you to the Aerospace Manufacturing Technologies Centre of the National Research Council, especially Hugo Laurin, for access to and assistance with the 150 ton Wabash press used to make the large DLF panels. As well, thanks are due to McGill's Additive Manufacturing Lab and the Hutchinson Aerospace & Industry Ltd. Quality department for their assistance in providing inspection equipment.

I would also like to thank Benoit Landry, Dominic LeBlanc, Gilles-Philippe Picher-Martel, and Marina Selezneva for their work designing the instrumented hot press, developing appropriate processing conditions for making defect-free flat plates, and demonstrating the viability of using DLF carbon/PEEK to make complex parts. Without their efforts to further the understanding of DLF composites, the motivation for this thesis would not exist.

As well, I would like to thank all of my colleagues in the Structural and Composite Materials Lab for their advice, support, and friendship throughout my time as part of the lab. In particular, I would like to acknowledge the help and support provided by Lucie Riffard who always kept the lab running smoothly; the leadership and insightful discussion provided by Adam Smith who repeatedly goes out of his way to help his colleagues; the assistance of Linus Lehnert who generously transported parts between the McGill campus and Hutchinson Aerospace & Industry Ltd for assessment; and the comradery of Julieta Barroeta-Robles, Natassia Lona Batista, and Sanesh Iyer. All of these individuals made my experiences at McGill truly enjoyable.

Above all, I would like to thank my supervisor, Professor Pascal Hubert, for all of his guidance and support throughout the project. I was truly lucky to have been a part of his lab.

Preface and Contribution of the Author

The work presented herein was fully carried out by the author, building on the contributions of past students in the following sections:

- Sections 2.1 and 2.2 utilized tooling, equipment, and processing cycles developed in the COMP-412 project by Benoit Landry, Gilles-Philippe Picher-Martel, and Dominic LeBlanc. The instrumented hot press and processing conditions used to make the small panels in Section 2.1 were the same as those presented in Benoit Landry's doctoral thesis. As well, the large panel mould and moulding conditions used in Section 2.2 were those presented in both Benoit Landry's and Marina Selezneva's doctoral theses.

  Some of the panels in this chapter were scanned by technicians at Hutchinson Aerospace & Industry Ltd, using their FaroArm.

- The ABAQUS model built in Section 2.3 stemmed from a number of past students' work. The thermal model grew from work performed by Nicolas Ohlmann during a summer internship. Assumptions that he made for flow within the cooling channels were utilized. The strand layups used as material inputs were generated using the same code that Marina Selezneva developed for her predictive mechanical property models in her doctoral thesis. The material models for temperature-dependent modulus and shrinkage properties were taken from the thermomechanical models developed by Benoit Landry in his doctoral thesis.

Table of Contents

List of Figures

List of Tables

1. Introduction

1.1 Motivation

As described by Peel, there are four key performance drivers in the aerospace industry: total cost, passenger safety, environmental initiatives, and overall aircraft performance, including potential payload [1]. The last of these two of these drivers – aircraft performance and environmental initiatives – motivate increased usage of advanced composite materials in aircrafts as a means of weight reduction – to improve potential flight ranges and reduce fuel consumption. This shift towards composite materials can be seen in recent commercial aircrafts, such as the Boeing 787 Dreamliner [2] and Airbus A350 XWB [3], which boast that their primary airframes are composed of at least 50% advanced composites by weight. Additionally, the Bombardier C-Series, which advertises itself as being 12 000 lb lighter than competing 100- to 150-seat aircrafts [4], attributes 2000 lb of this weight reduction to their use of advanced composite materials [5].

The usage of composite materials in these aircrafts is dominated by primary structures, such as the fuselage and wing surfaces. Hundreds of load-bearing components – including clips, hinges, and brackets – remain metallic [6]. Some parts with relatively simple geometries, like the clips used to attach fuselage panels to its frame (see Figure 1), are beginning to be replaced with thermoformed thermoplastic-matrix composites as they have been in the Airbus A350 XWB [7, 8]. Unfortunately, this process creates significant waste from the offcuts of preformed sheets and final part trimming. As well, it cannot effectively replace complex geometry components, such as those with rib-like features, thickness changes, and holes.

(a) (b)

Figure 1: Thermoformed thermoplastic (a) “Auto-Stabilized” clip and (b) “Cleat” used to attach the composite fuselage of the Airbus A350 to its frame [8].

Many complex components continue to be machined out of steel such as that shown in Figure 2(a) – using expensive CNC-machines, creating significant material waste, and adding weight to the aircraft. Alternately, components may be composed of many smaller parts, such as the aluminum part shown in Figure 2(b) – creating material waste for each machined part and a need for additional fasteners. The added fasteners both increase weight and reduce assembly efficiency. Both examples are expensive, particularly in terms of time and material waste.

(a) (b)

Figure 2: (a) Complex, CNC-machined steel aircraft hinge by UDASH [9] and (b) Rendering of multi-component aluminum aircraft bracket [10].

To form complex parts, a discontinuous bulk moulding compound composed of chopped strands of pre-impregnated composite tape has proven to be useful. This material is sometimes referred to as Randomly Oriented Strands (ROS), discontinuous carbon fibre platelets, chips, flakes, strands, long discontinuous fibres (LDF), or, for the purposes of this thesis, Discontinuous Long Fibres (DLF). When combined with compression moulding, DLF presents an opportunity for replacing complex metallic components with single, lightweight, near-net-shape moulded components, as pictured in Figure 3. The success of this method has been demonstrated by a number of authors including van Wijngaarden [11], Howell [12], and Eguémann [13].

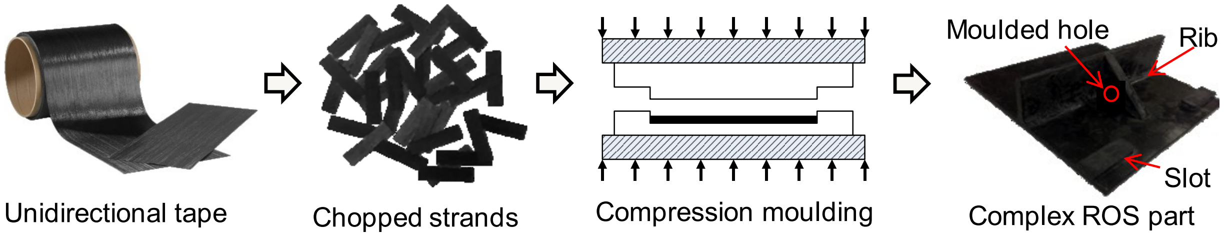

Figure 3: Manufacturing process for DLF parts taken from [14].

Demand for compression-moulded DLF composites – otherwise known as LDF, ROS, platelet, or chopped carbon fibre tape-reinforced thermoplastics (CTT) – is growing in the aerospace industry and manufacturers like TenCate [15] and Greene, Tweed [10, 16] have demonstrated its potential for commercial use. One such example is the Xycomp® bracket presented by Greene in [10] as a 43% lighter, single-piece replacement for the three-part aluminum assembly shown in Figure 2(b). The DLF carbon fibre/Polyether-ether-ketone (PEEK) bracket, made with moulded-in holes and an over-moulded metal insert, is pictured alongside the original assembly in Figure 4. In creating this near net-shape part as one piece, manufacturing time is significantly reduced, thus fulfilling a third key performance driver – cost reduction.

(a) (b)

Figure 4: Industry example of DLF part replacing assembly showing (a) concept and (b) final part [10].

DLF composite parts act as a compromise between high strength, but difficult-to-form continuous fibre composites and weak, but easily formable short strand composites [10, 17]. By using chopped strands of unidirectional pre-impregnated tape, a high fibre volume fraction is preserved, so parts maintain a relatively high stiffness [17]. The reduced fibre length provides sufficient formability for the creation of intricate net-shape parts with complex features like thickness variations, tight radii, holes, and ribs [10, 17], as seen in the example pictured in Figure 4, above. As well, the incorporation of a thermoplastic matrix has added benefits over a thermoset matrix in its production efficiency and performance. In terms of production, when using manufacturing techniques like compression moulding, parts are produced with relatively short processing times and create minimal waste [12, 16]. Regarding performance, thermoplastic parts typically have superior impact, moisture, and corrosion resistance [12, 16] when compared to parts with thermoset matrices. As well, they can withstand relatively high operating temperatures [16], can be welded, and are more easily recycled [18]. PEEK, specifically, is also very chemically resistant [19]. The research presented in this thesis will focus on thermoplastic-matrix DLF composites, specifically those made with carbon fibre in a PEEK matrix.

1.2 Challenge

DLF compression moulded composite parts have shown their value and are beginning to be recognized in the aerospace industry. The randomly-oriented chopped strands in these composites contribute to their many advantages - their excellent formability, their relatively isotropic properties, and their potential for short processing times. However, the random distribution of strands also means that parts are created differently every time. Of course, the in-plane orientation of strands is uncontrolled and varies part-to-part, but out-of-plane orientation is also uncontrolled. Due to the strand geometry and distribution method, strands clump, creating waviness, pockets of resin between strands, and out-of-plane orientation in some strands, as seen in Figure 5. Altogether, there can be significant variation in final part properties.

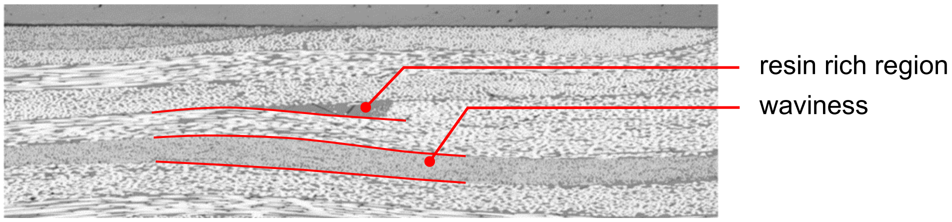

Figure 5: Cross-section of DLF composite plate, highlighting inconsistencies in fibre placement (micrograph taken from [17]).

A few researchers have investigated the processing conditions of DLF parts – using numerical models to assess compaction pressures for eliminating interstrand voids [20], fluid-structural models to assess the interactions between chopped strands during compaction and their transition from a compressible to incompressible medium [21], computational models to characterize the squeeze-flow behaviour of the moulding compound during melt processing [22], and temperature-dependent stress simulations to determine necessary cooling pressures for manufacturing parts free of surface voids [17]. A few researchers have assessed the final part structure as well – using micrometer scale computed tomography (MicroCT) to determine final microstructure in the part [23, 24] and developing methods for measuring strain during high temperature testing [25]. The most common focus of researchers is on understanding how this randomization of strands affects mechanical properties. Authors have concentrated on characterizing the variability in mechanical properties of thermoplastic [14, 26-28] and thermoset-matrix [29-31] DLF parts, and explored means of reducing variability by using specialized “ultra-thin” strands [27, 28, 32], using existing pre-formed sheeting [33], or by introducing labor-intensive strand distribution methods to create preformed sheets of random material [26, 28, 31, 32]. Efforts to pursue predictive models for the elastic moduli [27, 34, 35], strength, and failure mechanisms [36] seen in DLF parts, or stiffness and strength of similarly discontinuous composites with high fibre volume fractions [37, 38], have also been prevalent. However, there is little understanding of how the heterogeneous meso-structure of DLF composites affects dimensional stability of the final part. Selezneva indicates that an undesirable out-of-plane deflection, or warpage, presents itself as a prominent defect in the carbon fibre/PEEK DLF plates that were manufactured in [14]. However, there is still much to understand about residual stress development, and the resulting warpage of DLF composites. The following literature review will focus on efforts that have been made to understand residual stress generation and resulting warpage in composites in general.

1.3 Literature Review

It is generally understood that advanced composite materials suffer from residual stress generation due to their inherent anisotropy and interactions with tooling [39]. The effect of these residual stresses is twofold – they reduce mechanical properties [40-42] and create dimensional instability [40, 43]. This literature review will discuss the levels of residual stress, as described by Parlevliet et al [43], common to continuous-fibre composites. The specific sources of residual stress in thermoset and thermoplastic-matrix composites and their implications for the dimensional stability of continuous-fibre parts will then be discussed. As DLF lies partway between a continuous-fibre and short-fibre composite, review of the residual stress generation and resulting warpage in injection-moulded, short-fibre thermoplastic-matrix composites will follow.

1.3.1 **Levels of Residual Stress in Continuous Fibre Composites**

1.3.1.1 Micro-Mechanical Stresses

The first level of residual stress is that generated on a micro-mechanical level, directly between the fibres and matrix. The fibres are relatively dimensionally stable. Using carbon fibre as an example, the coefficient of thermal expansion in the fibre is very small, on the order of $10^{-7}\epsilon/°C$ [41], and slightly negative along the length of the fibre. Radial to the fibre, the CTE is similarly small, but positive. Relative to the fibre, the matrix – be it thermoset or thermoplastic – is prone to shrink more significantly than the fibre from thermal expansion as the part cools [43, 44], from cure shrinkage (in the case of a thermoset matrix) [44], and from matrix crystallization (in the case of a semi-crystalline thermoplastic matrix) [43]. So, the fibres end up under compression – both radially and longitudinally – and the matrix ends up in tension, as depicted in Figure 6.

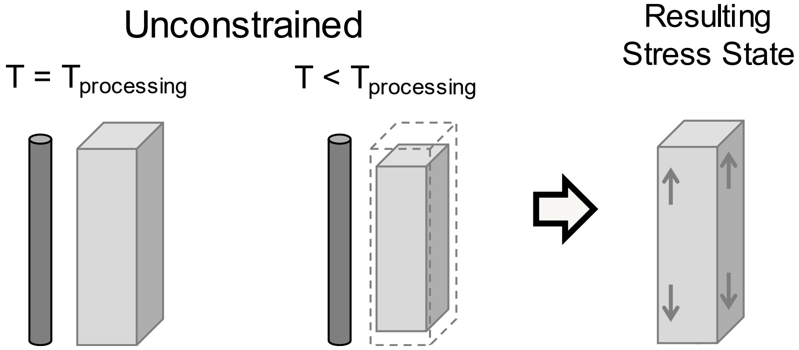

Figure 6: Generation of micro-mechanical stress, adapted from [43].

The stress induced by micromechanical interactions is highly variable, even within a single ply, because individual fibres are not perfectly straight, uniform, and evenly spaced. This variation is difficult to address and often neglected [44]. From a thermoset standpoint, Johnston indicates that micromechanical residual stresses are typically small and balance each other out between laminae [44]. Speaking of thermoplastic-matrix composites, Parlevliet et al indicate that significant residual strain may be generated along the length of the fibre, and relatively low residual strain is generated radial to the fibre. The high longitudinal strain necessitates a strong bond between the fibre and matrix to prevent fibre buckling, interface de-bonding, and micro-cracking [43], but the effect that micro-mechanical stress on its own has on part warpage has not been explored. The radial residual strains allow for the transfer of stress between the fibre/matrix interface but do not significantly contribute to residual stress within the composite [43].

1.3.1.2 Macro-Mechanical Stresses

In a continuous fibre composites, macro-mechanical stresses form between laminae. Just as the matrix surrounding an individual fibre tow will shrink more than the fibre, the matrix-dominated direction of a continuous-fibre lamina will shrink more than the fibre-dominated direction [43]. When restrained by adhesion to another lamina of opposing fibre direction, tension will develop in the transverse direction of the lamina, promoting the part curling around that lamina's longitudinal direction. In the case of a flat, [0/90] laminate as pictured in Figure 7, these macro-mechanical stresses have shown to create bi-stable laminates that curl around the fibres of one ply at rest, and around the fibres of the opposite ply if attempted to be bent [45].

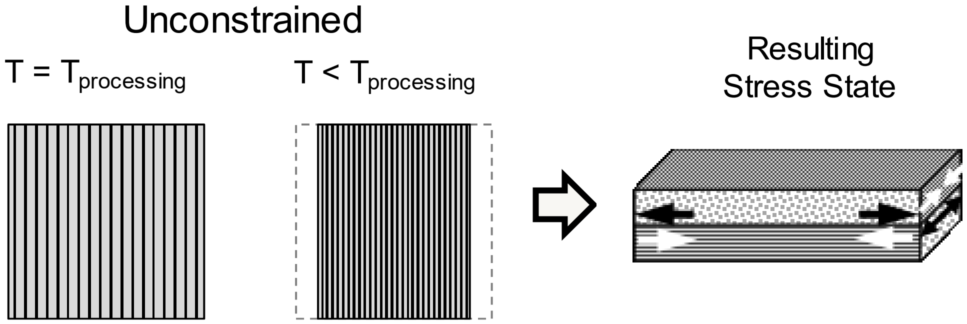

Figure 7: Generation of macro-mechanical stress, adapted from [43].

Macro-mechanical stresses are considered to be a significant fraction of residual stress, contributing to dimensional instability and mechanical failings. For simplicity in modelling, many assume them to be the dominant residual stress, effectively acting as an average of the micro-mechanical stresses in each ply [44].

1.3.1.3 Global Stresses

Global residual stresses are those that act on the part as a whole. One potential source of global stress would be a thermal gradient in the part. For thermoset-matrix composites, thermal gradients are be induced by heat generated from the chemical reaction of polymerization during cross-linking (cure) [44, 46]. Bogetti and Gillespie studied this phenomenon on a series of glass/polyester laminates. Thin laminates heat quickly, initiating cure throughout the part. Further heat generated from cure is relatively well distributed and the thermal gradient is small. As thickness increases, the gradient can increase, with the most heat generated at the centre of the part, where heat from the exothermic reaction of cross-linking is not easily dissipated. This effectively initiates cure from the centre outwards, stiffening at the centre and putting the external surfaces of the part in tension. In the study by Bogetti and Gillespie, this occurred at a thickness of 2.54 cm. Thicker laminates, in this study 5.08 cm thick or thicker, take longer to heat through their thickness. So, the external surfaces may become hot enough to initiate cure during heat-up before the centre of the laminate does. In this situation, the thick laminates cure from the outside in, locking stress in place at the exterior surfaces and putting the centre in tension. The full progression from temperature gradient to degree of cure to residual stress distribution in thick glass/polyester laminates, as presented in [46], is shown in Figure 8. This figure emphasizes that the thermal gradient within the part changes significantly with part thickness in thermoset composites.

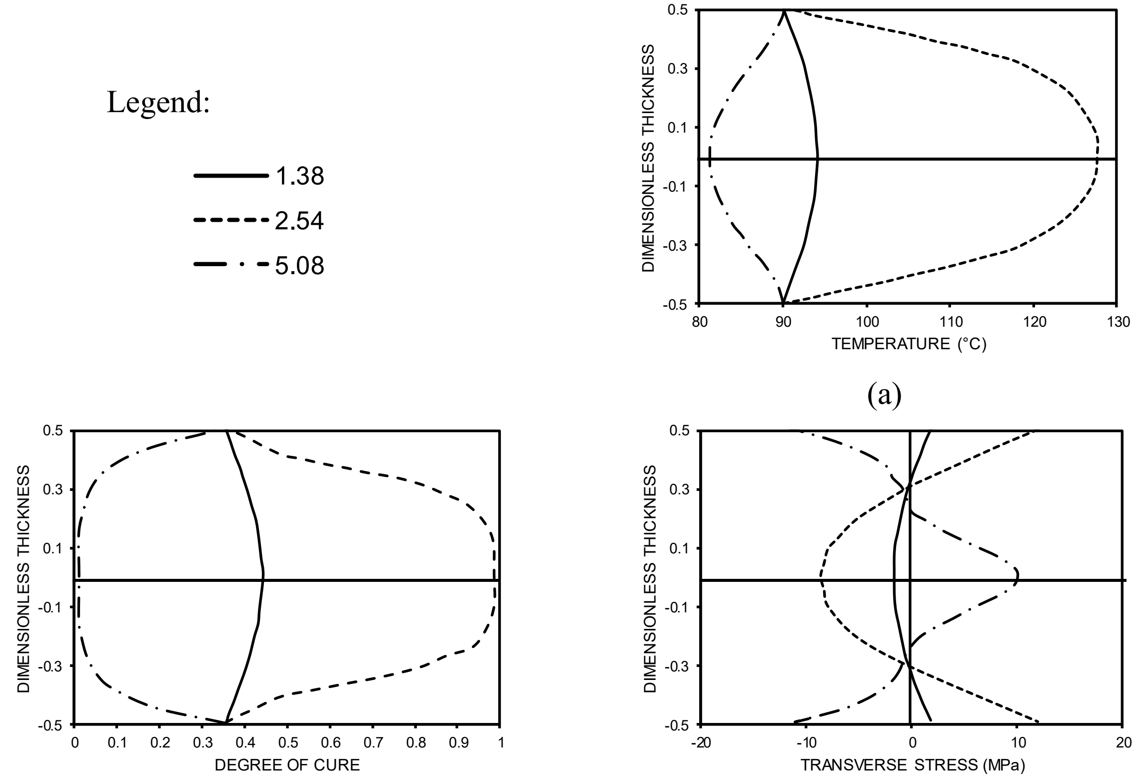

(a)

(b)

(c)

Figure 8: Effects of thermal gradients in 1.38 cm, 2.54 cm, and 5.08 cm thick glass/polyester laminates, showing (a) Temperature distribution 164 minutes into the prescribed cure cycle; (b) Resulting degree-of-cure distributions at 164 minutes; (c)Final residual stress generation, adapted from [46]. Legend identifying panel thicknesses can be seen in the top left corner of this figure.

Similarly for thermoplastic-matrix composites, thermal gradients are generally not considered to develop in thin laminates [43], unless there are in-plane thermal gradients generated from interactions with the mating tool. For thick laminates, through-the-thickness temperature gradients may develop, particularly if a part cools too quickly. The exterior surfaces may cool first, crystallizing to lock in stresses at the surface before heat has fully dissipated from the centre. As the part fully solidifies, the stress distribution would resemble that shown in Figure 9 [43].

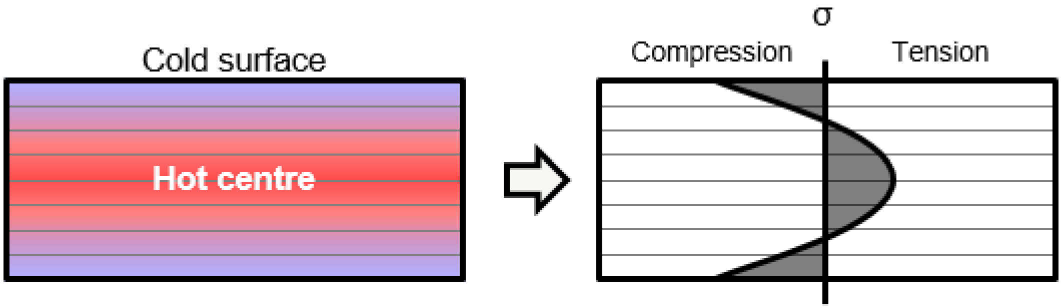

Figure 9: Residual stress distribution in thick, thermoplastic-matrix part cooling from external surfaces first, adapted from [43].

Another source of global stress is tool-part interaction. In a vacuum-bagged application, further thermal gradients may be introduced into the part as the bagging, bleeder, and breather layers inhibit heat dissipation, and metallic tool plates will conduct heat away from the part [44]. As well, friction between the tool plate and the part can create shear stress as the tool and part have different CTEs and will grow and shrink at different rates [44, 47]. If the tool has a higher CTE than the part, it can stretch the ply in contact with it during heat-up, and lock shear stresses in during cure [39]. Figure 10, taken from Twigg et al, shows the mechanism and effect of tool-part interaction for thin, 0° carbon/epoxy laminates of varying length. For the displayed case, the effect is greatly apparent because the laminate consists of only four plies and as such did not have sufficient stiffness to resist the incurred residual stresses.

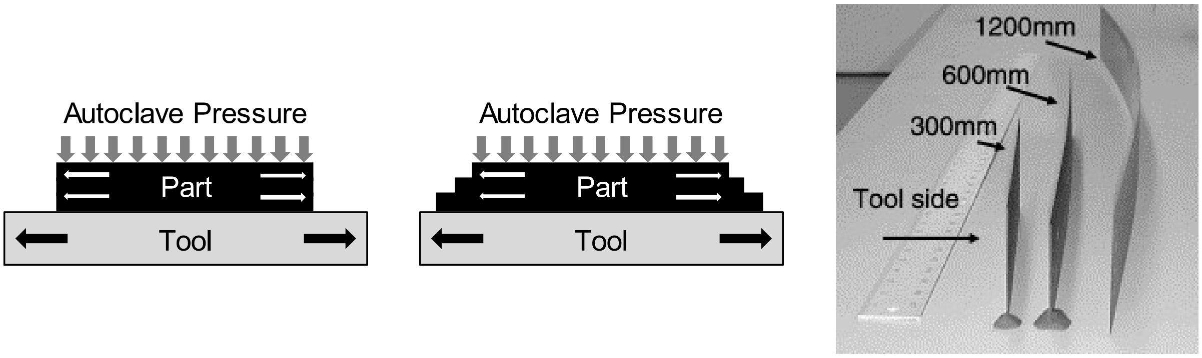

(a) (b) (c)

Figure 10: Warpage from tool-part interaction, showing (a) Tool expanding as it heats up, inducing tension in part, (b) Ply-slippage to relieve stress between plies and cure, and (b) Resulting deformation in $[0^\circ_4]$ carbon/epoxy laminates, taken from [39].

If the part cures or solidifies while cooling, the resulting shear stress from the faster-shrinking tool plate can compress the plies in the layer contacting the tool plate, inducing fibre waviness [43].

For other manufacturing methods, such as compression moulding, the effects of tool-part interaction can become more complex. For example, using rubber stamp moulding with a matching metallic die, could significantly impact the formation and distribution of residual stresses because each side will dissipate heat differently and has a different coefficient of friction [43]. Additionally, constraining the part within a cavity adds additional normal stresses [44], as illustrated in Figure 11.

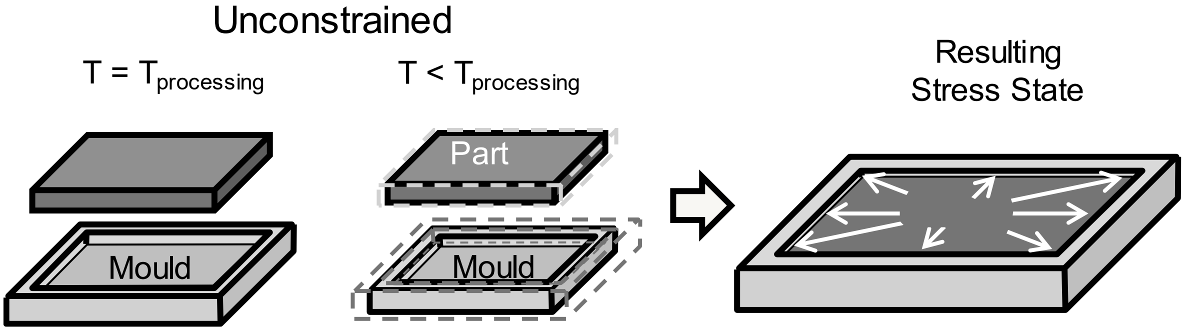

Figure 11: Generation of global stress from tool-part interaction and part constraint.

While residual stresses can be considered on these three different levels, in reality, they all interact and contribute to each other. The thermal distribution within the part affects how the matrix shrinks, in turn affecting the macro- and micro-mechanical stress distributions. The next sections will explore how residual stress generation differs in thermoset and thermoplastic-matrix composites.

1.3.2 **Residual Stress in Continuous-Fibre Thermoset-Matrix Composites**

The adverse effects of residual stress on mechanical properties and dimensional stability motivated the investigation of residual stresses in thermoset composites, with early publications by Hahn [48, 49] and Daniel and Liber [50-52] emerging in the mid 1970s [40]. From years of study, the sources of warpage in continuous-fibre thermoset-matrix composites are well understood, and have been classified into two distinct groups – intrinsic and extrinsic.

Intrinsic properties include part geometry – laminate thickness, ratio between laminate length and width, and lay-up – and material properties [47] – resin shrinkage, resin viscosity, and prepreg age [39]. Extrinsic properties are specific to the tooling used – coefficients of friction and expansion – and the processing conditions employed [47] – rate and magnitude of applied pressure and temperature [39]. Each level of residual stress is driven by both intrinsic and extrinsic factors. When considering micro-mechanical stresses, the difference in shrinkage between fibre and matrix is of course linked to the intrinsic material properties – the difference in CTE of the materials. The extrinsic processing conditions employed affect the overall matrix shrinkage. In addition to shrinking from cooling, thermoset resins shrink as they cure. The van der Waals bonds between resin molecules are replaced with shorter co-valent bonds as the resin cross-links, and the resin effectively shrinks [44]. The cure cycle employed controls the temperature at which the matrix cures, which is effectively the point at which residual stresses start to build. The temperature difference between this point and ambient temperature impacts the level of residual stress developed from the CTE mismatch between fibre and matrix. The cure cycle employed also affects the degree of cure of the resin – how much cure shrinkage there is and how well it resists residual stresses. On a macro-mechanical level, the same driving forces are present, with the additional intrinsic source – lay-up.

Global residual stresses are impacted by both intrinsic and extrinsic parameters as well. The part shape and thickness affect the temperature distribution within the part. Thicker parts are stiffer and better withstand residual stresses [39], but greater residual stresses are generated within thick parts because of the large thermal gradients [46]. Processing-induced residual stresses have been found to significantly increase with increasing thickness [46].

The interaction between intrinsic material properties and processing parameters creates complexity in the understanding of residual stresses. For example, in some cases, lower cure temperatures were found to reduce residual stresses, as the effects of thermal expansion were reduced. As well, shorter cure cycles have been shown to reduce residual stress. So, a conflict arises because lower cure temperatures typically require longer cure cycles [47]. To better understand residual stress development in thermoset composites, Albert and Fernlund performed a comprehensive study, varying both intrinsic and extrinsic parameters to determine their impact on final part warpage [47]. For the autoclave-manufactured, carbon/epoxy, angled laminates made in this study, the factors with the highest impact on part warpage were found to be the friction of the tool surface, the part geometry (thickness and length), and the cure cycle employed. The tooling material – and effectively the tooling CTE – also had a noticeable impact on part warpage [47]. As this study was specific to one material and set conditions, the authors warn against translating its findings directly to another material [47]. However, it clearly highlights the significant impact from tool-part interactions and cure cycle on final part warpage.

Comprehensive predictive models, accounting for laminate cure kinetics of thermoset resins and thermal gradients within parts were created as early as 1990, as documented in the work by Bogetti and Gillespie [46]. In this model, Bogetti and Gillespie predicted residual stress in thin and thick thermoset-matrix laminates, with good correlation to experimental results. An increasingly comprehensive model, incorporating resin flow during processing and its implications on uneven curing, as well as tooling properties and tool-part interactions, was developed in the 1990s by Johnston [18] and Hubert [53], resulting in the now commercially available software, COMPRO®, produced by Convergent Manufacturing Technology. When coupled with the Convergent software, RAVEN®, for modelling cure kinetics, full-scale composite cure process models can be developed, such as those presented by researchers at NASA in [54]. Between years of experimental investigation and model development, residual stress generation and warpage development in thermoset-matrix composites is well understood.

1.3.3 **Residual Stress in Continuous-Fibre Thermoplastic-Matrix Composites**

Investigation into thermoplastic residual stresses began increasing in interest in 1983/1984 with work done by Cogswell [40]; however, there is still a gap in the understanding of residual stress in thermoplastic matrix composites, compared to thermoset, with most studies focussing solely on PEEK matrices [43].

The driving factors behind warpage in thermoplastic-matrix composites are similar to those in thermoset-matrix composites, but the differences in matrix processing lead to different challenges. While thermoset matrices harden from curing, thermoplastic matrices melt and solidify. They can be re-melted and re-solidified, but this repeated cooling can change the matrix properties and alter the level of residual stress [55]. As well, thermoplastics are typically processed at higher temperatures, which can significantly increase the impact of the matrix CTE on residual stress [40, 41, 56], and also makes it difficult to accurately measure the thermo-mechanical properties of the matrix [40]. For example, some authors believe from observation that 75% of residual stress in carbon/PEEK builds up between its glass-transition temperature (T_g) and room temperature [40]. Conversely, other studies have found that residual stresses build up linearly, above and below T_g [55].

To add additional complexity, thermoplastic matrices can be amorphous or semi-crystalline. Amorphous matrices allow for the relaxation of residual stresses during cooling, until the matrix is below T_g. So, for an amorphous matrix, slow cooling is preferential to provide sufficient time for stress relaxation [43]. In semi-crystalline thermoplastics, a fraction of the matrix becomes densely packed in a crystalline structure, creating significant matrix shrinkage [43] and stiffening the matrix to lock in residual stresses [55]. Thermoplastic matrix properties are heavily dependent on processing conditions – with sites of crystalline nucleation, crystallization temperature (T_c), and crystalline fraction, all depending on the duration that the material is held at any given temperature. Slow cooling rates are believed to promote nucleation of crystallization at the fibre surface, creating a "trans-crystalline" region around the fibre to improve static and fatigue properties, but increase radial stresses in the fibre. This has an unknown impact on part warpage [43]. The peak crystalline temperature is believed to significantly contribute to residual stress and warpage, as this is the point where stresses begin to be locked in [56]. So, its variability with processing condition can have a significant impact. Higher cooling rates generally result in lower peak crystallization temperatures [43], and thus lower matrix shrinkage and warpage. At the same time, higher cooling rates generate lower crystalline fractions, which again contributes to lower matrix shrinkage [43]. The trade-off is that lower crystallinity content correlates with lower mechanical properties. So, each composite material and layup needs its own processing cycles designed to yield best mechanical properties and lowest warpage [43].

So, while it is believed residual stresses in thermoplastic-matrix composites can be modelled in a similar fashion to those in thermoset-matrix composites, taking into account their temperature-dependent properties, this modelling is limited by the availability of reliable data and thermomechanical models for thermoplastic matrices [40].

Considering global residual stresses, thermoplastic composites are similar to thermosets in that residual stress development from thermal gradients is most significant for thick laminates [43]. Unlike thermoset composites, thermoplastics can be annealed to relax these stresses [43]. Regarding tool-part interaction, thermoplastic composites are presumed to react similarly to thermosets, but limited work has been done to investigate these impacts [43].

1.3.4 Residual Stress in Injection Moulded, Thermoplastic Parts

Warpage is a common problem in injection moulded parts as well, whether they are made with neat, unfilled thermoplastics or thermoplastics filled with short fibres. In both cases cooling gradients, mould designs, and process conditions are attributed to creating uneven part shrinkage, resulting in warpage [57, 58]. Of course, material properties and, in fibre-filled plastics, fibre-orientation affect warpage as well[58].

One main difference between warpage generated in continuous-fibre parts and injection-moulded parts is the filling process. Filling creates a flow front within the part, resulting in part anisotropy, with the molecules of the polymer matrix aligned in the direction of filling [57]. The molecules shrink more along the direction of their alignment, so the overall part sees shrinkage predominantly in the fill direction [57, 59]. With this material anisotropy, pure thermoplastics are subject to warpage from processing parameters. Geometric asymmetry, non-uniform thicknesses, and processing conditions induce thermal gradients within the part, inducing residual stresses [57]. So, introducing fibres into injection moulded parts creates further complications with part warpage. The fibres align in the direction of the fill, restricting shrinkage in the flow direction and creating predominantly transverse shrinkage [57]. The shrinkage patterns for filled and unfilled injection moulded thermoplastics are captured in Figure 12.

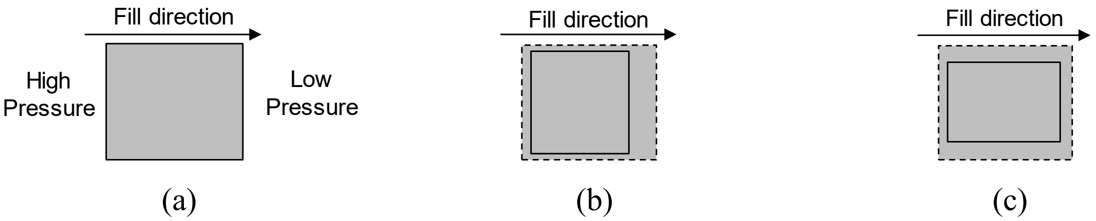

Figure 12: Shrinkage of unfilled and filled injection-moulded, thermoplastic materials showing (a) Fill direction and resulting areas of high and low pressure, (b) Shrinkage of unfilled thermoplastic due to molecules aligning in fill direction; and (c) Shrinkage of filled thermoplastic due to fibres aligning in fill direction [57].

For thin, flat, injection-moulded parts, the relationship of fibres to warpage is relatively straightforward. In [59], the author explores the level of warpage generated in thin, injection-moulded, flat discs and plates, varying polymer type, fibre type, and fill percentage. To a certain degree, the fibres could be used to balance out shrinkage from polymer alignment. For example, in glass-filled acetal parts, the flow shrinkage from aligned acetal molecules was approximately equal to the transverse shrinkage developed from aligned glass fibres when at a fibre content of 8% by weight. With this relatively even shrinkage, the part was found to have the lowest recorded warpage at this level of fibre filling [59]. Additionally, the use of glass beads in place of glass fibres in nylon 6/6 parts did not affect the transverse shrinkage developed from fibre alignment [59]. Overall, the author found that warpage was easiest to control when making thin, uniform parts using beads as filler in an amorphous matrix. Unfortunately, this combination also produced the weakest parts [59].

For more complex shapes – shapes that merit the use of the injection-moulding process – fibre alignment and distribution become more complex. Filling has been studied at length, with focusses on predicting the advancement of the flow front as well as on predicting pressure and temperature distributions [60]. Efforts focussing on modelling the resulting shrinkage and warpage within the parts were rare prior to Zheng et al's numerical model, which incorporated thermal history and stress relaxation into the simulation of the filling, packing and cooling of injection moulded parts [60]. In recent years, authors such as Taghizadeh et al [61] and Guo et al [62] have performed comprehensive studies on process conditions for injection moulding pure thermoplastic parts and their impact on warpage. The studies by these authors, and similar studies on plastic injection moulded parts are made possible by the commercial software – Moldex3D and Autodesk's Moldflow – which simulates the melting, injection, dwell, and cooling of an injection moulded part. Moldflow can calculate part shrinkage and resulting warpage, accounting for thermal gradients and material properties. However, most work focusses on neat thermoplastics. Most recently, Jiang et al developed a numerical model for determining warpage in a glass-filled injection moulded part, accounting for filling, pressurization, and cooling in air. This model gave results between those generated in Moldflow and the true experimental values [58], showing that modelling of fibre-filled thermoplastic composites is progressing.

1.3.5 **Summary**

To best understand the residual stress development in thermoset composites, the cure kinetics of the resin must be accounted for as a function of processing conditions throughout cure. Global residual stresses in turn affect the cure progression within the part, with thermal gradients affecting the degree of cure in each ply. Convergent's COMPRO® software makes this possible.

A similar approach must be taken for understanding residual stress development in thermoplastic composites – regardless of fibre length. The existing limitation is full thermal and visco-elastic characterization of thermoplastic matrices. As well, for short-fibre composites, the flow of the short fibres, their resulting alignment, and their final distribution must be considered. Commercial software helps to make this possible. However, as found in a review of the literature, there is a deeper understanding of continuous-fibre thermoset-matrix composites than there is of thermoplastic composites. Table 1 summarizes some findings from the literature, highlighting that while many of the factors creating warpage within composite parts are known, there are still many existing unknowns for the overall impact of each factor, particularly in thermoplastic-matrix composites.

Table 1: Summary of factors contributing warpage in continuous fibre and short-fibre compacts and known levels of impact.

	Parameter	Impact		
		T-800H/3900-2 carbon/epoxy unidirectional prepreg	APC-2 unidirectional carbon/PEEK prepreg	Carbon-filled PEEK short fibre composites
Extrinsic	Tool Material	Medium [47]	? [43]	?
	Tool Surface	High [47]	? [43]	?
	Thermal Gradient	?	?	?
	Pressure During Cure	Medium [39]	Low [43]	High [57]
	Cure Cycle /Cooling Rate	High [47]	High** [56]	?
Intrinsic	Lay-up/fibre dispersion	?	?	High [59]
	Part Thickness	High [47]	?	High [59]
	Part Length	High [47]	?	?
	Part Aspect Ratio	?*	High [56]	?

*The study performed by Albert and Fernlund [47] focussed on spring-in of angled composite brackets. While the part aspect ratio was shown to have low importance for spring-in, no comment was provided on its affect on warpage.

**Per [56], changing cooling rates between 1.5°C/min – 100°C/min does not have significant effect, but warpage decreases significantly for cooling rates on the order of 1000s°C/min

Even less is understood about warpage in thermoplastic-matrix DLF composites and their compounded complex residual stress state. They are different from continuous fibre composites in that each individual strand acts as its own lamina. Each strand will overlap with multiple strands to varying degrees and in varying orientations creating complex macro-mechanical stress interactions. As well, the discontinuities in stress at the edge of each strand and the high fibre volume fraction compared to short-fibre composites will further contribute to warpage. Finally, the strand dispersion is random and will change for every part. So, there is a lot left to explore regarding the dimensional stability of DLF composites.

1.4 Research Objectives

Compression moulding of DLF composites has been shown to create near net-shape replacements for complex aerospace brackets. Parts with sudden thickness changes, ribs, tight radii, moulded-in holes and other complex features have been produced using chopped strands of carbon/PEEK as a bulk moulding compound. As the demand for DLF components grows, it is important to understand the limitations of the material system and its suitability for creating larger parts that could potentially have sizeable, thin sections. While a baseline understanding of the achievable mechanical properties and associated variation in mechanical properties of DLF composites exists, the literature review has shown that there continues to be a gap in understanding the processing implications of this material, particularly when it comes to final part stability. Much is understood in terms of mitigating warpage in thermoset-matrix continuous-fibre composites and there is a growing understanding of warpage within both short-fibre and continuous-fibre thermoplastic-matrix composites. However, little is known about warpage in DLF composites. In light of this gap, the primary objective of this thesis is to advance the knowledge of warpage in DLF composites such that critical part size and thickness can easily be determined in the design stages for DLF parts with large, thin sections and tight dimensional stability requirements. In addressing this knowledge gap, this thesis will serve to explore the following:

1. Characterize dimensional stability in thin gauge DLF parts – In Chapter 2, a processing investigation of thin-gauge flat plates is conducted to find trends between part thickness, strand size, and resulting warpage. As well, preliminary efforts into simulating warpage within these flat plates will be presented.
2. Investigate methods of mitigating warpage – In Chapter 3, periodic stiffening features are introduced to determine their effects on warpage. A study of rib size and its presumed effect on part mass and stiffness is addressed, followed by a fill-assessment on ribbed parts, updated processing conditions to achieve good quality parts, and finally a comparison of ribbed parts to flat parts in terms of warpage.

Chapter 4 will summarize the conclusions from this research and present potential future work.

2. Processing Investigation – Flat Plates

While the modelling of thermoplastic composites is progressing, challenges in modelling even the more traditional continuous-fibre thermoplastic-matrix composites persist. With the added material complexity of DLF strands, the first step to understanding residual stress and warpage development in DLF composites is to approach them experimentally. In this chapter, flat plates are moulded with two different strand sizes and at incrementally increasing thicknesses to look for trends in how they warp.

Processing conditions for 101.6 mm x 101.6 mm and 304.8 mm x 355.6 mm flat plates have been established by Landry in [63]. So, 101.6 mm x 101.6 mm plates were first moulded using these known processing conditions. After assessing the warpage in these small plates and looking for trends between warpage, thickness, and strand size in Section 2.1, 304.8 mm x 355.6 mm plates of fixed thickness and strand size were made. These large plates were compared to the smaller plates to assess any possible trends between plate warpage and plate size in Section 2.2.

Finally, a preliminary simulation of the moulded 101.6 mm x 101.6 mm plates was developed and compared to the moulded plates in Section 2.3.

2.1 Small DLF Composite Panels

DLF flat plates measuring 101.6 mm x 101.6 mm were moulded at consistent processing conditions, varying thickness and strand size to determine the impact of these variables on part warpage. All plates were thin, with the thickest plates measuring 3.8 mm thick.

2.1.1 **Experimental Setup**

2.1.1.1 Material and Test Matrix

Chopped strands of pre-impregnated, unidirectional AS4 carbon fibre/PEEK tape were used. Two different sizes of strands were assessed – 6.35 mm x 3.18 mm strands of TenCate Cetex® MC1200 bulk moulding compound and 12.70 mm x 12.70 mm strands of TenCate APC-2/AS4 tape. For the remainder of this document, the 6.35 mm x 3.18 mm strands will be referred to as "short strands" and the 12.70 mm x 12.70 mm strands will be referred to as "square strands." Both strand sizes have a fibre volume fraction of approximately 59%, a consolidated ply thickness of 0.132 mm, a melting point of 343°C, and a glass transition temperature of 143°C. Panels were moulded following the test matrix presented in Table 2. Target panel thickness was achieved by weighing material prior to placement – using the density of the material and the intended volume of the part cavity to determine the required weight.

Table 2: Small flat panel test matrix.

Strand Size	Quantity Moulded at Plate Thickness					
	1.0 mm	1.5 mm	2.0 mm	2.3 mm	3.0 mm	3.8mm
6.35 mm x 3.18 mm	2	2	2	-	2	2
12.70 mm x 12.70 mm	2	2	2	3	2	-

2.1.1.2 Test Setup

The panels were manufactured in a 250 kN MTS load frame, retrofitted with a small instrumented hot press as pictured in Figure 13. The press was heated using four 500 W FIREROD® heating cartridges by Watlow in each the top and bottom platen. The heating was controlled using an SD Series proportional-integrative-derivative (PID) controller from Watlow. The top platen’s and bottom platen’s heating cartridges were controlled separately. Platen surfaces had a high-quality surface finish as they were ground when initially manufactured. A picture frame mould was fitted around the bottom platen, creating a 101.6 mm x 101.6 mm mould. Cooling was implemented through forced air. A compressed air hose was fitted to both top and bottom platens during cooling to force air through three cooling channels in each platen. The rate of cooling was controlled by setting a fixed cooling rate on the PID control for the heating cartridges.

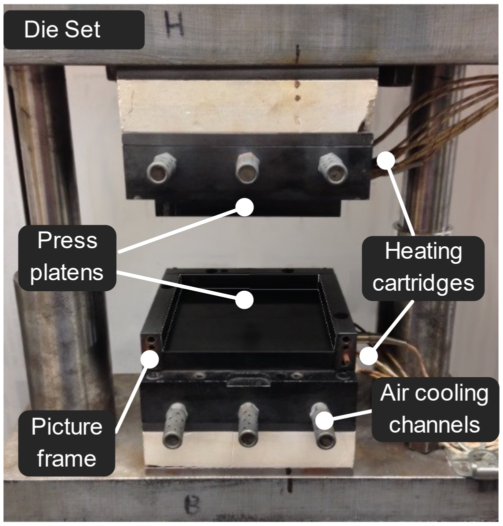

Figure 13: Instrumented hot press used to mould 101.6 mm x 101.6 mm DLF panels [63].

Strands were manually distributed in the mould cavity that had been coated with Frekote® NC-700 release agent. Strands were added in small batches, shuffling between batches to allow for an even, random distribution and minimize out-of-plane strand orientation. The cavity was filled evenly, as pictured in Figure 14, to minimize flow during moulding, and create the most mechanically consistent panels possible while using a manual, bulk moulding technique. Leaving gaps would promote excessive flow, which has been shown to increase fibre alignment near the edges of the mould cavity [63] and create further unpredictability in final part properties. To consistently compare physical characteristics between panels, a coordinate system was established, with *x* in the direction of the heating cartridges, *y* following the path of the cooling channels from outlet to inlet, and *z* pointing upwards, as pictured in Figure 14.

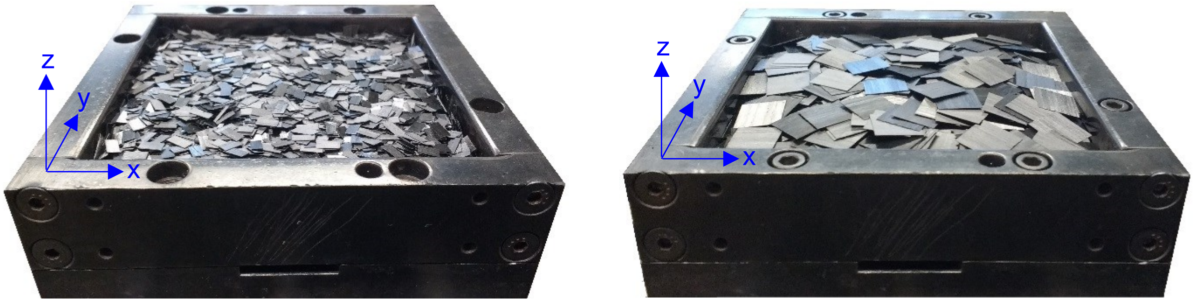

(a) (b)

Figure 14: DLF material distribution of (a) short strands and (b) square strands in mould cavity.

2.1.1.3 *Procedure and Process Cycle*

After material is appropriately distributed in the mould cavity, the moulding cycle can be initiated. All panels were moulded using consistent processing conditions, as shown in Figure 15 and determined to make "defect-free" panels by Landry and Hubert in [17]. An initial pressure of 10 bar is applied to pack the strands together, as the mould heats up to a target temperature of 380°C – almost 40° above the melting point of the PEEK matrix (343°C). With the controller at this temperature, pressure is increased to 70 bar and the part is left to dwell at 380°C for 15 minutes. This hold time is implemented to lessen thermal gradients within the mould and ensure that the full material charge is heated above 360°C – the temperature at which all nuclei for crystallites will be eliminated [45]. Following dwell, 70 bar of consolidation pressure is maintained during cooling. This high processing pressure is necessary because, as explained in [17], the part cools as it shrinks – both from the effects of thermal expansion and crystallization in the PEEK matrix. Due to temperature gradients within the mould, parts shrink unevenly – shrinking where the mould cools first. In [17], Landry determined that, for the thermal gradient in this instrumented hot press, 70 bar of pressure was sufficient to maintain contact between the part and mould platens until the full part had cooled below crystallization temperature, preventing surface defects in the final part. So, 70 bar of pressure was maintained during part cooling.

Cooling was performed at approximately 10°C/min, using the heating cartridges and controller to meter the cooling rate. For semi-crystalline thermoplastics, like PEEK, it is known that cooling rate affects the degree of crystallinity and the crystallization temperature. For fast cooling rates – on the order of 5000°C/min and above, the matrix does not have time to crystallize and stays purely amorphous [41, 56]. At low cooling rates, the thermoplastic can reach its maximum level of crystallinity, achieving crystalline fractions near 40% when cooled at less than 1°C/min [41, 56]. According to Wang et al [64], the ideal degree of crystallinity for PEEK is around 30% for the best balance of stiffness, toughness, and solvent resistance. Tests on pure PEEK have shown that its crystalline fraction is relatively easy to control [19] and only shows significant changes when cooled at rates above 600°C/min [64] – a rate that is often impractical [43]. For the cooling rates possible in the instrumented hot press used – between approximately 1°C/min and 20°C/min – the degree of crystallization of PEEK remains relatively constant. For cooling rates between 5°C/min and 20°C/min, the degree of crystallization is approximately 33% [63]. For 1°C/min cooling rates, the degree of crystallinity was found to be approximately 27% [63], contrary to the trend of increasing crystallinity for slower cooling implied by Unger [41, 56]. The range of crystallization temperature, however, changes with cooling rate. It lowers with increasing cooling rate, changing from a range of 297°C-326°C for a cooling rate of 1°C/min to a range of 250°C-307°C when cooled at 20°C/min [63]. Changes between cooling rates in the range possible for the instrumented hot press are not expected to create significant changes in part warpage, and cooling rates were maintained at 10°C/min for the panels moulded. At this cooling rate, crystallization was found to occur between approximately 280°C-320°C by Landry in [63]. For Chapman in [65], crystallization was found to initiate at approximately 307°C in carbon/PEEK laminates cooled at 10°C/min.

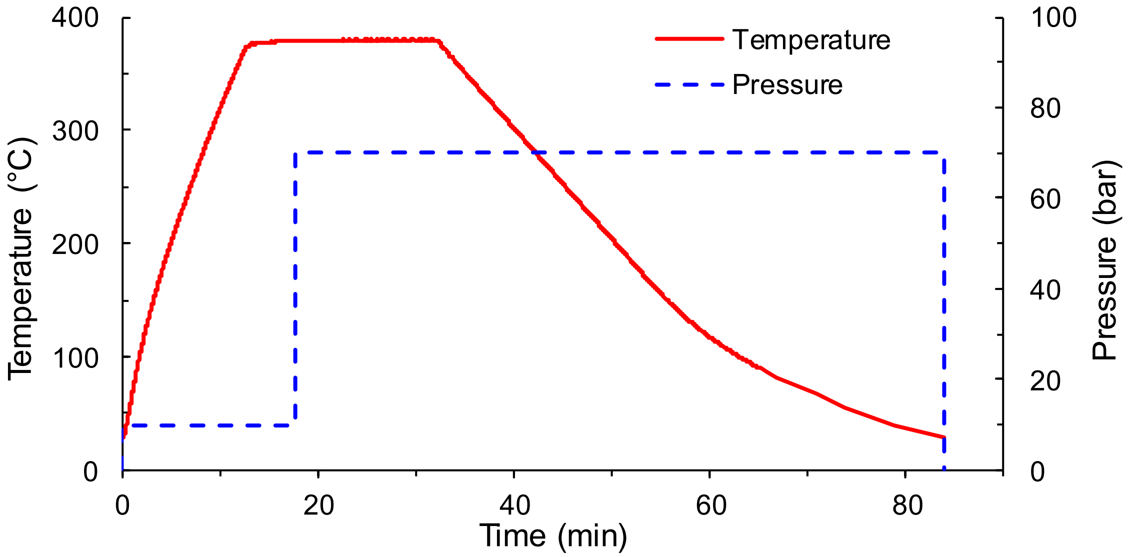

Figure 15: Processing cycle used to mould 101.6 mm x 101.6 mm DLF panels.

2.1.2 **Results and Analysis**

2.1.2.1 Warpage Magnitude

Similar to what was described by Selezneva and Lessard in [14], the panels were initially compared based on an overall warpage value determined by the distance between the lowest and highest point on the part, as pictured in Figure 16. However, since the parts made were thin and flexible, they could not be measured using a physical probe. The force from a standard dial gauge or CMM probe would deflect the 2.0 mm and thinner panels. So, to find this warpage measurement, the panels were scanned using a FARO® ScanArm, generating a unique point cloud for each part in Geomagic Studio. The point cloud was then converted to a 3D model and exported as an STL file. Using InnovMetric's PolyWorks® IMInspect software, these unique part models were aligned with 3D models of perfectly flat panels using a best-fit approximation and electronically probed to determine their deviation from a flat surface, effectively providing a flatness measurement.

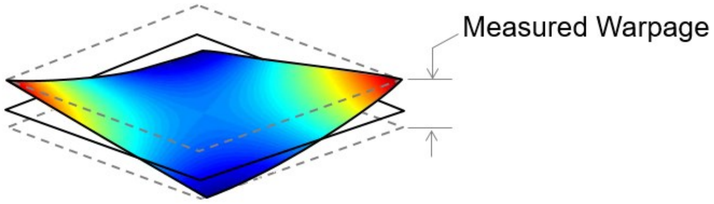

Figure 16: Depiction of warpage measurement for DLF panels.

The results of the warpage measurements are compiled in Figure 17.

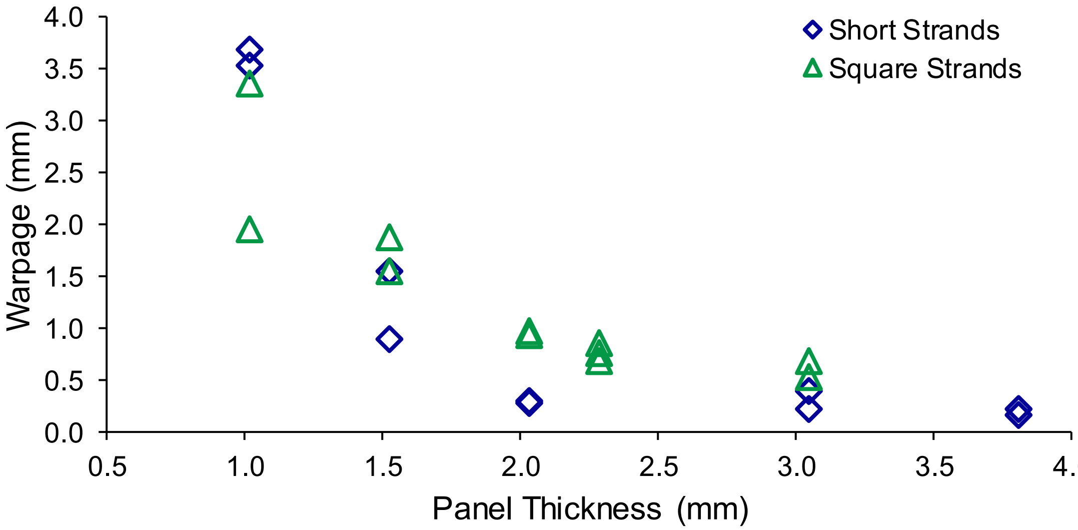

Figure 17: Measured panel warpage as a function of panel thickness for short and square strands.

From these results, a few trends are immediately clear. First, there is significant scatter in warpage values for the 1.0 mm and 1.5 mm thick plates. Additionally, the warpage values for these plates are greater than the plate thickness – ranging from 2.0 – 3.7 mm of warpage in the 1.0 mm panels and from 0.9 – 2.9 mm warpage in the 1.5 mm thick panels. So, it is clear that warpage in parts made thinner than 2.0 mm, with short or square strands, is hard to predict.

Second, warpage appears to decrease with increasing panel thickness. Past 2.0 mm of thickness, the warpage in panels made with the short strands is relatively stable with an average of 0.26 mm warpage. The panels made with the square strands decrease from 0.94 mm and 0.96 mm of warpage in 2.0 mm thick panels to 0.69 mm and 0.53 mm of warpage in the 3.0 mm thick panels. This trend of decreasing warpage for increasing thickness is intuitive, particularly for thin plates where the temperature gradient through the thickness of the plate is not believed to be significant. As warpage is created by residual stresses internal to the plate, stiffer plates should better resist warpage. The stiffness of the plate is closely tied to its thickness, with its moment of inertia increasing as a cubic function of thickness.

Finally, it is apparent that, with the exception of the 1.0 mm thick plates, the plates made with the larger, square strands, sustained greater warpage than those made with the short strands. For example, the 2.0 mm thick plates had approximately 0.28 mm – 0.29 mm of warpage when made with short strands but approximately 0.94 mm – 0.96 mm of warpage when made with square strands, showing more than a three-fold increase in warpage. This trend is less intuitive, but consistent with what was seen by Selezneva and Lessard in [14]. Increasing the strand size significantly reduces the number of strands that are randomly distributed within the plate and thus reduce the likelihood of a relatively homogeneous distribution. The square strands are eight times larger than the short strands, so there are roughly one eighth of the number of strands in the same panel thickness making these panels much more heterogeneous. It is believed that this increased heterogeneity contributes to the increase in part warpage.

Since each panel warped differently (as further discussed in Section 2.1.2.2), a second method of gauging warpage was utilized. To avoid any extreme local deflections from dominating the warpage value, a weighted average of the panel's deviation was taken over its area. The volume between each warped panel and its best-fit plane was determined using MATLAB and normalized against the area of the panel. First, the surface represented by the data points collected for each panel was fit with a surface using the `scatteredInterpolant` function in MATLAB. Then, the volume between the surface and the best-fit plane was calculated using the `quad2d` function. This was done separately for the portions of the panel surface above (V_{dev+}) and below (V_{dev-}) the best-fit plane. These volumes were then summed and divided by the projected plate area that they span – the panel's total area. A visual depiction of the volume between the surface and the best-fit plane is presented in Figure 18. The results are shown in Figure 19.

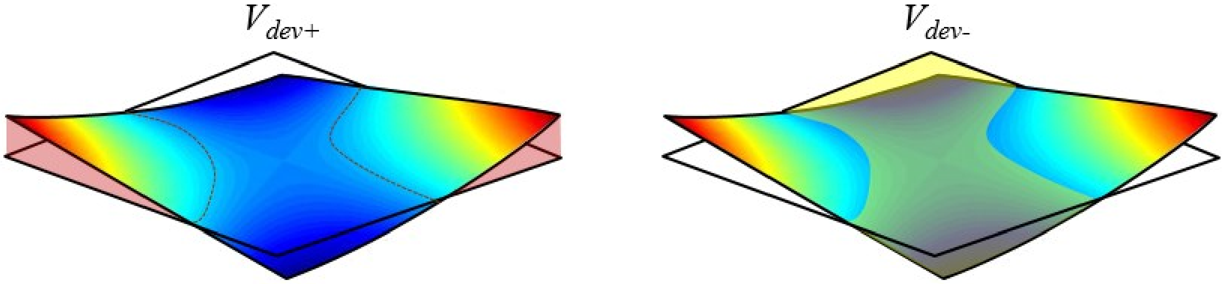

Figure 18: Volume between the surface above (shaded in red) and below (shaded in yellow) the best-fit plane.

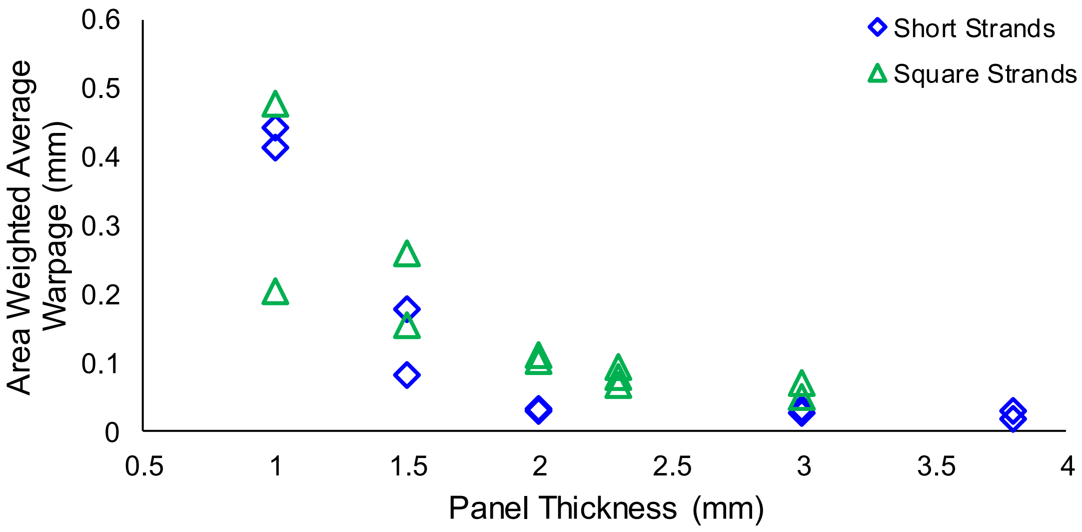

Figure 19: Area weighted average warpage as a function of panel thickness for short and square strands

The captured trend is very similar to the trend captured by the previous warpage magnitude measurements in Figure 17, and further emphasizes the instability of warpage measurements in 1.0 mm and 1.5 mm thick panels. These panels saw the greatest change between warpage magnitude measurements, as a flatness measurement, and the area weighted average warpage measurement, with variation in the relative difference between short-strand and square-strand panel warpage. Overall, the panels made with square strands sustain more warpage than the panels made with short strands and warpage decreases with increasing panel thickness.

2.1.2.2 Warped Shapes

Beyond knowing the magnitude of warpage, it is important to know how the parts will warp. Unfortunately, the warped shape of each part was different, without a clear trend. For all parts made, the highest and lowest points on the plate were found along the free edge of the plate. However, the locations and number of maxima and minima are not consistent. Of the twenty-one parts made, thirteen have relatively saddle-shaped warpage patterns, such as that seen in Figure 20, with saddle points – where orthogonal curves meet at a maximum for one and a minimum for the other – near the centre of the plate. However, the locations of the part’s maximum and minimum points are in different corners or points along the free edges for each part – regardless of thickness or strand size. As seen in Figure 21, the saddle shape may have its extrema at all four corners, along each edge, or in some combination of both. All warped shapes are shown in Appendix A, where it is apparent that the orientation of each saddle can be dramatically different between parts. The parts that were found to be relatively saddle-shaped are indicated in Table 3, with the quantity of saddle-shaped parts at each strand size and thickness indicated.

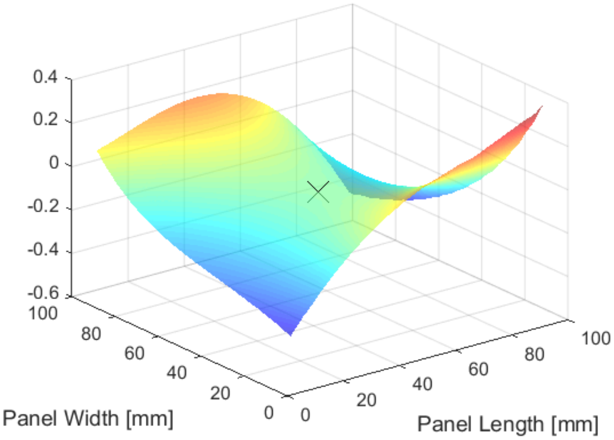

Figure 20: Warped shape of 2.0 mm thick panel made with square strands, showing saddle-point marked with an “X”.

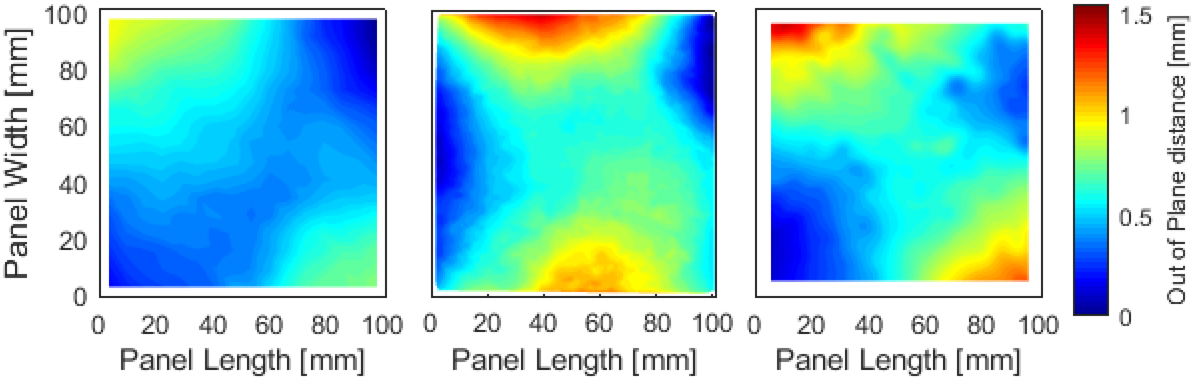

(a) (b) (c)

Figure 21: Warped shape of (a) 2.0 mm thick part made with square strands, showing maxima and minima at corners; (b) 1.5 mm thick part made with short strands, showing maxima and minima at free edges; and (c) 2.3 mm thick part made with square strands, showing mixture of maxima and minima at corners and edges.

Table 3: Distribution of saddle-shaped parts.

Strand Size	Quantity of Saddle-Shaped Parts at Each Plate Thickness					
	1.0 mm	1.5 mm	2.0 mm	2.3 mm	3.0 mm	3.8mm
6.35 mm x 3.18 mm	2	2	0	■	0	2
12.70 mm x 12.70 mm	1	2	2	1	1	■

Eleven of the saddle-shaped parts were successfully fit with polynomial surfaces of the fourth order in both x and y, with r-squared values ranging from 0.924 – 0.997. (The 3.8 mm thick panels did not achieve a good surface fit.) From these best-fit surfaces, the locations of each panel's saddle point, maxima, and minima were calculated. The saddle points were clustered near the centre of the plates, as plotted in Figure 22. There was no apparent trend in the out-of-plane location of the saddle points.

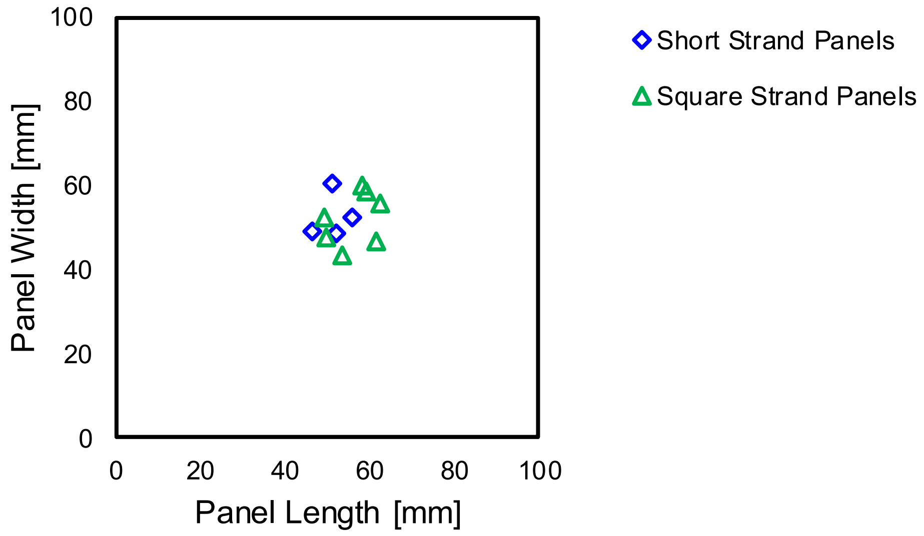

Figure 22: Locations of saddle points on saddle-shaped panels made with short strands at 1.0 mm and 1.5 mm thicknesses as well as with square strands at all thicknesses.

Four of the plates showed uneven warped shapes with three local maxima and three local minima. The saddle points in these parts were typically skewed to one side, as displayed in Figure 23. The parts exhibiting these shapes were all made with square strands, as seen in Table 4. Of these plates, only two were fit to fourth-order polynomial surfaces in x and y with some success – the 1.0 mm thick plate and one of the 2.3 mm thick plates. Surface fits were not successfully found for the other two panels.

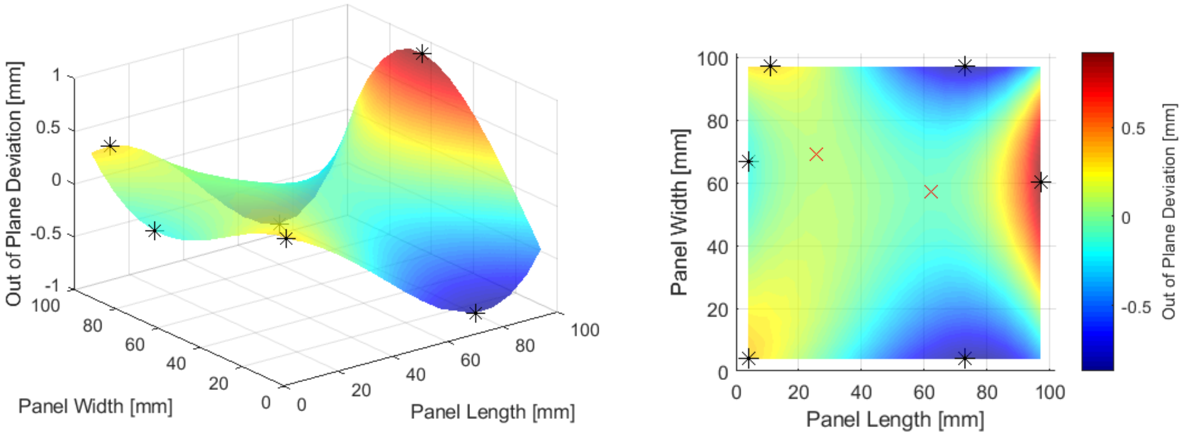

(a) (b)

Figure 23: Warped shape of 1.0 mm thick part made with square strands, showing (a) in 3D with maxima and minima marked with black stars and (b) as a contour plot, showing maxima and minima marked with black stars and saddle-points marked with red Xs.

Table 4: Distribution of parts with three local maxima and minima.

Strand Size	Quantity of Saddle-Shaped Parts at Each Plate Thickness					
	1.0 mm	1.5 mm	2.0 mm	2.3 mm	3.0 mm	3.8mm
6.35 mm x 3.18 mm	0	0	0	■	0	0
12.70 mm x 12.70 mm	1	0	0	2	1	■

The remaining four plates did not have clear trends to their shape, with the lowest or highest regions of the plate extending towards the part's centre. These four plates with less distinguishing features were all among the group with the lowest warpage – parts made with the short strands at thicknesses of 2.0 mm and 3.0 mm. As an example, the 2.0 mm thick panels are pictured in Figure 24.

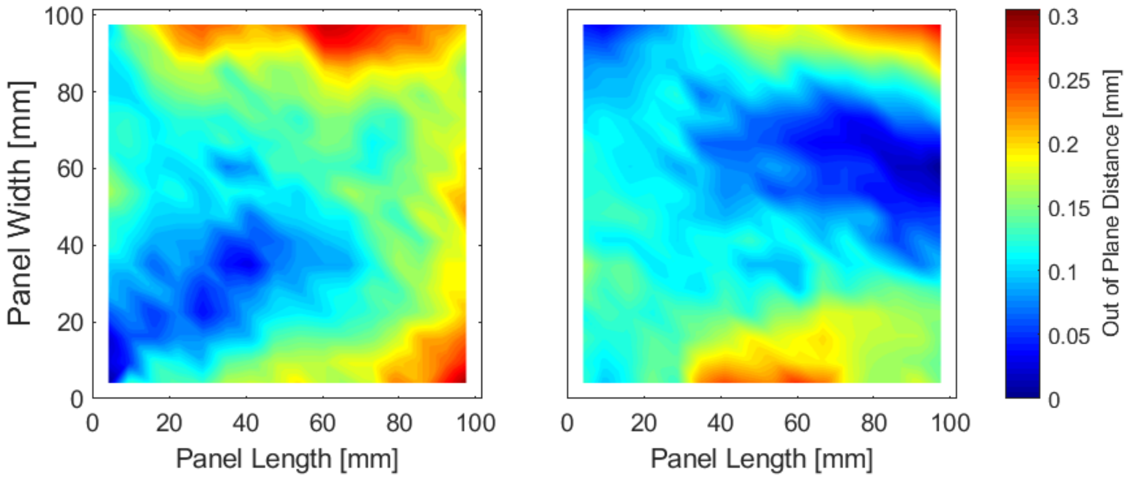

Figure 24: Warped shape of 2.0 mm thick part made with short strands.

2.1.2.3 Non-Dimensionalization of Warpage for Comparison between Panel Sizes

Due to the inconsistencies between warped shapes of the panels and lack of surface fit in many panels, there is not a clear-cut way to non-dimensionalize the data. For the saddle-shaped panels fit with fourth-order polynomial surfaces, the out-of-plane deviation at the locations of all local maxima and minima on the saddle-shaped panels were found. The out-of-plane deviations between the local peaks and the saddle-point were then normalized against their distance to the saddle point. The results are shown in Figure 25 and Figure 26, where Figure 25 shows the out-of-plane deviation of the local minima normalized against the distance between the saddle point and the minimum and Figure 26 shows the out-of-plane deviation of the local maxima normalized against the distance between the saddle point and the maximum. While trends remain consistent with the trends found for overall warpage magnitude, the data is quite scattered. On approximately half of the panels, the normalized warpage values found were significantly different for the maxima than they were for the minima.

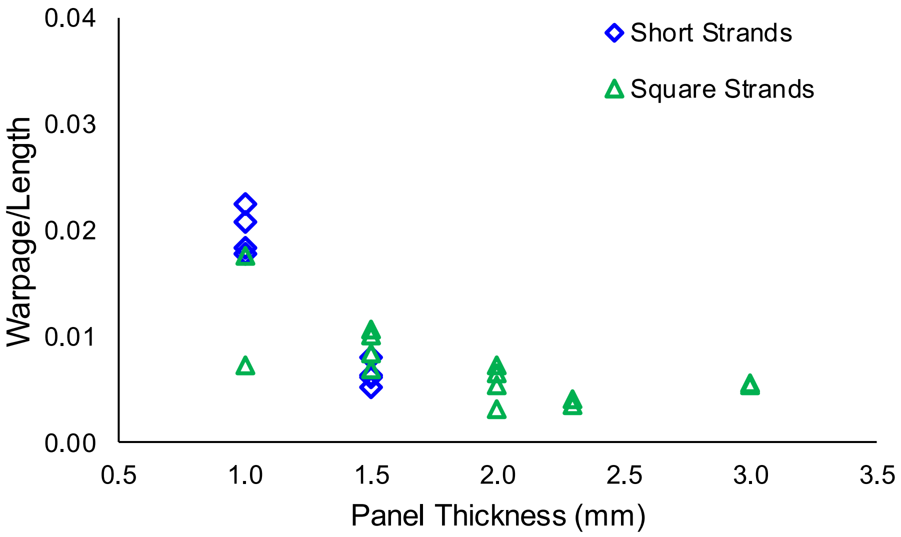

Figure 25: Out-of-plane deviation between local minima and saddle-point, normalized against distance between saddle-point and minimum for saddle-shaped panels.

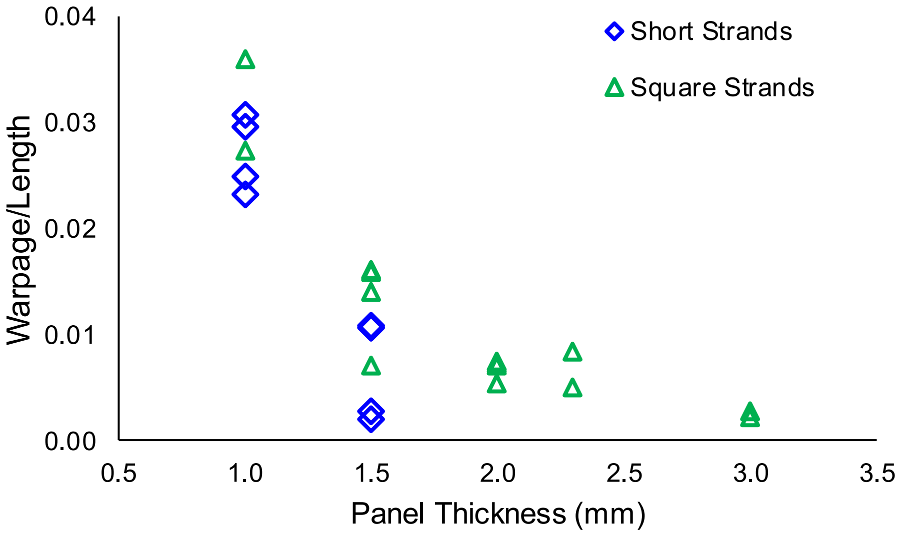

Figure 26: Out-of-plane deviation between local maxima and saddle-point, normalized against distance between saddle-point and maximum for saddle-shaped panels.

This method of non-dimensionalization only works for saddle-shaped parts that were successfully fit with polynomial surfaces. So, it is difficult to directly compare between panels of different sizes. As another way of comparing plates between sizes, the deviation between the absolute maximum and minimum on each plate was found and normalized against the distance between these points. These non-dimensional measurements are presented in Figure 27. This measurement can be used to compare between panels of different sizes, but does not capture data of any intermediate maxima or minima, or the trajectory of the warpage.

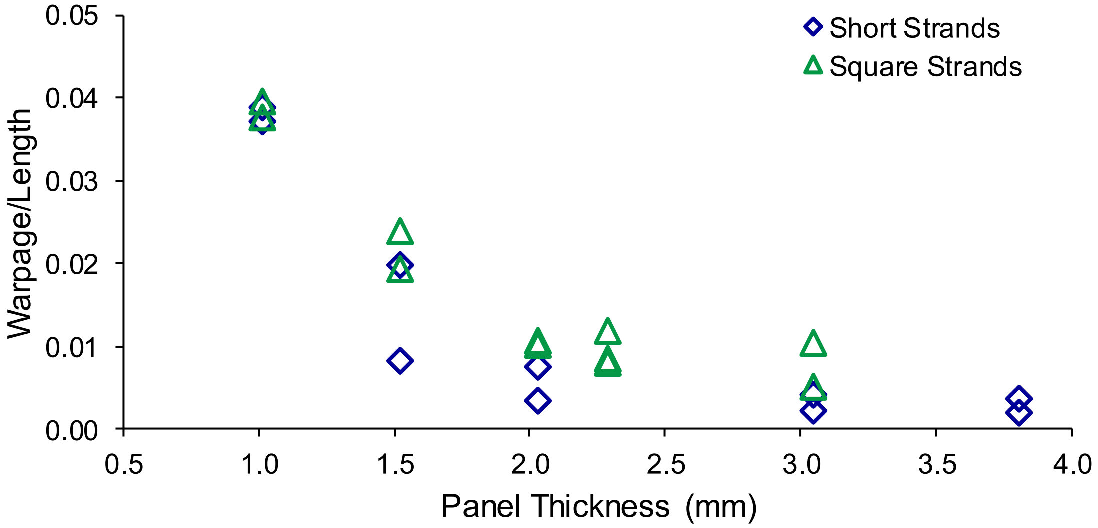

Figure 27: Warpage per unit length, taken as the difference in maximum and minimum out-of-plane deviation normalized against the distance between absolute maxima and minima for 101.6 mm x 101.6 mm plates.

Similar trends were seen when plotting warpage per unit length as were seen when plotting warpage magnitude – warpage decreased with increasing thickness and warpage was more significant in plates made with square strands than it was for the short-strand plates. Interestingly, the scatter seen in the 1.0 mm thick plates was reduced.

2.1.2.4 Thickness

All parts were also assessed for thickness, to determine if there was a link between thickness deviations and warpage. First, virtual caliper measurements were taken across the panel in PolyWorks® IMInspect software, using the STL file created from the 3D scanned data discussed in Section 2.1.2.1. As well, measurements were taken at 12.7 mm increments, using an external micrometer from Mitutoyo. (Part Number 118-107 with a 0-1" span). Each part was measured three times with the micrometer and the average measurement at each location was then compared to the data collected in PolyWorks®.

Each panel had a slightly different thickness distribution, indicating that the random strand geometry contributed to variations in thickness. The general trend of observed thickness distributions were consistent between virtual caliper and physical micrometer measurements.

However, the values obtained using the virtual calipers had larger deviations and were larger than those measured with the micrometer in general. When measured with a micrometer, all panels were found to be within 0.26 mm of the target thickness at all measured locations, with the exception of one of the short-strand 3.8 mm thick panels, which lost material during moulding and ended up being as much as 0.43 mm below its target thickness in places. Many of the panels were within as little as 0.11 mm from the target thickness at all locations.

These thickness distributions were compared with the curvature within the panels, and with the panels' ability to fit polynomial surfaces. However, no clear relation was found between the thickness distribution and warpage. The range of thickness measurements for each panel is captured in Appendix A, showing contour plots of the results from the external micrometer measurements.

2.2 Large Flat Plates

Large DLF flat plates measuring 304.8 mm x 355.6 mm were moulded for comparison with the 101.6 mm x 101.6 mm panels. Panels were moulded using the processing conditions established in [63] and [66] to make defect free panels. The pressure and cooling rates used differ from those used to make the 101.6 mm x 101.6 mm panels, but are expected to create parts with good quality surface finishes and near negligible void content.

2.2.1 **Experimental Setup**

2.2.1.1 Material and Test Matrix

The same unidirectional AS4 carbon fibre/PEEK tape material, described in Section 2.1.1.1, was used for moulding the large DLF plates. However, only 12.70 mm x 12.70 mm strands were used. The target panel thickness for all panels was 2.3 mm.

2.2.1.2 Test Setup

Manufacturing took place in a 150 ton Wabash hydraulic press (Wabash MPE V150-36-CX), as detailed in [63] and [66]. The press was retro-fitted with additional steel plates to reduce the thermal gradient induced during cooling. These plates were designed by S. Roy of the Aerospace Manufacturing Technology Centre of the National Research Council, as described in [66].

A polished flat plate, measuring 304.8 mm x 355.6 mm and coated with Frekote® 700-NC release agent was placed in the centre of the bottom press platen. The plate had three small notches to provide room for thermocouple measurement. For every plate manufactured, the notches were configured as shown in Figure 28. One thermocouple was fixed in place in each notch, and a picture frame mould was fitted around them. The maximum temperature difference between thermocouples at any point during cooling was approximately 20°C at the most. In a standard Wabash press, without the additional plates designed by S. Roy, thermal gradients can be as large as 120°C for a mould this size, as seen in [63].

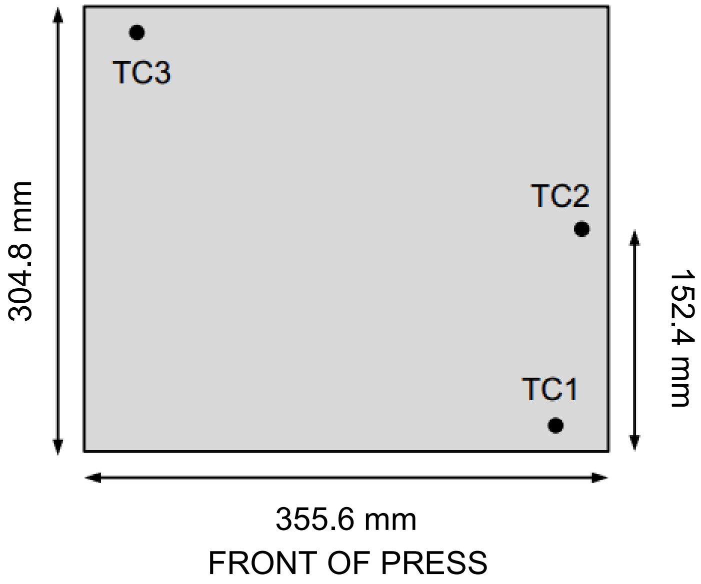

Figure 28: Thermocouple configuration on bottom mould surface for 304.8 mm x 355.6 mm, oriented within a Wabash press (adapted from [63]).

Material was evenly distributed onto the polished flat plate in five batches. After the first 20% of the material was added, the thermocouples were repositioned such that they would be measuring temperature on top of a few layers of material. At each 20% increment, material was manually shuffled until it was visibly level. After all material was placed, the mould appeared as it does in Figure 29. Then, a flat plate was placed gently on top of the material, taking care to keep all material within the mould cavity, and the press was closed. All mould surfaces were coated with Frekote® 700-NC release agent prior to material distribution.

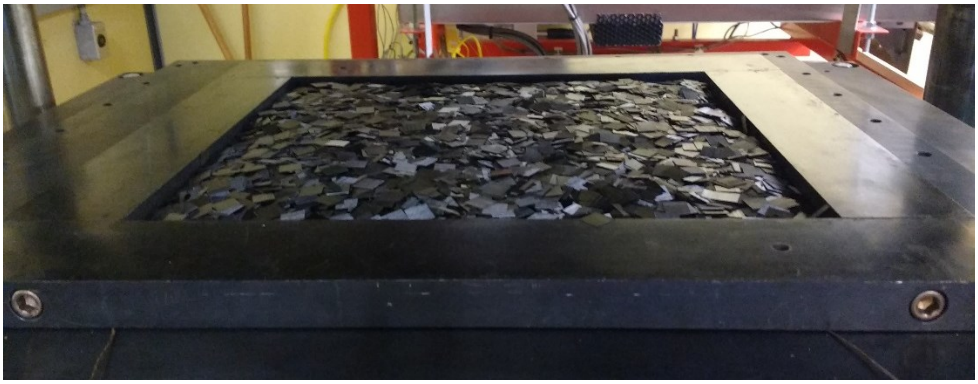

Figure 29: Wabash hydraulic press with DLF material distributed in 304.8 mm x 355.6 mm picture-frame mould.

2.2.1.3 *Procedure and Process Cycle*

The moulding cycle was initiated once the press was closed. The material was compressed under approximately 9.6 bar of pressure – corresponding with the minimum clamping force in the press – while the material was heated to 380°C. To achieve this temperature within the material, the press was set at 400°C until the thermocouples embedded in the plate read 380°C. Then, the controller was reduced to 380°C and pressure was manually increased to 34.6 bar – the pressure determined to create defect-free parts in [63]. The parts were held at approximately 380°C and 34.6 bar pressure for 15 minutes, but due to a lag between the temperature controller and the material temperature, the effective dwell time in the material ranged from 18-31 minutes.

Under 34.6 bar of pressure, a cooling cycle, programmed into the Wabash press, was initiated. The parts were slow-cooled using only forced air until the platen temperature dropped below 343°C. This corresponds to a cooling rate between 1.5°C/min – 2.0°C/min at the platen, and a similar cooling rate in the part. The cooling rates were slightly different at each thermocouple, but ranged from 1.0°C/min – 1.9°C/min while air cooling was employed. When the platen temperature reached 343°C, the part material was typically between 363°C and 369°C – still above the melting point of the material. At this point, a mixture of air and water cooling was employed, causing the platen temperature to decrease at a rate between 12°C/min and 14°C/min. Due to the added fixturing in the press, the material typically took four or five minutes from when the new cooling rate initiated at the platens to when the material saw a change in cooling rate. The material continued to cool at the air-cooled rate until it was approximately between 340°C and 360°C at the thermocouples. So, when the cooling rate in the part was increased from the addition of water cooling, the bulk of the material was likely still molten. The addition of water increased the cooling rate to between 5.5°C/min and 7.5°C/min in the material. In each cycle, the cooling rate measured between thermocouples could vary by up to 1°C/min over this period. After the platen temperature reached 177°C, pure water cooling was initiated. This did not have a significant impact on cooling rate.

An example of the intended processing cycle is captured in Figure 30.

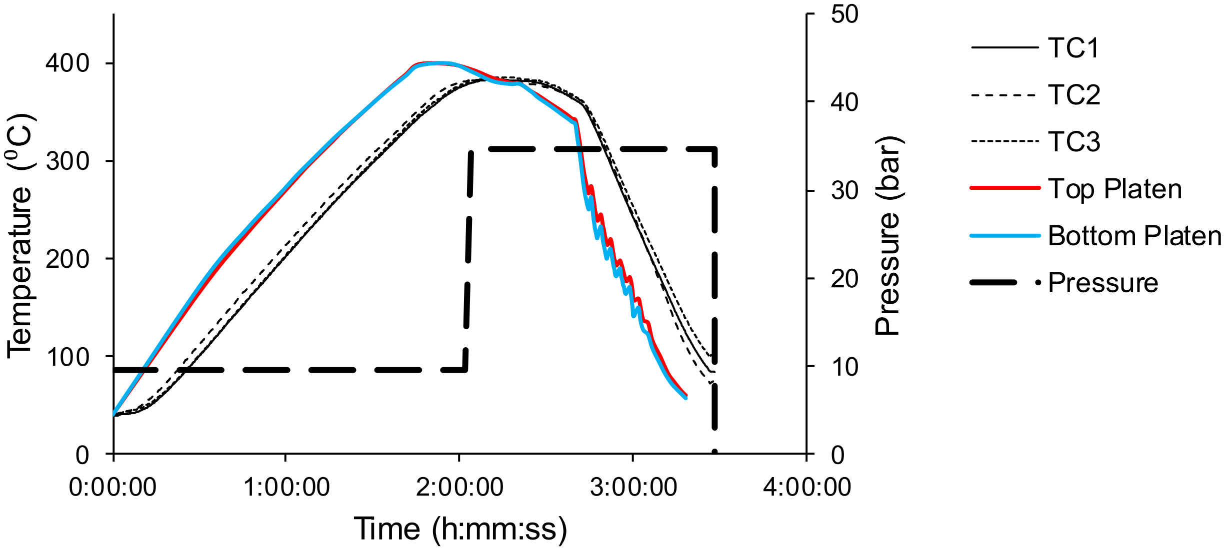

Figure 30: Process cycle used to make 304.8 mm x 355.6 mm parts in 150 ton Wabash press.

2.2.2 **Results and Analysis**

2.2.2.1 Thickness Assessment

Due to the age of the mould, material escaped through the shear gap between the picture frame mould and the polished tool plates during processing of several panels, as pictured in Figure 31. Throughout the subsequent sections of this chapter, the escaped material will be referred to as "flashing." The degree of material loss to flashing affected the final thickness in the moulded panels.

Figure 31: Moulded 304.8 mm x 355.6 mm panel, made with square strands, showing excessive material leakage (flashing) along 304.8 mm sides of the panel.

The first three Panels to be discussed – Panels A, B, and C – were moulded under consistent processing conditions and experienced similar levels of flashing. Using an external micrometer from Mitutoyo, the thickness of these panels was assessed in 25.4 mm increments. Each measurement was taken three times with the same measuring device. The average of these measurements was used to create contour maps of the thickness distributions within panels, which were then validated against thickness distributions taken from 3D-scanned models of the same panels. Plates A and B were 2.23 mm thick on average, with similar thickness distributions as seen in Figure 32 and Plate C was 2.26 mm thick on average. Panel C had a different thickness distribution from Plates A and B, with more thinning along the bottom edge and less thinning along the left-hand side of the panel.

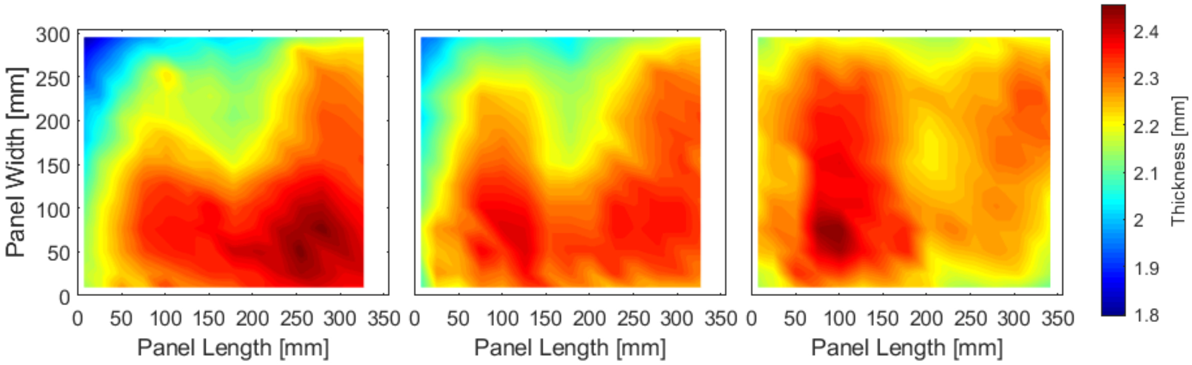

Figure 32: Thickness distributions in Panels A, B, and C which all experienced significant flashing during moulding.

Panels D and E experienced negligible flashing, leading them to both have average thicknesses of 2.36 mm. There were some similarities in their thickness distributions, as shown in Figure 33, but Panel D's thickness distribution was closer to that seen in Panel C.

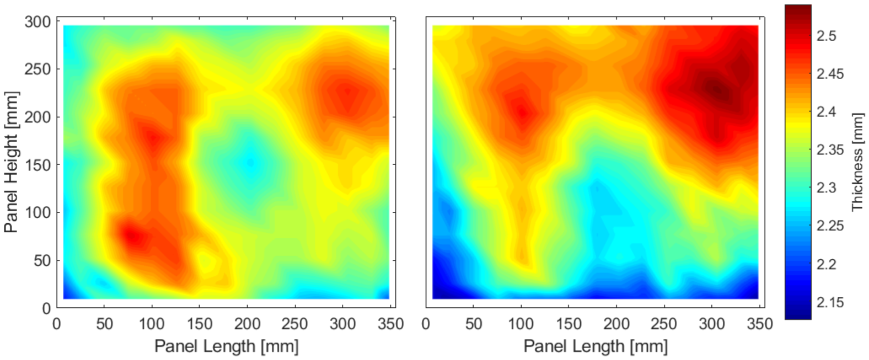

Figure 33: Thickness distributions in Panels D and E which experienced negligible flashing during moulding.

2.2.2.2 Warpage Magnitude Assessment

As discussed in Section 2.1.2.1, the panels were scanned using a FARO® ScanArm and assessed in InnovMetric's PolyWorks®, to find warpage. Despite all panels having the same target thickness, processing conditions, and strand size, the degree of warpage was significantly different between panels. Looking at warpage as an effective flatness measurement, the panels ranged from 1.63 mm – 4.35 mm, as pictured in Figure 34. In this figure, the panels are compared to the small panels made with square strands.

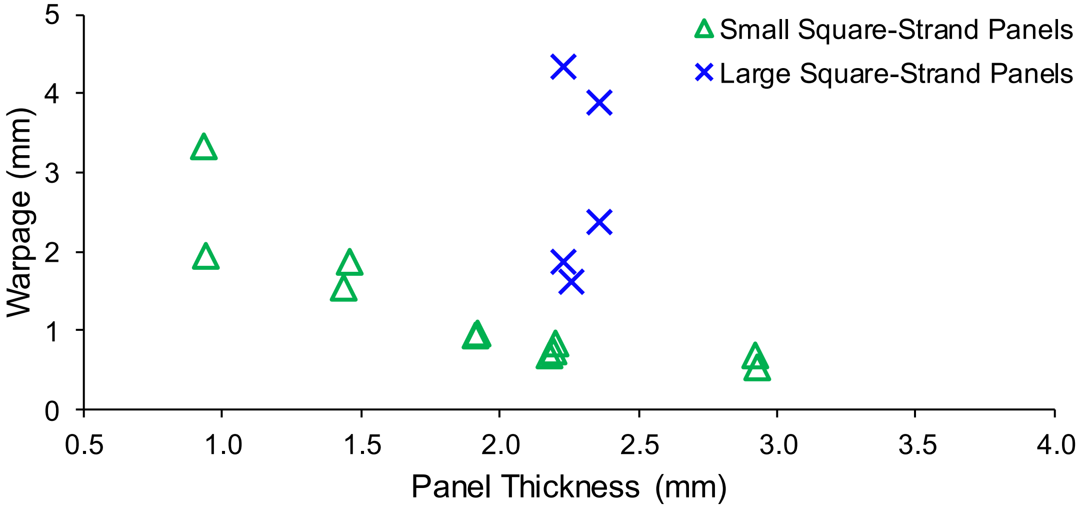

Figure 34: Measured panel warpage as a function of panel thickness for panels made with square strands.

Even though Panels A and B had very similar thickness distributions and average thicknesses, they sustained very different magnitudes of warpage: 4.35 mm and 1.89 mm, respectively. Similarly, Panels D and E sustained very different magnitudes of warpage, with values of 3.90 mm and 2.37 mm, respectively. Panel C had the least warpage, at 1.63 mm. The same degree of variation was seen when panel warpage was measured as an area weighted average, as seen in Figure 35.

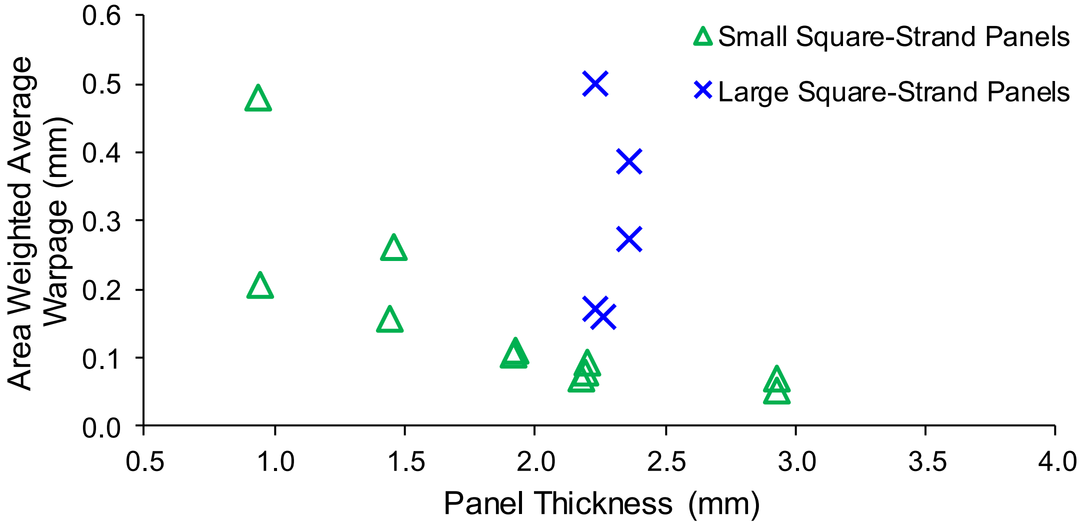

Figure 35: Area weighted average of warpage as a function of panel thickness for panels made with square strands.

There was no apparent trend between panel thickness and warpage, or between material leakage and warpage.

2.2.2.3 *Warped Shape Assessment*

Despite having consistent processing conditions, the shape of each moulded panel was very different. Panel A warped in a dome-like fashion, having only one local maximum at roughly the centre of the panel. The other panels have many maxima and minima distributed throughout, with most located along the free edges. Only Panel C has a distinct local minimum mid-panel. Altogether, the shapes of each panel are very different, regardless of consistency in processing conditions and thickness distributions. Due to the large range in panel magnitude, the contour images for the panels were plotted on two different colour scales, with Panels A and D sharing one colour scale in Figure 36 and the remaining panels sharing another colour scale in Figure 37.

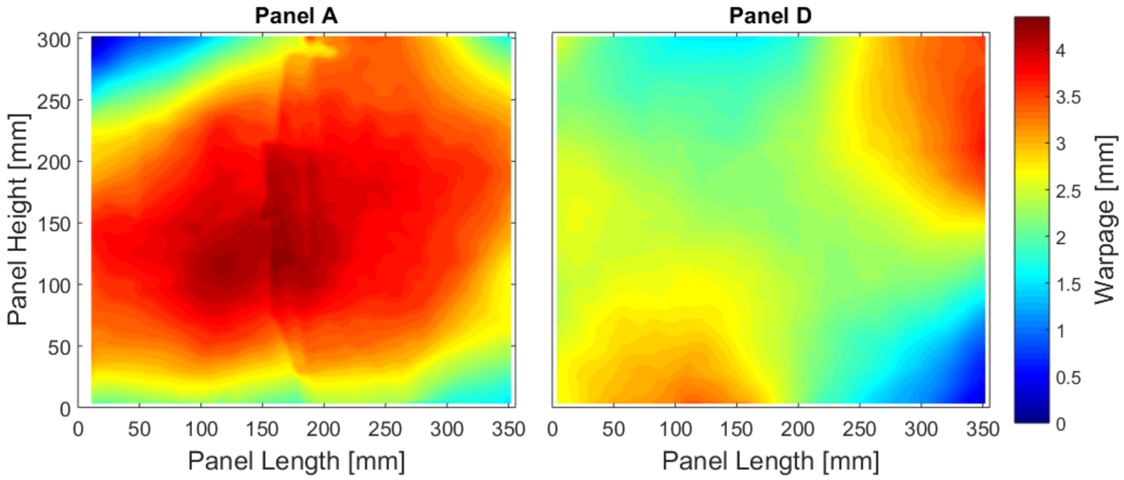

Figure 36: Warped shape of 304.8 mm x 355.6 mm panels with between 3.90 mm and 4.35 mm of warpage.

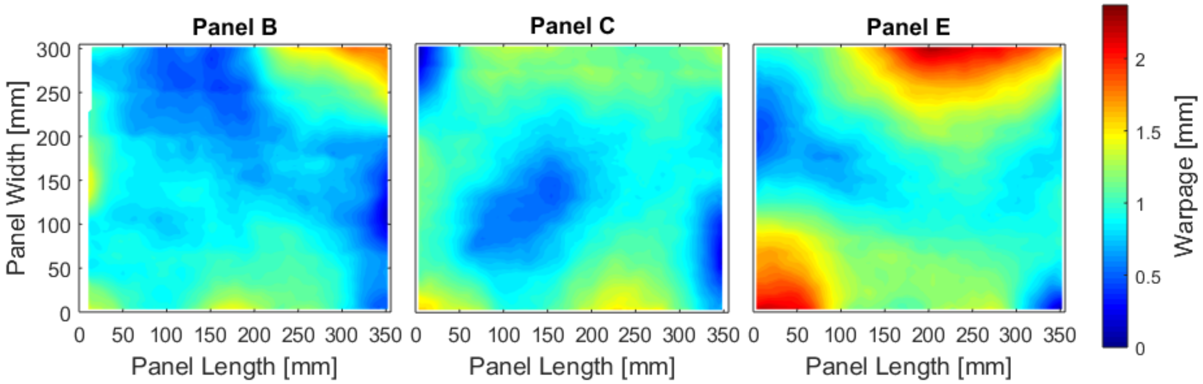

Figure 37: Warped shape of 304.8 mm x 355.6 mm panels with between 1.63 mm and 2.37 mm of warpage.

2.2.2.4 Non-Dimensionalization of Warpage for Comparison between Panel Sizes

As none of the large plates had consistent shapes, the method chosen to non-dimensionalize the data was to normalize the deviation between the absolute maximum and minimum on each plate against the distance between these points. These non-dimensional measurements are presented in Figure 38, where it is apparent that three of the plates had warpage/length measurements similar to those seen in the 101.6 mm x 101.6 mm panels. Panels A and D had significantly more warpage/length.

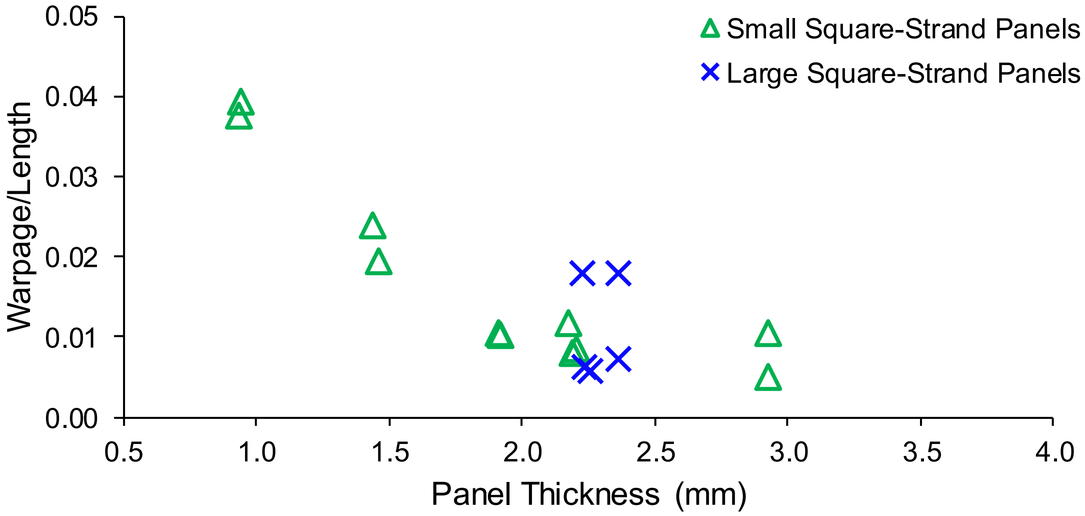

Figure 38: Warpage per unit length, taken as the difference in maximum and minimum out-of-plane deviation normalized against the distance between maxima and minima for plates made with square strands.

Overall, the large panels produced showed more variation, particularly in warped shape, than the small panels discussed in Section 2.1.2. Since consistent processing conditions were applied between panels, the random strand distribution is believed to dominate the warpage pattern. Producing larger, thin panels appears to create more possibilities for how the part can warp.

2.3 Flat Plate Warpage Simulation

A preliminary model to predict warpage within 101.6 mm x 101.6 mm flat plates was developed to determine if the trends seen in Section 2.1.2 could be reproduced. First, a thermal model of the small instrumented hot press was created. Then, thermal data from the hot press model was used to simulate the stress-development and resulting warpage in the flat plates, as captured in the flowchart in Figure 39. This model combines the simulation developed by Landry in [63], incorporating temperature-dependent properties for the DLF material as it cools, and the model developed by Selezneva in [66] for strand distribution, as a first step towards warpage prediction. The model development will be outlined, highlighting the trends seen in predicted results.

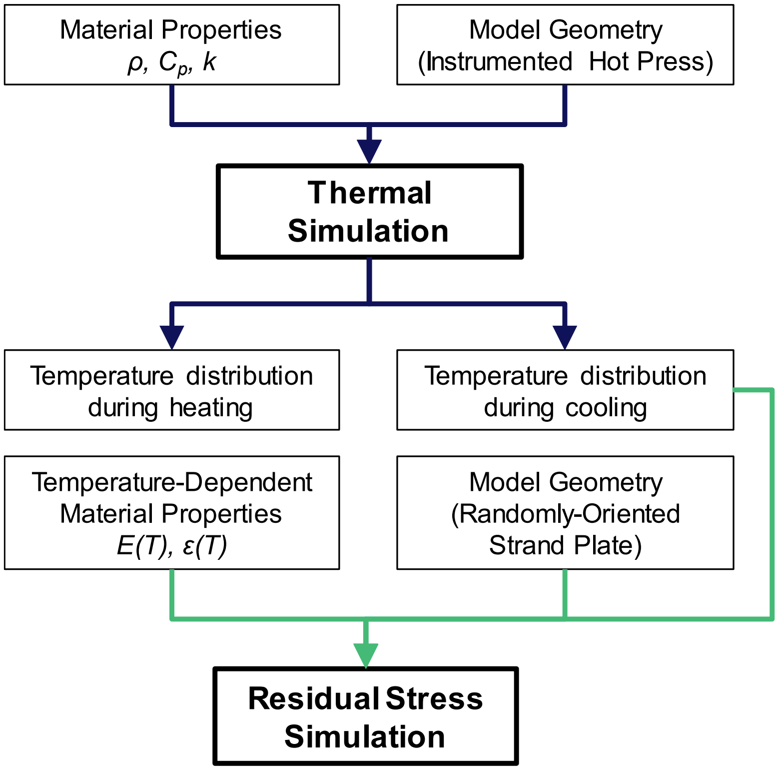

Figure 39: Simulation work flow.

2.3.1 Thermal Model Development and Assumptions

The 3D model captures the geometry of the instrumented hot press used in Section 2.1.1.2 to mould small flat plates. The model includes the press platens, the picture frame mould, 25.4 mm thick ceramic glass insulation surrounding the platens, and 6 mm thick steel plates, placed as they are in the instrumented hot press, and as pictured in Figure 40. The picture frame, press platens, and 6 mm plates on either side of the ceramic glass insulation are made of H13 steel. Channels in the platens for heating cartridges and cooling channels are left empty. The surfaces of these channels are used for heating and cooling load conditions, respectively.

The full press was modeled, as the strand distribution in the composite plate does not have any planes of symmetry. To simplify geometry, bolted connections were removed from the model setup.

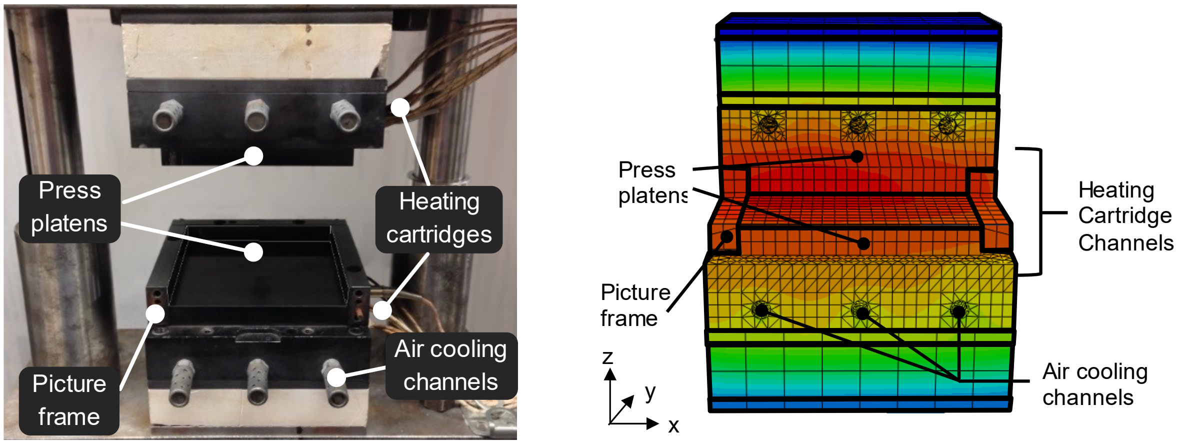

(a) (b)

Figure 40: (a) Physical instrumented hot press and (b) model of hot press used for simulation.

The instrumented press dimensions were fixed, but the composite plate was given variable thickness. The model undergoes heating to the moulding temperature of 380°C, by applying thermal loads to the surfaces of each heating channel, to establish the initial thermal gradient within the plate. Subsequently, the model is cooled down through forced convection through the cooling channels such that the material cools at a rate of approximately 10°C/min until it reaches ambient temperature, maintaining a thermal gradient between the centre and edges of the plate. The thermal data from the cooling step is used as an input to the subsequent stress model.

Similar to the approach taken by Landry in [63], the following key assumptions were made:

- The press platens are parallel;
- The DLF material charge does not change shape throughout the thermal simulation - it is initiated and ends as a plate of constant thickness, neglecting material flow; and
- The DLF material has isotropic conductivity, in plane.

2.3.2 Elements and Boundary Conditions

For the thermal model, linear heat transfer elements were used. The majority of the elements were brick elements (DC3D8) with tetrahedral elements surrounding the channels in the platens (DC3D4). The use of linear elements was shown to yield results within a few degrees of the empirical data, as captured in Section 2.3.3

Each contacting surface was assumed to have surface-to-surface contact, without sliding or smoothing. Contact conductance was set between all surfaces, reflecting intimate contact between surfaces. As well, all external surfaces were exposed to free convection and radiation.

2.3.3 **Comparison with Empirical Results**

The results of the thermal simulation were compared to experimental results collected by Landry in [63]. Experimental results were available for the top surface of the plate at 18 thermocouple locations, as detailed in Figure 41.

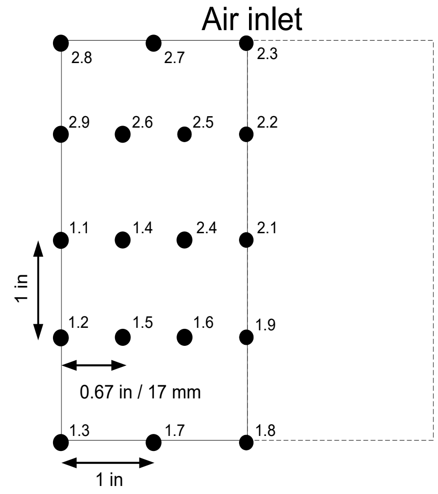

Figure 41: Network of thermocouples used to acquire experimental data [63].

The simulated data fits closely with the empirical data, particularly below 350°C when it becomes critical. As seen in Figure 42, the temperature data gathered near the centre of the plate fits best, with at most, a 1°C deviation at thermocouples 1.9, 2.1, and 2.4.

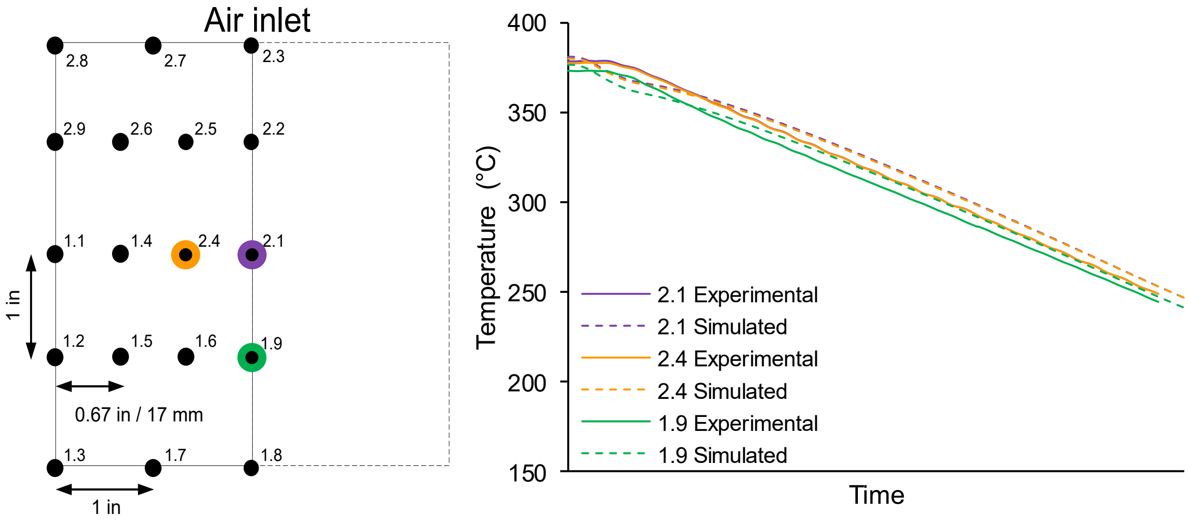

Figure 42: Comparison of simulated to experimental temperature data nearest centre of plate.

The temperature data deviates most at the corners where the experimental data shows the panel to cool a bit faster than the simulated data as seen in Figure 43. The variation at the bottom corner, 1.3, is about 6°C, but the variation at the top corner is as high as 10°C.

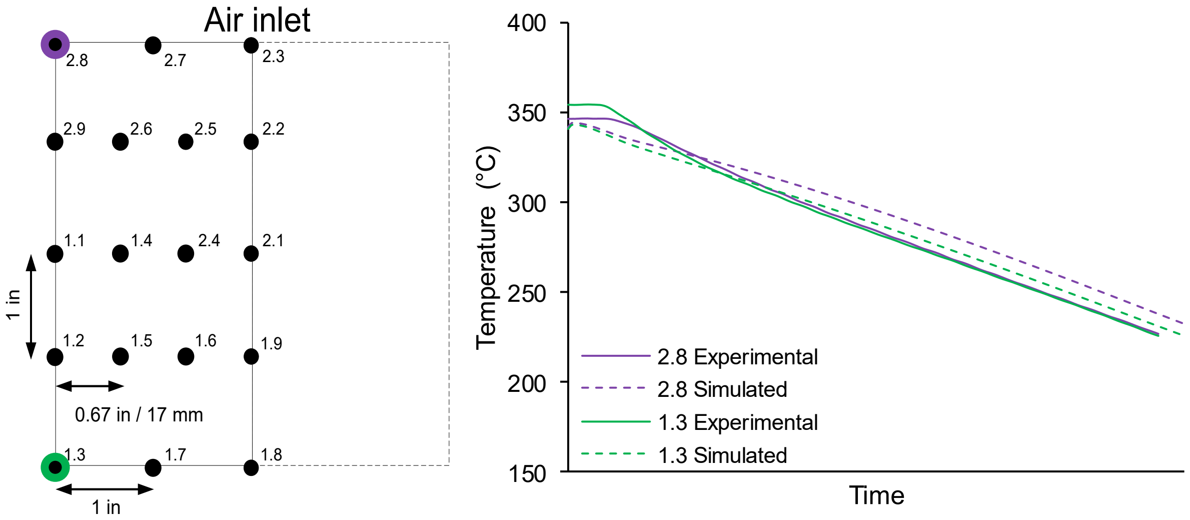

Figure 43: Comparison of simulated to experimental temperature data at corners.

2.3.4 **Stress Model Development and Assumptions**

The stress model focussed solely on the composite plate, between rigid platen surfaces as pictured in Figure 44. This setup mimicked the geometry established by Landry in [63]. The full plate was modelled, as its heterogeneous properties do not allow for a plane of symmetry. The plate thickness was set to vary with the plate thickness selected for the thermal model.

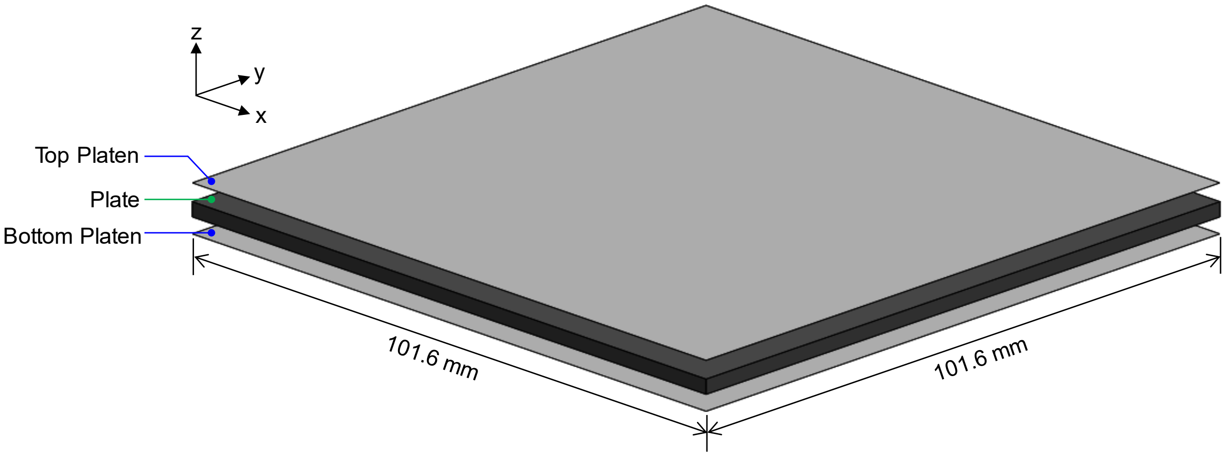

Figure 44: Model geometry used for stress model.

The stress model expanded on the temperature-dependent pressure distribution model established by Landry in [63]. The temperature distribution during cooling generated by the thermal model was applied to the composite plate. Temperature-dependent properties for material modulus and shrinkage were input, based on models developed by Landry in [63] and extended until the material reached ambient temperature. At each time step, the instantaneous stiffness and shrinkage within the plate contribute to developing residual stresses. At the end of the simulation, the deformed state of the composite plate is recorded. The process flow of the model is captured in Figure 45.

Just as in the thermal model, several assumptions were applied:

- The press platens are assumed to be perfectly parallel, rigid bodies with negligible thermal expansion;
- The DLF strands are assumed to be distributed fully in-plane, without any out-of-plane orientation or waviness;
- The DLF material charge does not change shape throughout the thermal simulation - it is initiated and ends as a plate of constant thickness, neglecting material flow; and
- Defects, such as voids and resin-rich regions, are ignored.

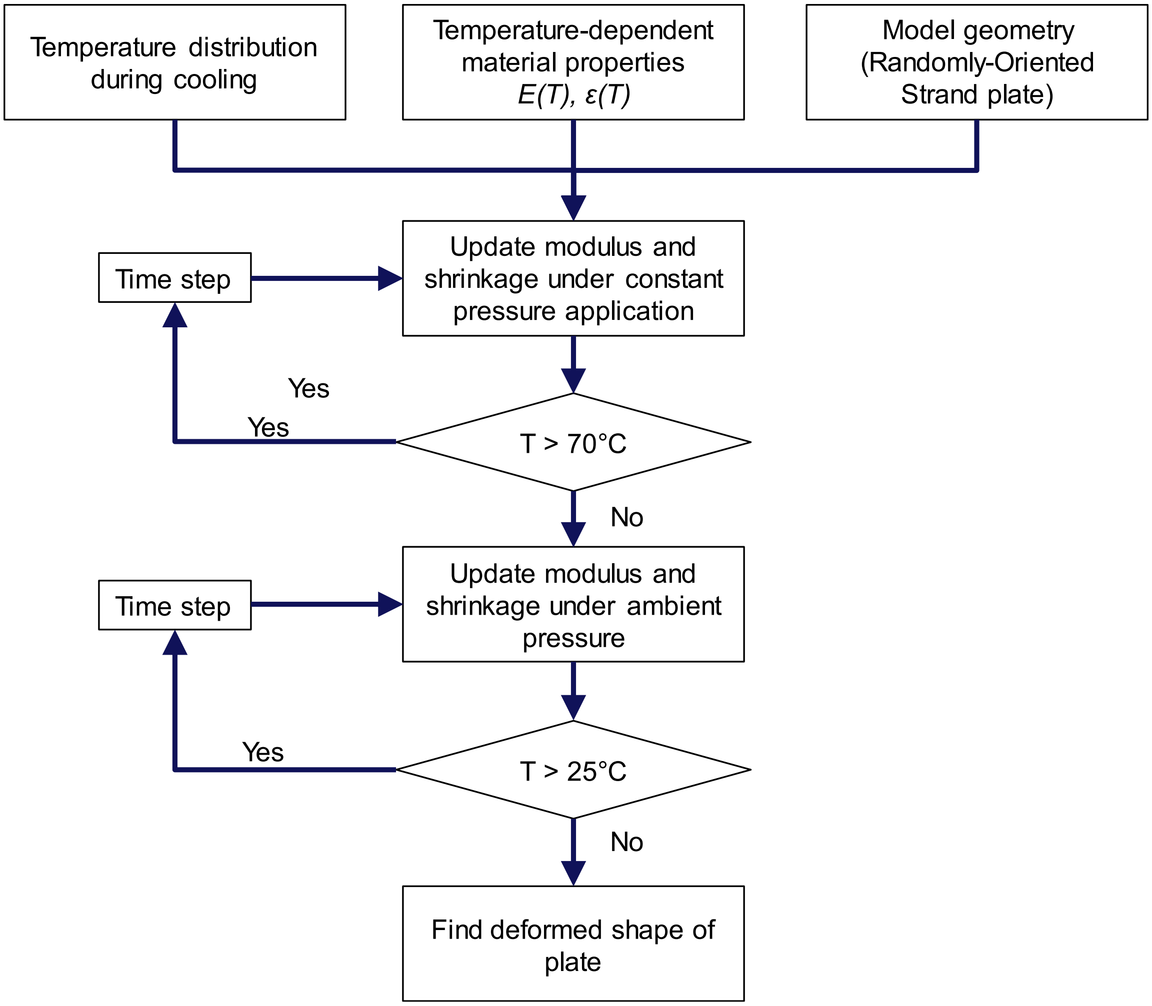

Figure 45: Process flow of stress model, showing inputs and outputs.

2.3.4.1 Temperature-Dependent Elastic Properties

The elastic properties of the PEEK matrix are highly temperature dependent. Transitioning from melt temperature to ambient temperature, the modulus first sees a significant increase during crystallization, as the polymer chains organize. Cooling beyond the range of crystallization, the modulus continues to increase at a reduced rate until the temperature is within range of the glass transition temperature. The modulus increases most during this transition, with marginal gains once the part is cooled below T_g.

Data for the out-of-plane elastic modulus of carbon/PEEK, when cooled at 10°C/min, was collected by Landry in [63] through dynamic mechanical analysis. In [63], this data was subsequently used to create a step-wise polynomial model for the temperature-dependent matrix modulus. The transverse and out-of-plane moduli (E_{yy}, E_{zz}) were calculated using this temperature-dependent matrix modulus and the inverse rule of mixtures as shown in Equation 1. The results were plotted against the empirical data in Figure 46 to affirm the calculation for the temperature-dependent matrix modulus. The depicted model and data matches well with data recorded for AS4/PEEK by Barnes and Byerly [55]. For this equation, the modulus of carbon fibre was assumed constant at 21 GPa, as it was in [63].

$$E_{yy}(T) = E_{zz}(T) = \left(\frac{V_f}{E_f} + \frac{1 - V_f}{E_m(T)}\right)^{-1} \qquad (1)$$

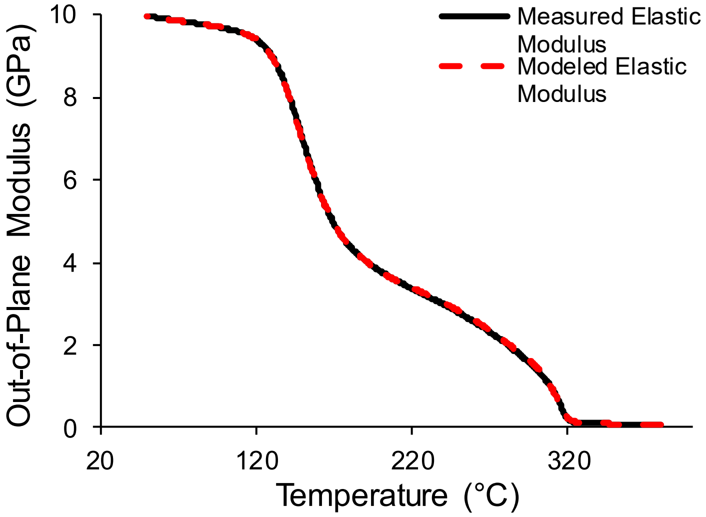

Figure 46: Modeled transverse and out-of-plane elastic modulus for carbon/PEEK cooled at 10°C/min (measured properties from [63]).

To determine the longitudinal modulus (E_{xx}), the previously found temperature-dependent matrix modulus was used with the rule of mixtures as shown in Equation 2 and plotted in Figure 47. The tensile modulus of carbon fibre was assumed to be 231 GPa [67], creating a room temperature longitudinal modulus near the empirical value of 138 GPa reported in [68] for AS4/PEEK.

$$E_{xx}(T) = V_f E_f + \left(1 - V_f\right) E_m(T) \qquad (2)$$

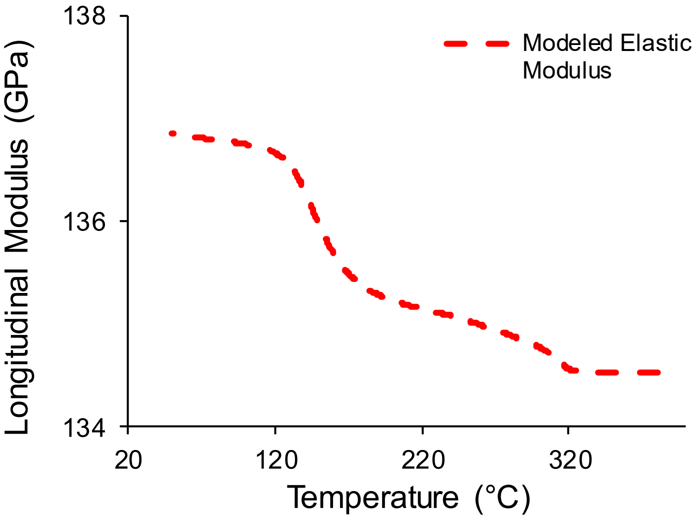

Figure 47: Modeled longitudinal elastic modulus for carbon/PEEK cooled at 10°C/min.

Keeping conditions consistent with work done in [63], the Poisson's ratio is assumed to be constant in all directions, regardless of temperature.

$$\nu_{xy} = \nu_{yz} = \nu_{xz} = 0.33 \tag{3}$$

The in-plane shear modulus is assumed to be the longitudinal shear modulus, divided by twice the Poisson's ratio plus 1, per [68].

$$G_{xy}(T) = \frac{E_{xx}(T)}{2(1+\nu)} \tag{4}$$

Following Landry's model [63], the out-of-plane shear moduli are assumed to react proportionally to the out-of-plane elastic modulus. The typical shear modulus of carbon/PEEK is 7.1 GPa at room temperature [68]. This shear modulus is effectively scaled with the reduction in out-of-plane modulus at temperature by multiplying the typical shear modulus by the fraction of at-temperature out-of-plane modulus to ambient-temperature out-of-plane modulus (10 GPa).

$$G_{xz}(T) = G_{yz}(T) = 7.1\ \text{GPa}\,\frac{E_{zz}(T)}{10\ \text{GPa}} \tag{5}$$

2.3.4.2 Thermal Strain Properties

Landry captured out-of-plane thermal strain for the cooling cycle of carbon/PEEK using thermomechanical analysis in [63]. This thermal strain incorporates strain from material shrinkage and from the material's coefficient of thermal expansion. His results are pictured in Figure 48. As ABAQUS does not take direct thermal strain inputs, Landry's data was discretized into instantaneous coefficient of thermal expansion data for the out-of-plane direction, assuming a reference temperature of 348°C. So, the data was entered into the model as CTE data, but it reflects overall thermal strain.

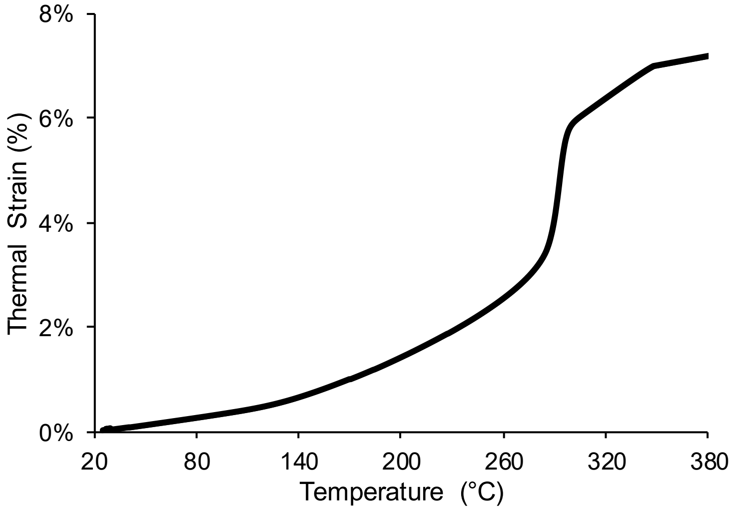

Figure 48: Transverse and out-of-plane thermal strains (experimental data from [63]).

The transverse thermal strain was assumed to be equal to the thermal strain in the out-of-plane direction. The longitudinal thermal strain was assumed constant at a literature value for longitudinal CTE in carbon/PEEK of 0.24 x 10^{-6} /°C in the fibre direction.

2.3.4.3 Strand Distribution Model

The strand distribution model developed by Selezneva in [66] was used to create each simulated plate's unique layup. Using Selezneva's MATLAB program, the plate was divided into a set number of partitions, based on its intended mesh size, and each strand was discretized into elements of the same width and length. Each strand was rotated at a random angle and deposited at a random location within the plate as shown in Figure 49. This process continued until the target number of strands was used. So, each partition of the composite plate had its own unique layup. The plate thickness was held constant, but the number of strands in each section was variable. So, the input for strand thickness can vary between elements.

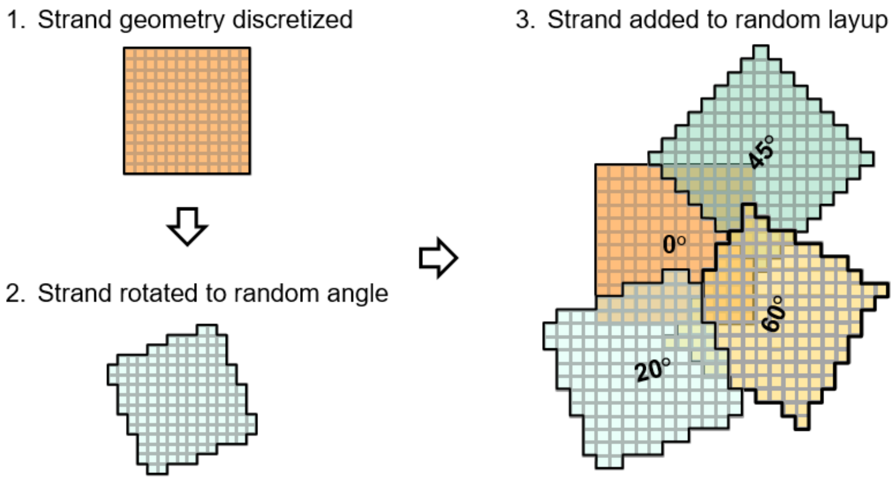

Figure 49: Simplified schematic of strand distribution input.

This discretized series of elements with random strand orientations was directly read into ABAQUS, such that each element of the composite plate had unique properties.

2.3.5 Elements and Boundary Conditions

The elements used to model the plate geometry are solid 3D quadratic stress elements with 20 nodes each (C3D20R). The number of elements is set to match the number of elements generated in the thermal model, such that the temperature data transfers appropriately. The number of elements directly impacts the randomized strand distribution input into the model. As demonstrated in Figure 50, using a finer mesh size creates a more representative discretization for the strand inputs.

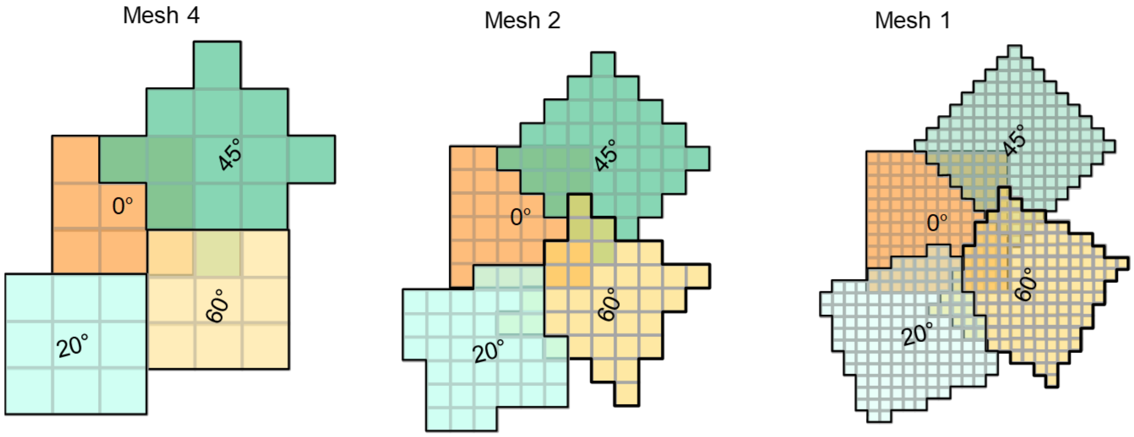

Figure 50: Schematic showing strand dependence on mesh size.

The elements used to represent the platens are discrete rigid elements (R3D4). These elements are described in ABAQUS as “4-node 3-D bilinear rigid quadrilaterals.”

The boundary conditions implemented on the stress model mimicked those used in Landry's pressure model in [63], with the bottom platen fully fixed and the top platen free to slide in the *z*-direction only, maintaining the assumption of parallelism. The composite is restricted on its sides where it would interact with the picture frame mould, stopping it from moving normal to its contact with the picture frame. The boundary conditions are pictured in Figure 51.

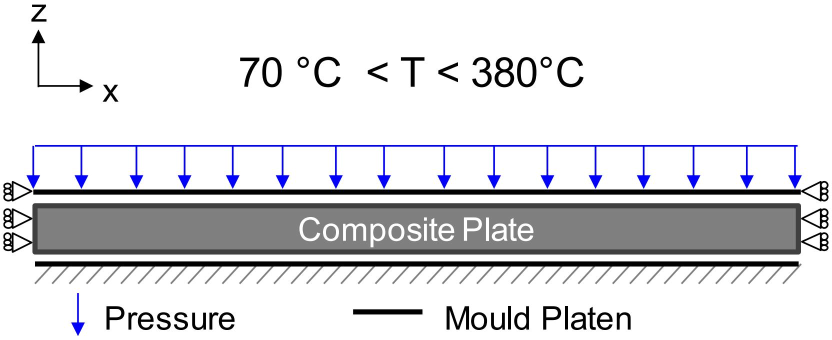

Figure 51: Schematic of boundary conditions in stress model.

As the composite plate progresses through its cooling simulation, constant pressure is applied to the top platen. To mimic what was done in experiments, 70 bar of pressure is applied to the top platen. Contact between the platens and the composite plate is modelled at two extremes. The first extreme assumes hard contact normal to the plate, but frictionless contact tangential to the plate, effectively neglecting the effects of tool-part interaction. At a second extreme, the contact between plate and platens is modeled as fully adhesive – effectively as infinite friction. These two extremes act as upper and lower bounds for the level of warpage that can be predicted with this model. When the plate temperature drops below approximately 70°C, the pressure is released and the plate is no longer in contact with the modelled platens. Only the boundary conditions on each edge of the plate are maintained as seen in Figure 52.

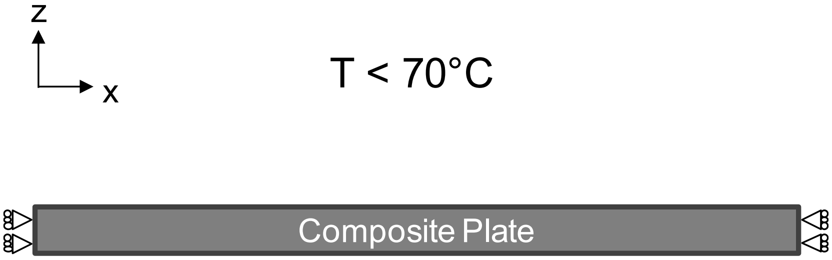

Figure 52: Schematic of boundary conditions in stress model.

2.3.6 Comparison of Modelled Plate Warpage with Experimental Results

Looking at the results of the warpage simulation, similarities are seen between the warpage results and experimental data. First, the composite plate is predicted to warp differently in each simulated scenario, similar to what was seen in practice – again emphasizing the link between the random strand distribution and the inconsistencies seen in warpage. As well, the trends found in simulated panels mimicked what has been seen experimentally – the amount of warpage decreases as panel thickness increases. However, the magnitude of the warpage was not predicted accurately. The results, assuming a mesh size of 2 (creating 2 mm x 2 mm elements) are shown in Figure 53.

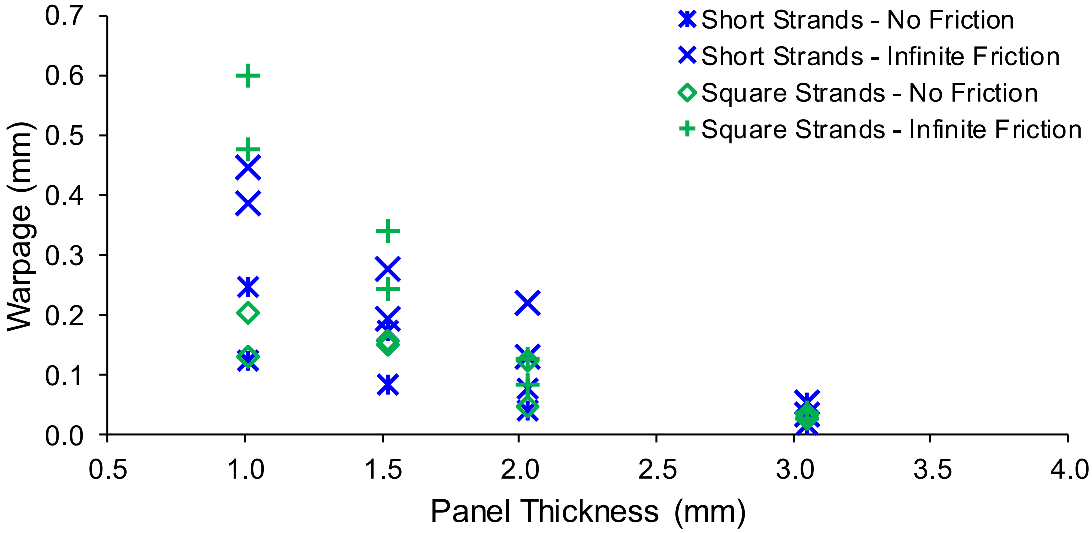

Figure 53: Comparison of simulated warpage results in (a) frictionless and (b) infinite friction case.

As seen in Figure 53, the predicted warpage with no friction is lower than the predicted warpage with infinite friction, indicating that tertiary residual stresses from the friction between the composite plate and the tooling during cool down contribute to warpage. This is furthered by the warped pattern displayed in Figure 54 below, where one simulated DLF distribution for a 2.3 mm thick plate made with square strands is pictured in its warped condition both with and without friction. In the frictionless state, the centre of the plate is its lowest point. Only its corners and edges curl up to create warpage. This was representative of all warpage predictions without friction. In the infinite friction case, the warped plate has corners and edges that curl both up and down. This was representative of all warpage predictions made in the infinite friction state. The shape of the infinite friction case is more representative of shapes seen experimentally.

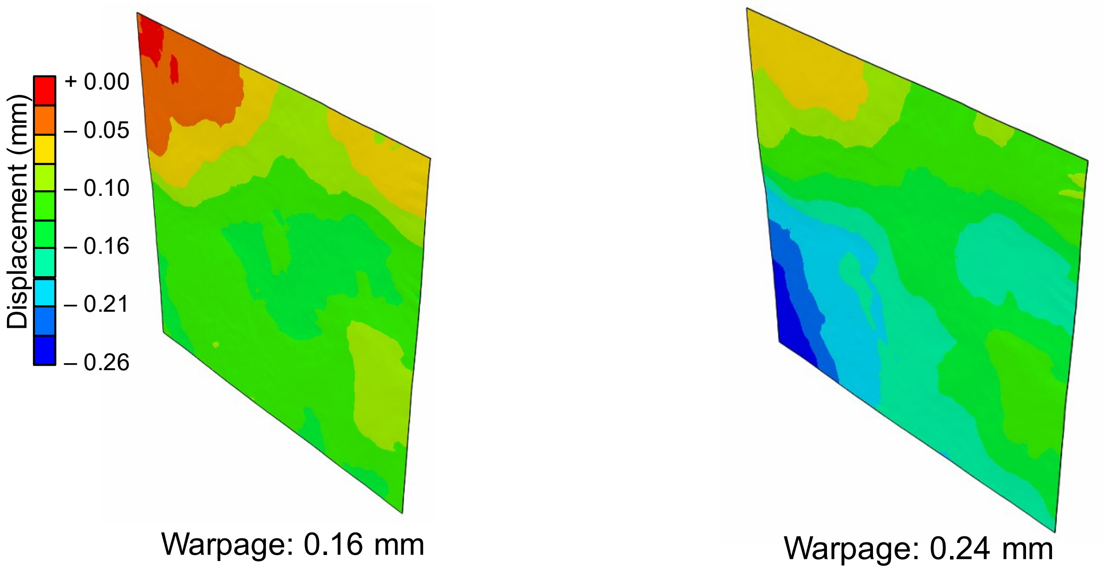

(a) (b)

Figure 54: Comparison of simulated warpage results in (a) frictionless and (b) infinite friction case for square-strand, 1.5 mm thick, small plates with identical layup inputs.

The magnitude with which tertiary residual stresses contribute to warpage, compared to primary and secondary residual stresses, is unknown. However, since both simulated and experimental plates warp in different ways each time they are made under the same processing conditions, the primary and secondary residual stresses – those coming from interactions between the fibres and matrix independent of moulding conditions – appear to dominate in determining the final part shape.

Comparing the simulated results to the experimental in Figure 55, the simulation significantly under-predicts part warpage. At this level, the simulation is only indicative of trends in part warpage.

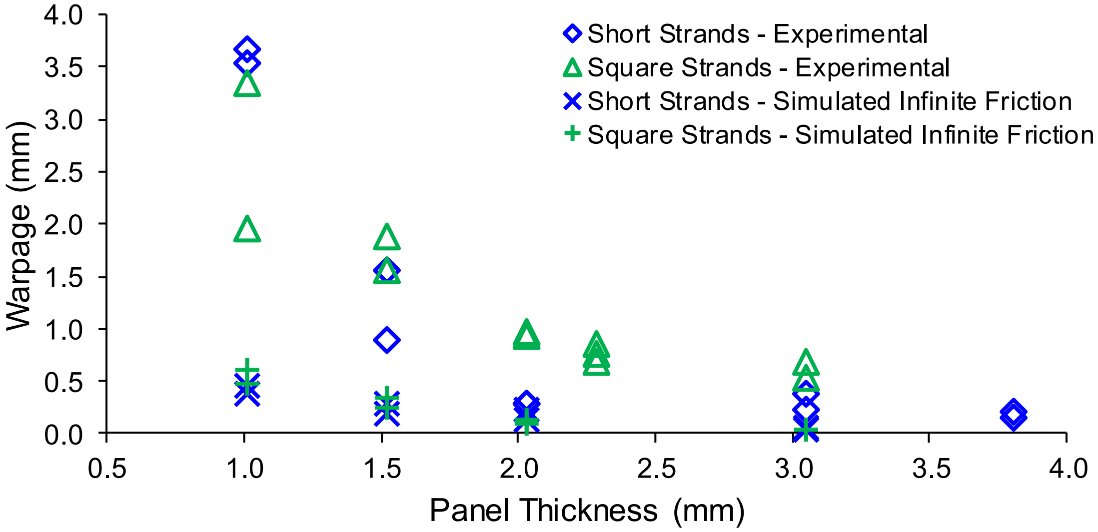

Figure 55: Comparison of simulated and experimental warpage results.

2.4 Summary and Conclusions

In this chapter, a series of small 101.6 mm x 101.6 mm flat plates were made under consistent processing conditions, varying strand size and plate thickness. From this experimental work, four aspects of warpage produced in DLF parts became clear:

1. Plates made <2.0 mm thick suffered from significant warpage, with significant variation part-to-part. It is not recommended to use DLF material for sections thinner than 2.0 mm unless dimensional stability is not a part requirement.
2. Plates made with 6.35 mm x 3.18 mm strands warped less than plates made with 12.70 mm x 12.70 mm strands. This is consistent with the findings of Selezneva and Lessard in [14] and believed to be a function of the smaller material's relative homogeneity compared to the larger material. As well, it is notable that the magnitude of warpage in the parts made with 6.35 mm x 3.18 mm strands stabilizes and remains relatively constant for parts 2.0 mm thick and thicker.
3. Each plate warped differently, indicating that the random strand distribution has a dominant effect on part warpage and affirming the assertions of Hufenbach and Gude [69] that crystalline shrinkage has a more dominant effect on carbon/PEEK part warpage than thermal gradients.

While many of the parts took on saddle-like shapes, the orientation of the saddle was inconsistent. As well, approximately 40% of the parts did not resemble saddles, having several randomly-located local maxima and minima. This inconsistency creates difficulty in establishing a metric for comparing warpage between plates of different sizes. As well, it creates a level of futility in predicting the shape of part warpage, as the shape of thin-gauge, featureless parts will be different each time.

4. Finally, warpage was shown to reduce with increasing plate thickness, as this directly correlates to an increase in plate stiffness.

In moulding a series of 2.3 mm thick, 304.8 mm x 355.6 mm flat plates using square strands, the above-mentioned warped shape inconsistency was further verified. Each plate presented warped in a different shape, despite consistent processing conditions and thickness distributions between parts. Using a non-dimensional metric based on the total out-of-plane deviation, normalized against the distance between maximum and minimum points, three of the five discussed large plates had similar warpage metrics to the small plates of near-equivalent thickness. The remaining two plates had significantly higher warpage, despite consistent processing conditions.

Finally, a preliminary simulation of processing conditions and warpage in the 101.6 mm x 101.6 mm plates was performed, again verifying that part warpage is dominated by strand distribution, as each simulated plate presented a different warped shape. As well, the simulation mimicked trends seen in experimental parts, showing a reduction in warpage for increasing plate thickness. Further efforts to reduce warpage by increasing stiffness will be pursued in Chapter 3.

3. Processing Investigation – Ribbed Panels

From the findings of Selezneva and Lessard [14] and the work done in Chapter 2 of this thesis, it is apparent that the degree of warpage in flat panels decreases with increasing panel thickness. Effectively, warpage decreases with increasing panel stiffness. It is desirable to reduce warpage, so it is desirable to increase stiffness. However, further incremental increases in part thickness can significantly increase the overall part weight. To increase stiffness without significantly increasing weight, the use of ribs will be explored. Ribs can greatly increase a part's stiffness by greatly increasing its moment of inertia, as seen in Figure 56.

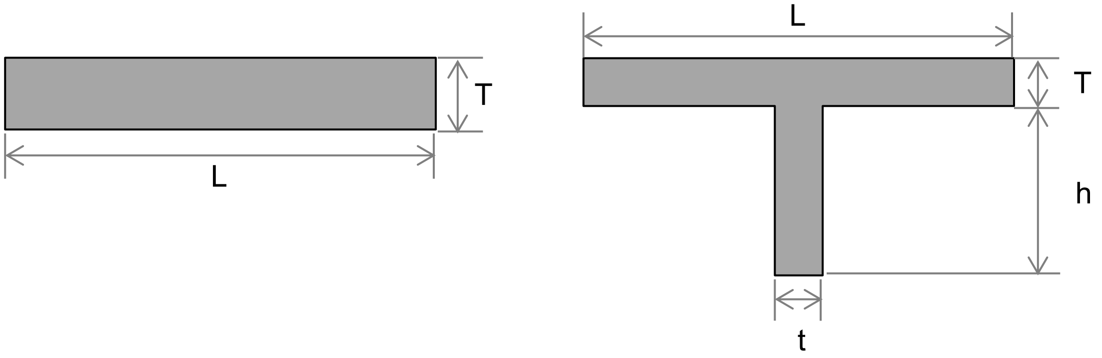

$$I = \frac{LT^3}{12}$$

(a)

$$I = \frac{LT^3}{12} + \frac{th^3}{12} + th\left(\frac{h+T}{2}\right)^2$$

(b)

Figure 56: Comparison of moment of inertia between (a) a flat panel and (b) a panel with ribs.

This chapter will explore the use of ribs as a means of mitigating warpage. First, an idealization of potential geometries is presented in Section 3.1 where a baseline ribbed geometry is established by referencing typical injection-moulded geometries and assuming homogeneous, isotropic material properties. As the part will be made by compression moulding, with DLF material, the problem was then explored experimentally. In Section 3.2, experimental investigation of parameters necessary to successfully fill small ribbed features will be explored, focussing on the minimum fill pressure and the processing conditions necessary to produce parts free of surface defects, respectively. Finally, in Section 3.3, a ribbed part is manufactured to explore the effect of ribs on the overall part warpage.

3.1 Ribbed Panel Geometric Investigation

It is desirable to increase the stiffness of the DLF panels as much as possible while maintaining their weight. As a preliminary investigation into optimum rib geometry, homogeneous and isotropic properties were assumed. A parametric study was run, varying rib number and rib geometry to increase the moment of inertia and maintain the weight of the baseline design. The baseline design was considered to be a flat plate with T = 2.3 mm.

3.1.1 **Geometry Considerations**

As ribs are common to injection-moulded part design, there are many existing design standards to restrict the possible rib geometry. From a few of these sources [70, 71], the following parameters were determined to be important:

1. Rib thickness (t) should not exceed more than half of plate thickness (T) [70, 71], unless T < 1.5 mm. This is intended to prevent dimpling/sink marks on the part.
2. Ribs should not be < 1 mm thick [70].
3. Rib height (d) should not be more than three times rib thickness (t) [70, 71].
4. Spacing between ribs should be at least twice panel thickness (T) [71].
5. For part ejection, ribs should have a draft angle of at least 0.5°[70, 71], but draft angle should not exceed 1°[70].
6. The corner radius of the rib should be greater than (0.25 mm – 0.4T) [71].

These guidelines were considered as limitations of the allowable rib designs used in a MATLAB optimisation study. Since the desirable plate thickness (T) is small and potentially close to 1.5 mm, separate optimisation runs for rib geometry were performed with the restriction $t \leq 0.5$ T and with the restriction $t \leq T$. As well, the lower bound for rib thickness was set at 1.0 mm. The minimum plate thickness was set at 1.8 mm, to fit allowable geometries that a client sponsor was considering. The maximum rib height was restricted to 3.8 mm to fit within the geometric envelope of an existing part. Ribs were considered in a grid pattern, as pictured in Figure 57, to better resist warpage in all directions. The ribs considered remained evenly spaced, but were considered to occur in both perpendicular directions (effectively “ribs per inch” x “ribs per inch”).

3.1.2 **Parametric Study Results**

Using the geometry considerations outlined above, optimisation runs were performed in MATLAB to determine the rib geometry and number of evenly spaced ribs (per inch) that would provide:

1. An increase in moment of inertia while maintaining the baseline mass of the part, or
2. A decrease in mass while maintaining the baseline moment of inertia of the part.

500 random initial guesses were used to initiate the runs and many ended at the same optimum points. From these runs, the best results for increasing moment of inertia were obtained when the maximum rib dimensions were used, as captured in Table 5. When minimizing mass, the smallest ribs with the greatest height-to-thickness ratio were found to be best. From these results, it is clear that adding ribs to a homogeneous material can significantly increase stiffness without increasing mass. As well, mass can be reduced without negatively impacting stiffness.

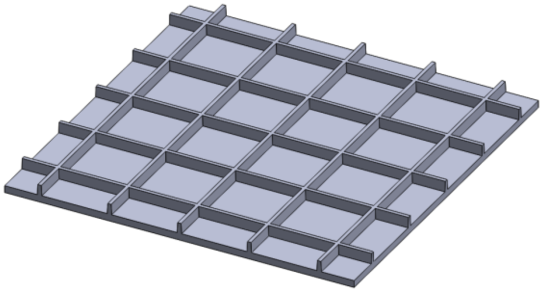

Figure 57: Evenly-spaced ribs in perpendicular directions.

Table 5: Summary of optimum rib dimensions, with relative moment of inertia and relative mass provided as compared to a homogeneous, 2.3 mm thick, flat plate.

Goal	Restriction	Plate Thickness, T (in)	Rib Thickness, t (in)	Rib Height, d (in)	Number of Ribs per Inch	Relative Moment of Inertia	Relative Mass
Maximize Moment of Inertia	t ≤ 0.5T	1.8	1.0	3.0	2	209%	98%
	t ≤ T	1.8	1.8	3.8	1	289%	100%
Minimize Mass	t ≤ 0.5T	1.8	1.0	3.0	1	128%	88%
	t ≤ T	1.8	1.0	3.0	1	128%	88%

As highlighted in Table 5, two sizes of ribs emerged as the best candidates for increasing part stiffness while minimizing mass – ribs 1.0 mm thick x 3.0 mm deep and ribs 1.8 mm thick x 3.8 mm deep. To pursue the creation of parts with these ribs, the processing conditions necessary to ensure that the ribs filled completely with material, without defects, must be understood. Necessary fill requirements, processing pressures, and cooling strategies to attain successfully filled ribs are outlined in the Section 3.2. The processing parameters determined in this section will then be used to create parts with evenly spaced ribs in perpendicular directions to determine the effect of ribs on final part warpage in Section 3.3.

3.2 Ribbed Panel Process Development

The objectives of the ribbed panel process development assessment were to verify necessary pressures for rib filling and determine moulding pressures and cooling strategies necessary to create smooth part surfaces, free of surface voids. Rib filling pressure was confirmed through experimentation, as discussed in Section 3.2.1 and evaluated using microscopy. Additional pressure and cooling strategies were necessary to ensure part surfaces with good surface finishes, as discussed in Section 3.2.2.

3.2.1 **Flow Assessment**

As the goal of adding ribs is to increase stiffness without significantly increasing mass, the ribs will be small, with depths smaller than the strand sizes used to fill them. As such, the material will have to flow into the ribs, creating potential complications. First, the pressure needed to fill the ribs must be determined. As well, having the material flow into the ribs may create surface defects like knit lines [68] or sink marks [70], that will act as weak points against stress. So, fill tests will be conducted to verify fill pressure and ensure that the rib geometry does not create further defects.

Flow studies with DLF material on similarly shallow ribs have been conducted by Lee et al [72] and Kobayashi et al [73], using ultra-thin carbon-fibre/polyamide 6 tapes. Flow tests with carbon/PEEK tapes were performed by LeBlanc et al in [74], where a processing envelope for filling a 3.3 mm wide, 25.4 mm deep rib was proposed. The work done by LeBlanc was used as a baseline in this work, but had to be verified for these shorter ribs.

3.2.1.1 Mould Geometry

To verify flow conditions for rib filling and identify any additional moulding challenges associated with the addition of ribs, parts with four parallel ribs were made. Two of the ribs were those identified in Table 5, with potential for increasing moment of inertia and reducing mass relative to the baseline 2.3 mm thick flat plate. A third rib maintained the 1.8 mm prescribed width, but increased the height of the rib to three times its thickness, for a final height of 5.3 mm. The fourth rib was chosen to be 2.5 mm wide, as this value fit incrementally between the other ribs tested and the width of 3.3 mm tested by LeBlanc in [74]. This fourth rib's height was three times its thickness as well: 7.6 mm. Each rib had a small radius at its entrance of approximately 0.5 mm and a draft angle of 3°. The rib geometry and configuration is summarized in Figure 58. Each rib will subsequently be referred to by letter name, per Figure 58(a).

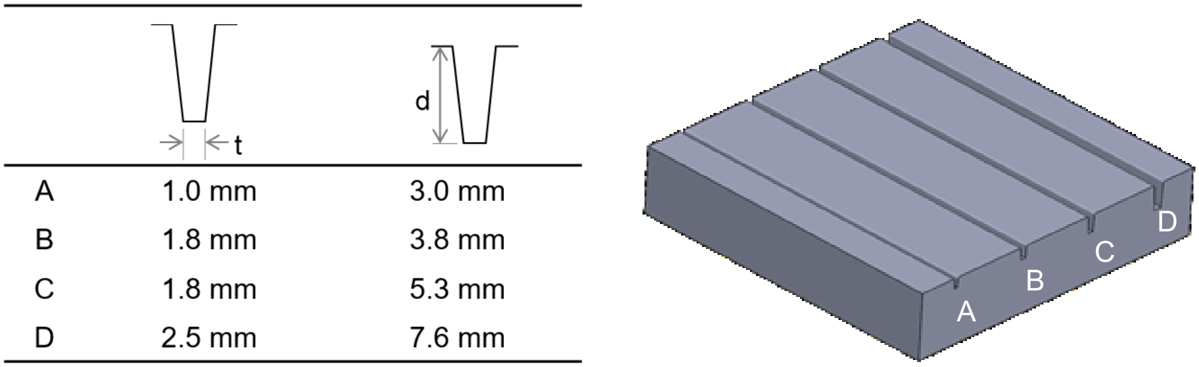

	t	d
A	1.0 mm	3.0 mm
B	1.8 mm	3.8 mm
C	1.8 mm	5.3 mm
D	2.5 mm	7.6 mm

(a) (b)

Figure 58: Rib sizes tested for filling showing (a) dimensions and (b) placement within mould.

3.2.1.2 Material and Strand Distribution

The material used to mould ribbed parts was the same as that used in Chapter 2 to mould flat plates – carbon/PEEK strands chopped at lengths of 6.35 mm x 3.18 mm (short strands) and 12.70 mm x 12.70 mm (square strands). To test rib filling at the shell thickness (T) expected to yield the best results in terms of mass, sufficient material was placed in the mould to yield parts with a 1.8 mm thickness.

3.2.1.3 Test Setup

The test was set up in the instrumented hot press detailed in Section 2.1.1, with a taller picture frame in place. To mould ribs into the plate, inserts were added to the mould platens, as pictured in blue in Figure 59. Ribs were moulded against gravity, oriented as shown.

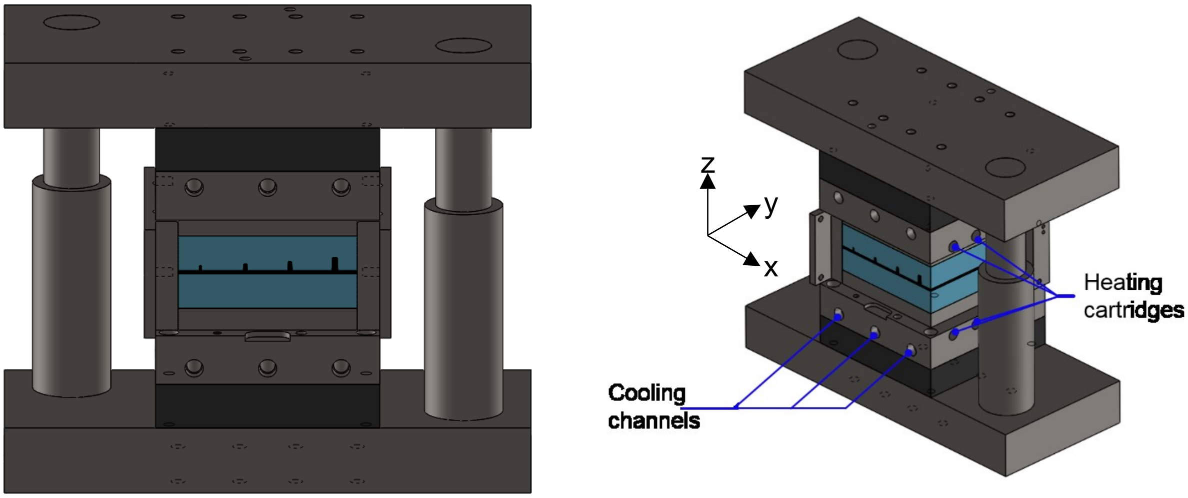

(a) (b)

Figure 59: Rib moulding setup showing (a) front view and (b) isometric view.

3.2.1.4 Procedure and Process Cycle

The moulding procedure mimicked that presented in Section 2.1.1.3. However, the temperature set at the controller and the dwell time were increased to account for the added distance between the DLF material and the thermocouple created by the addition of the moulding inserts. From measurements taken with thermocouples placed at the moulding surfaces, the material temperature is expected to be approximately 20°C below the temperature seen at the thermocouple after a 45-minute dwell. As well, the moulding pressure – applied when material reaches temperature and maintained throughout cooling – was reduced to determine the minimum fill pressure for the ribs. Following the moulding curves suggested in [74], and pictured in Figure 60 and Figure 61, respectively, the initial fill pressure attempted for the short strands was 10 bar. The initial fill pressure attempted for the square strands was 30 bar, assuming flow would be similar to that seen in the longest strands investigated in [74] when used to fill a 3.3 mm x 25.4 mm rib. To account for the 20°C difference between material and temperature controller, parts were moulded with the temperature controller at 400°C and 420°C. As determined in [74] and [17], parts moulded below 70 bar (critical pressure in the instrumented hot press) undergo matrix tearing and have significant surface voids. So, after filling pressure is determined, necessary moulding pressure will be discussed in Section 3.2.2.

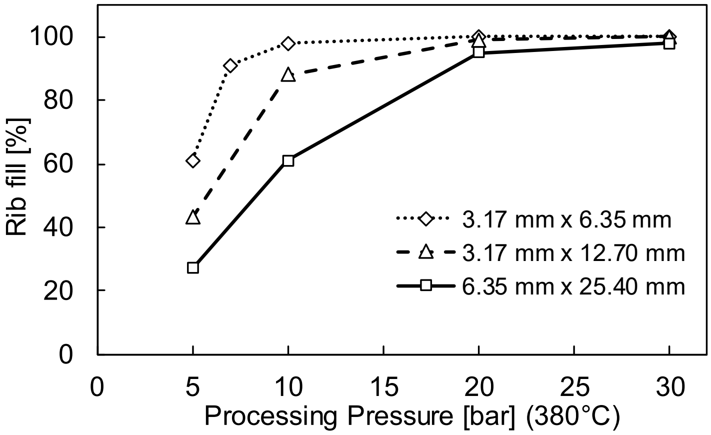

Figure 60: Fill pressure for a 3.3 mm x 25.4 mm rib at 380°C [68].

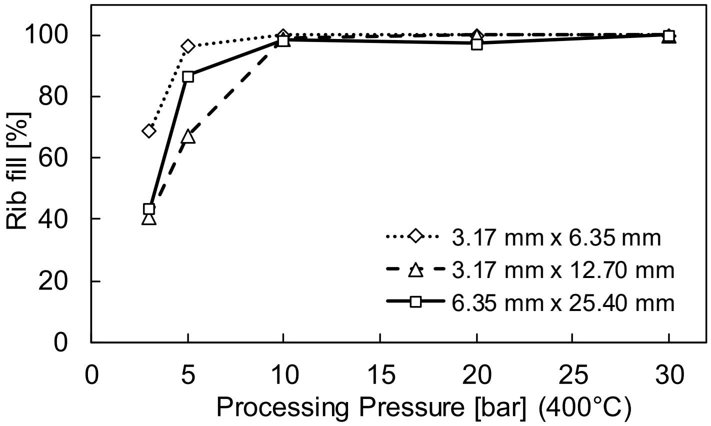

Figure 61: Fill pressure for a 3.3 mm x 25.4 mm rib at 400°C [74].

The process cycle used to test filling on parts made with square strands is depicted in Figure 62.

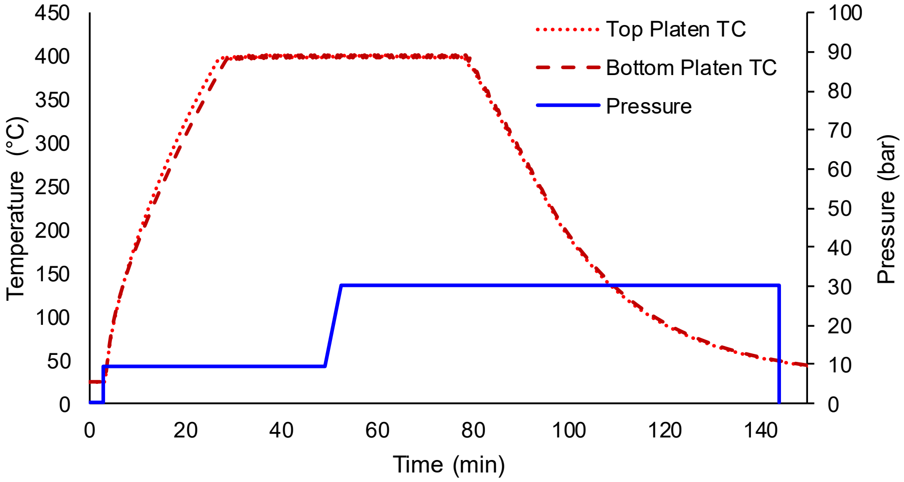

Figure 62: Process cycle to fill ribs of part made with square strands, temperature controller at 400°C.

3.2.1.5 *Visual Assessment*

From this fill pressure assessment, 10 bar was found to be sufficient to fill two of the four ribs in the short strand part. The two middle ribs – ribs B and C – filled completely when moulded at both 400°C and 420°C. Rib A almost filled completely, but showed a dry, unfilled section at its tip. This area of insufficient fill was on the side closest to the cooling channel outlet. Rib D suffered from insufficient fill at both ends, with more sustained on the side closest to the cooling channel outlet. As well, the corner of the part, beside this 2.5 mm x 7.6 mm rib on the cooling outlet side, was dry and poorly consolidated. This uneven filling may be indicative of more than just the fill pressure. From the positioning of the unfilled regions at the corners of the part, it is likely that the insufficient filling is in part due to thermal gradients within the mould. As the corners are cooler than the centre of the part, the viscosity of the material appears to have been too low to sufficiently flow in these regions. As well, the skew of poor consolidation from the cooling inlet to cooling outlet in the part may be indicative of a pressure gradient within the mould. Further evidence of a pressure gradient within the mould is discussed in Section 3.3.1.4 and Appendix B. The short strand part moulded at 10 bar is shown in Figure 63. Regions of insufficient fill are circled in red on Figure 63, and emphasized in Figure 64. When 20 bar of fill pressure was applied, all ribs filled completely with short strands, but exhibit rough, white surfaces indicative of matrix tearing and insufficient pressure during cooling.

Figure 63: Insufficient fill seen in Rib A and Rib D when moulded with short strands at 10 bar filling pressure and 400°C at the temperature controller. Areas of insufficient fill circled in red.


(a) (b) (c)

Figure 64: Insufficient fill seen at (a) cooling outlet side, Rib A; (b) cooling outlet side, Rib D; and (c) cooling inlet side of Rib D.

The initial fill pressure of 30 bar was sufficient to completely fill all ribs with square strands. Small resin-rich regions could be seen at the corner radii at the tip of the ribs, as white regions were visible. Figure 65 highlights these white regions, most noticeable at the tips of the ribs, for the part processed at 30 bar fill pressure and 400°C. While each of the ribs in Figure 65 show resin rich regions, only one section is enlarged for clarity. Again, since fill pressure was below critical pressure, rough, matrix-torn surfaces are visually apparent on the part.

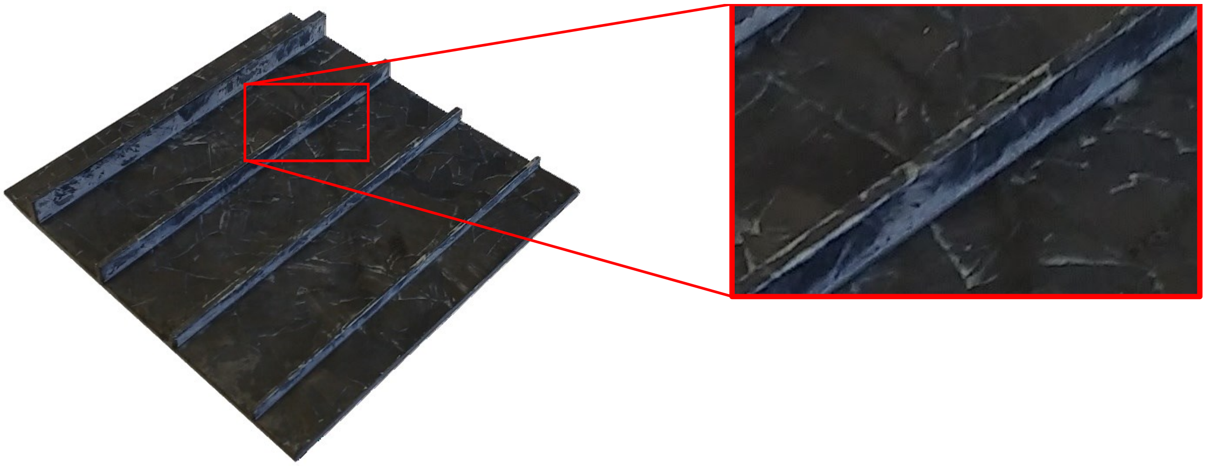

Figure 65: Resin rich rib tips seen in part made with square strands at 30 bar fill pressure and 400°C.

Per injection moulding standards, ribs should be roughly 50% as thick as the shell to avoid sink marks. (I.e. if the shell is 1.8 mm thick, the ribs should only be 0.9 mm thick.) Despite three of the ribs being as thick as the 1.8 mm thick shell or thicker, no sink marks formed opposing the ribs. Only faint lines could be seen on the backs of the panels, as pictured in Figure 66. So, DLF material behaves differently than short fibre composites – it does not suffer from the same defects.

Figure 66: Faint lines visible on the back of the part made with square strands at 30 bar fill pressure and 400°C.

Following the initial visual assessment, parts were cut in three places to assess the filling of the ribs. Cuts were taken approximately 6 mm from each edge, and at the centre of the part, as pictured in Figure 67. Specimen were cast in ClearCast 7000 epoxy resin and polished on a Forcipol variable speed grinder/polisher using a Forcimat automatic head. The images shown below, highlighting processing defects, were taken from specimen at the cut labelled A. Images were captured at 20x magnification on an upright Nikon Eclipse L150 optical microscope using a Märhäuser motorized stage and StageManager 1.0 software.

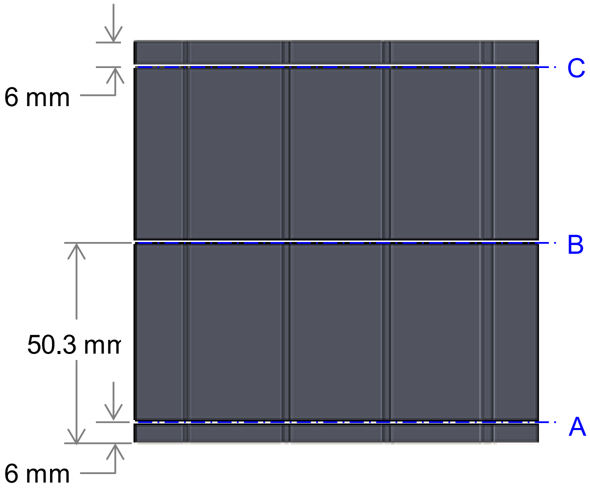

Figure 67: Locations of cuts taken for microscopy samples.

From the microscopy images, the ribs were observed to have filled completely with strands taking on random orientation. Some resin rich regions were present, particularly at the corner radii leading into the ribs and the tips of the ribs, as emphasized in Figure 68, using the Rib B moulded with square strands as an example.

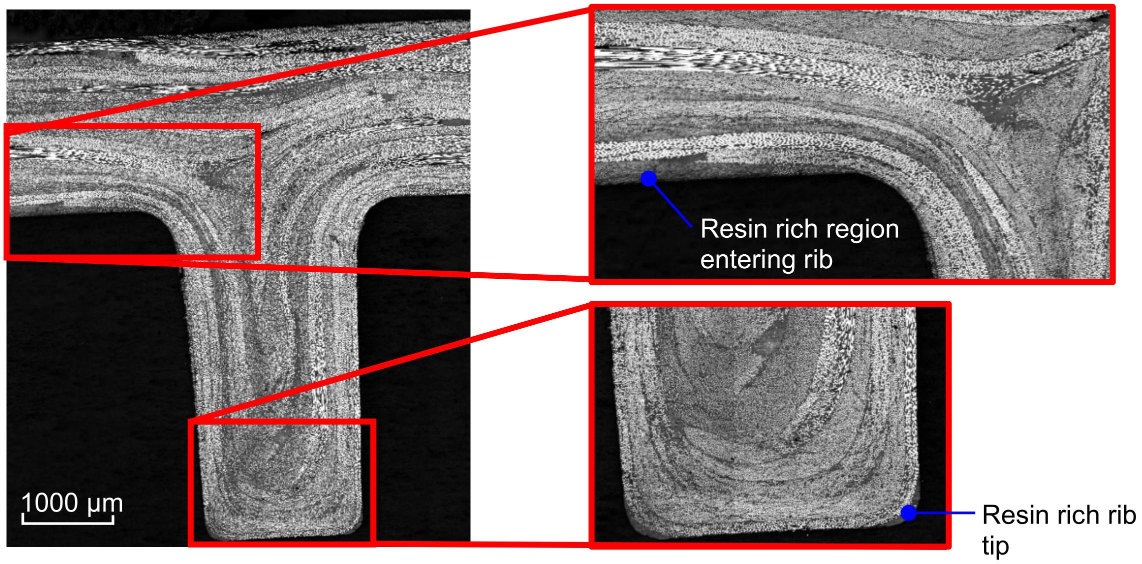

Figure 68: Microscopy image of Rib B moulded at 400°C (at temperature controller) with square strands. Image taken 6 mm from bottom edge of part, highlighting resin-rich regions at entrance to rib and rib tip.

Some swirling and resin rich pockets were also observed at the entrance of the ribs, as seen in Figure 69. Similar to what was seen by LeBlanc in [68], voids appeared more prevalent in the parts moulded at higher temperature, such as the one shown in Figure 69. LeBlanc's justification for this increase in void content was that the mould cavity for the ribs is a fixed volume, filled when the material is molten. So, when filled at higher temperatures, the material is in a greater stage of expansion, has lower density since it has not begun to crystallize, and ultimately less material is needed to fill the cavity. The change in material volume during cooling is greater. So, the parts moulded at higher temperatures create more areas devoid of material – more voids – as they cool.

Due to the low moulding pressure, many surface voids are present on the microscopy images, as highlighted in Figure 70. In addition to the surface voids, there is also visible tearing of the surface matrix, also highlighted in Figure 70. These surface tears create the rough, white part surfaces. To eliminate these defects, moulding pressure must be increased and an alternate cooling strategy must be used, as discussed in Section 3.2.2.1.

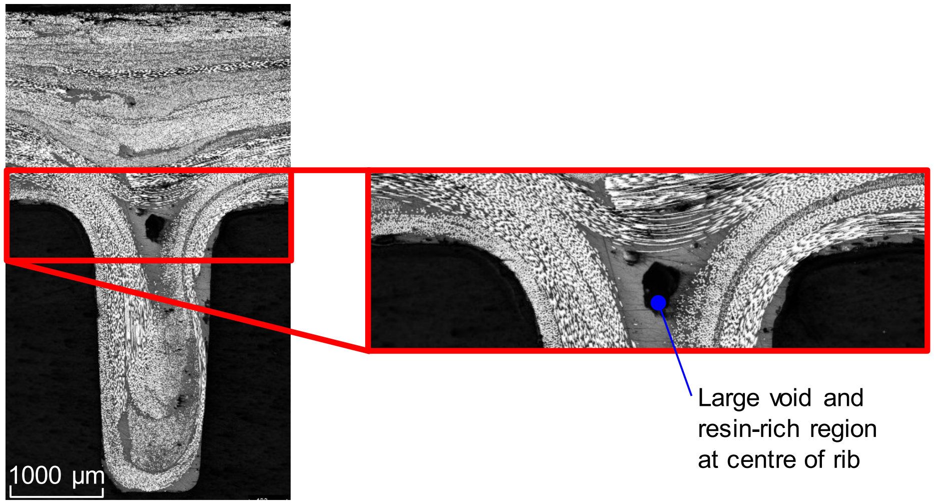

Figure 69: Microscopy image of Rib A moulded at 420°C (at temperature controller) with square strands. Image taken 6 mm from bottom edge of part, highlighting void and resin-rich region at entrance to rib.

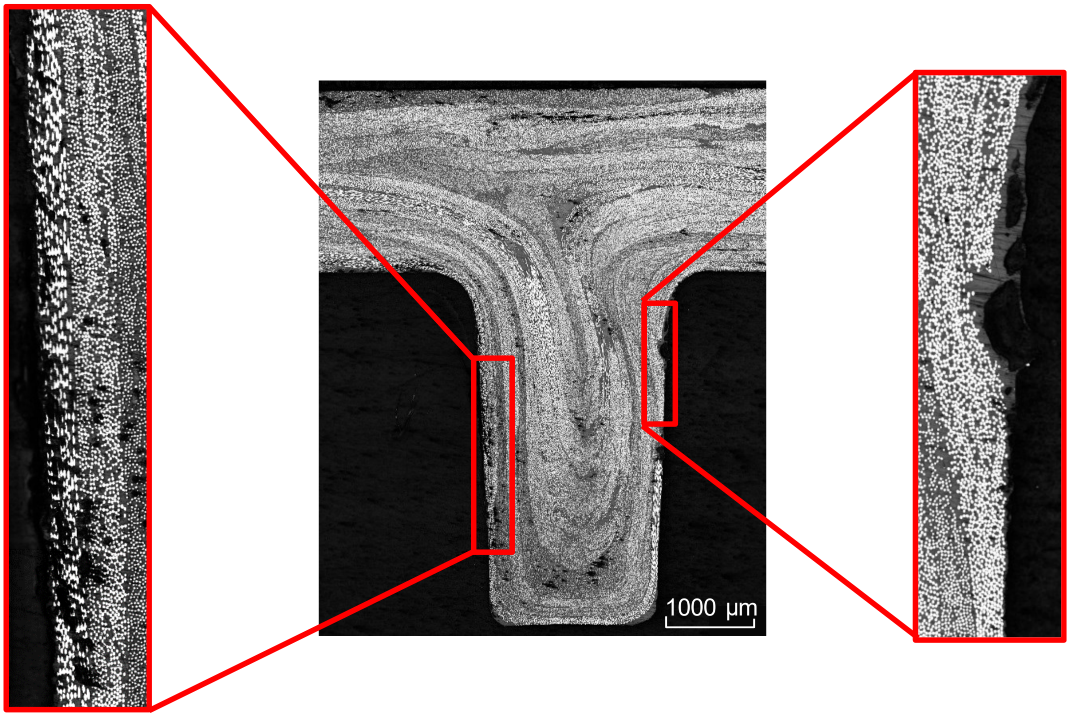

Figure 70: Microscopy image of 1.8 mm x 3.8 mm rib moulded at 420°C (at temperature controller) with square strands. Image taken 6 mm from bottom edge of part, highlighting surface porosity and matrix tearing.

3.2.2 **Part Quality Assessment**

In [17], Landy and Hubert indicate that the matrix-torn surfaces of DLF carbon/PEEK parts processed at insufficient pressure is indicative of higher internal part porosity, as well as the visible surface porosity. Porosity leads to reduced mechanical properties within the part. So, the parts manufactured in Section 3.2.1 at fill pressure, would likely be weaker than parts manufactured with appropriate processing conditions.

In this section, ideal processing conditions will be determined by varying both the applied pressure and the cooling strategy acting on the part. The parts will be checked for visual appearance, both by the naked eye and under the microscope, and consistency in thickness. As well, warpage between parts that were cooled under uniform conditions and cooled following the implementation of a new cooling cycle will be compared to determine if the cooling strategy required for making ribbed parts has a significant impact on overall plate warpage.

3.2.2.1 Procedure and Processing Cycle

Using the same material, mould, and test setup from Section 3.2.1, the moulding pressure and cooling strategy used to create ribbed parts was manipulated to minimize surface defects in the moulded parts. As a baseline, a moulding pressure of 70 bar with uniform cooling was used, since 70 bar was determined in [68] and [63] to produce defect-free surfaces on flat plates and parts made with 3.3 mm x 25.4 mm ribs, moulded in the instrumented hot press. As well, as discussed in [63], complex features, like ribs, need specialized cooling strategies to ensure appropriate compaction pressure during crystallization. The flange of the part should be kept near molten, with a low modulus, while the ribs crystallize, to maintain compaction pressure in the ribs. If the flange solidifies and stiffens before the ribs, the ribs lose pressure and tear away from the mould walls as they cool, leaving a rough, matrix-torn surface. So, the ribs need to be cooled before the flange of the part. Cooling strategy and applied pressure were varied to determine the best moulding conditions to make a part free of surface defects. Mimicking what was done in Section 3.2.1, sufficient material to mould parts with 1.8 mm thick flanges was used.

Using 70 bar pressure and uniform cooling, parts sustained matrix tearing on all surfaces. The back surfaces are shown in Figure 71 (a) and (b). 80 bar was sufficient pressure to achieve smooth back-side surfaces when parts were uniformly cooled, as shown in Figure 71 (c), but the ribbed surfaces still sustained extensive surface tearing.

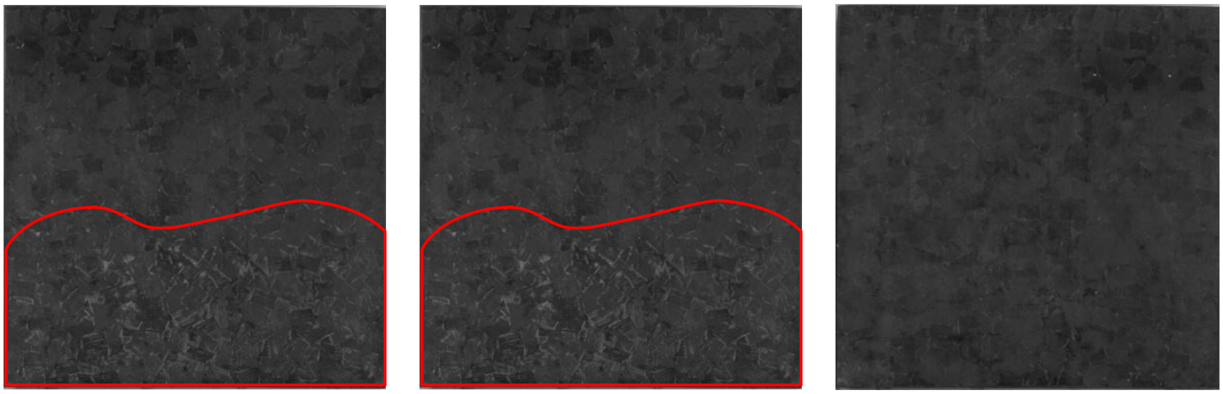

(a) (b) (c)

Figure 71: Back surface of parts made at with uniform cooling using (a) square strands at 70 bar pressure, (b) short strands at 70 bar pressure, and (c) short strands at 80 bar pressure. Regions of matrix tearing are circled in red.

When a cooling strategy, allowing the ribs to be cooled first, was implemented along with 80 bar of pressure, there was a noticeable improvement in the rib surfaces, but all surfaces – including the flat, backside of the part – sustained surface tearing. The best combination of pressure and cooling strategy found is captured in Figure 72, where 110 bar moulding pressure is used and the ribs are cooled fully, with the thermocouple dropping below 200°C before cooling is initiated on the flat side of the part.

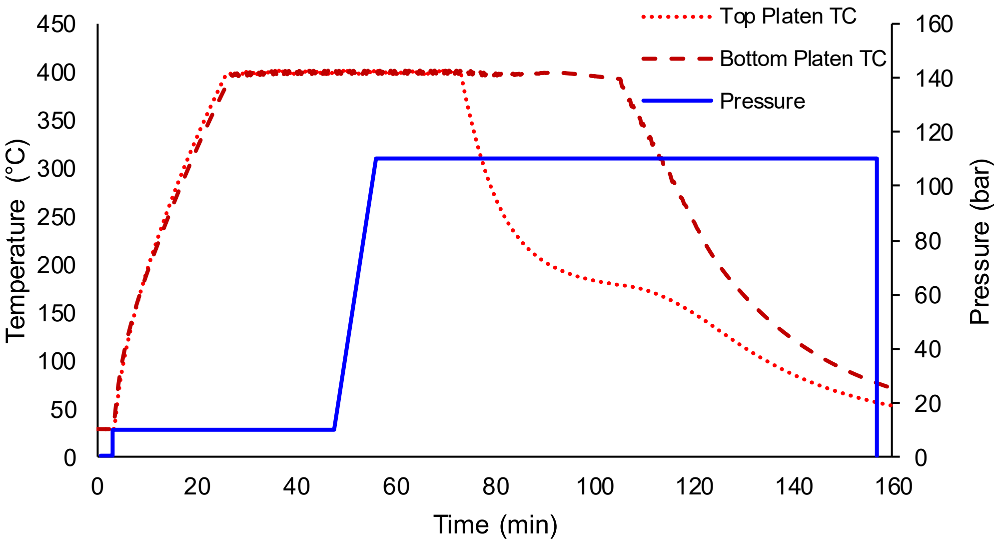

Figure 72: Process cycle used to yield good surface quality in ribbed parts.

3.2.2.2 Visual Assessment

When processed using the cycle shown in Figure 72, the back surfaces of all parts were smooth, and the ribbed surfaces were predominantly smooth as well. With 110 bar of pressure, surface tearing on the ribs was localized on the ends of rib C and rib D, closest to the outlet of the cooling channels, as seen in Figure 73. Matrix tearing was also seen along one full side of the largest (2.5 mm x 7.6 mm) rib, as seen in Figure 74. This indicates that the draft angle used in these ribs (3°) was insufficient to maintain pressure on Rib D throughout cooling. Both parts made at 110 bar – one with short strands and one with square strands – sustained similar matrix tearing.

Figure 73: Ribbed surfaces of parts made with short strands under 110 bar with rib-side cooled below 200°C at the thermocouple before flat-side cooling was initiated, highlighting matrix tearing on cooling outlet end of Rib C and Rib D.

Figure 74: Ribbed surfaces of parts made with short strands under 110 bar with rib-side cooled below 200°C at the thermocouple before flat-side cooling was initiated, highlighting matrix tearing on full side of Rib D.

Even with this high-pressure filling, parts made with the square strands had visible resin-rich regions leading into the ribs and at the tips of the ribs, as shown in Figure 75. These resin rich areas appeared as white areas at the tips of the ribs and at the entrance to the ribs.

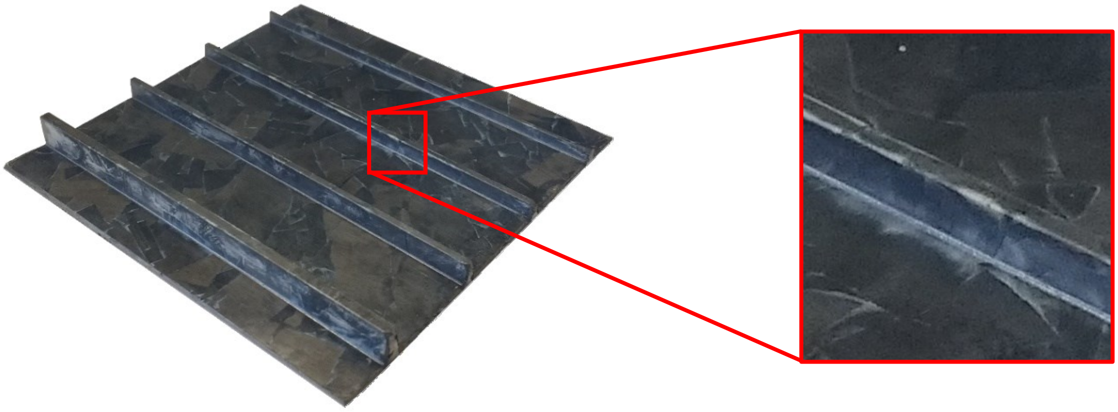

Figure 75: Appearance of resin rich regions at rib entrance and rib tip in part made with square strands and moulded at 110 bar with cooling strategy.

For visual comparison, specimen were cut from parts made under 70 bar moulding pressure with uniform cooling and parts made under 110 bar moulding pressure with rib-side cooling. These samples were cut and polished following the same procedure used in Section 3.2.1.5. Images were captured at 20x magnification on an upright Nikon Eclipse L150 optical microscope using a Märhäuser motorized stage and StageManager 1.0 software. The visible sections were taken from the centre plane of the part.

Looking at Rib C moulded with square strands under both processing conditions, it appears that the processing pressure and cooling strategy only help with final part surface finish, as Figure 76(a) shows matrix tearing and Figure 76(b) does not. Both ribs have large resin rich pockets, with larger pockets seen in the rib moulded at 110 bar in this example. The rib processed under 70 bar pressure also appears to have larger voids, but this is not definitive from the small sample size.

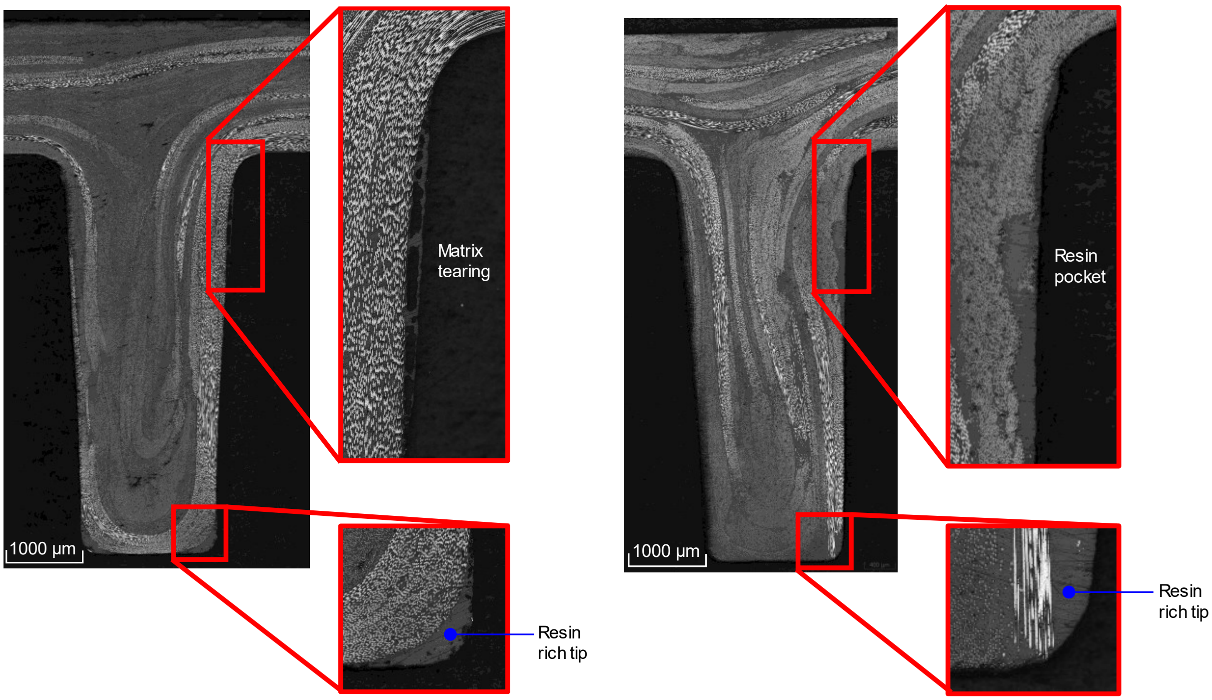

(a) (b)

Figure 76: Microscopy images of Rib C moulded at 400°C (at temperature controller) with square strands using (a) 70 bar moulding pressure and uniform cooling and (b) 110 bar moulding pressure and rib-side cooling. Images taken 50.8 mm from bottom edge of part.

Regardless of processing condition, the ribs show strand swirling and resin rich pockets. However, they do successfully fill completely. The impact of ribs on final part warpage will be assessed in Section 3.3.

3.2.2.3 Thickness Assessment

All parts made under 70 bar of pressure and uniform cooling, as well as under 110 bar of pressure with the prescribed cooling strategy were measured at 12.7 mm increments, using an external micrometer from Mitutoyo (Part Number 118-107 with a 0-1" span). Each part was measured three times and the average measurement attained at each increment was used to create contour maps of part thickness, to visualize variations in thickness within each part. All parts were made with a target thickness of 1.8 mm. In each panel, the thinnest sections were along the cooling inlet side of the part and the thickest sections were closest to the cooling outlet. Figure 77 shows the thickness distributions in parts made with short strands, which ranged from 1.14 mm to 1.98 mm thick in the part made at 70 bar and from 1.15 mm to 2.07 mm thick in the part made at 110 bar. This observed thickness distribution was representative of all measured parts. The images in Figure

77 are oriented as if the ribs are coming out of the page, with the smallest rib on the left side of each part and the largest rib on the right side of each part, as indicated by the dotted white lines.

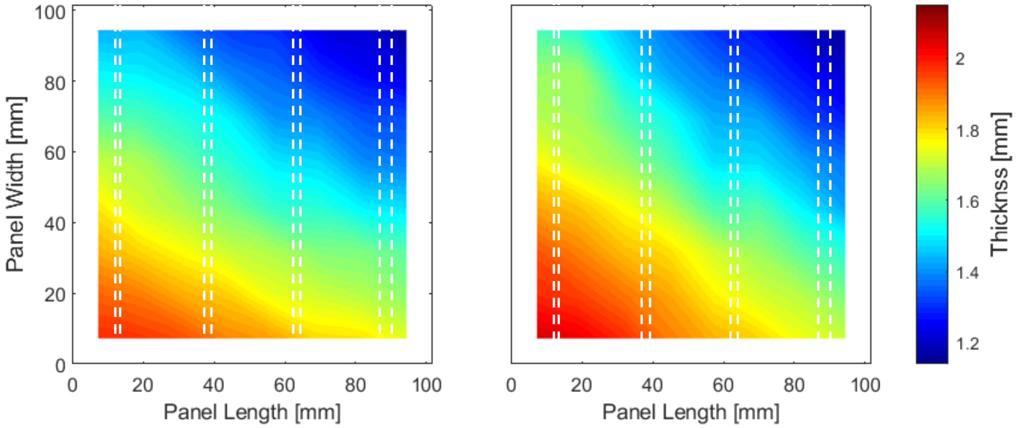

Figure 77: Thickness distribution in parts made with short strands at (a) 70 bar moulding pressure with uniform cooling and (b) 110 bar moulding pressure with cooling strategy.

The total deviations in thickness (difference between maximum and minimum thickness) were significant and varied based on moulding pressure, as shown in Figure 78. The parts made at 110 bar moulding pressure had up to 0.97 mm deviation in thickness for a part with a target thickness of 1.8 mm.

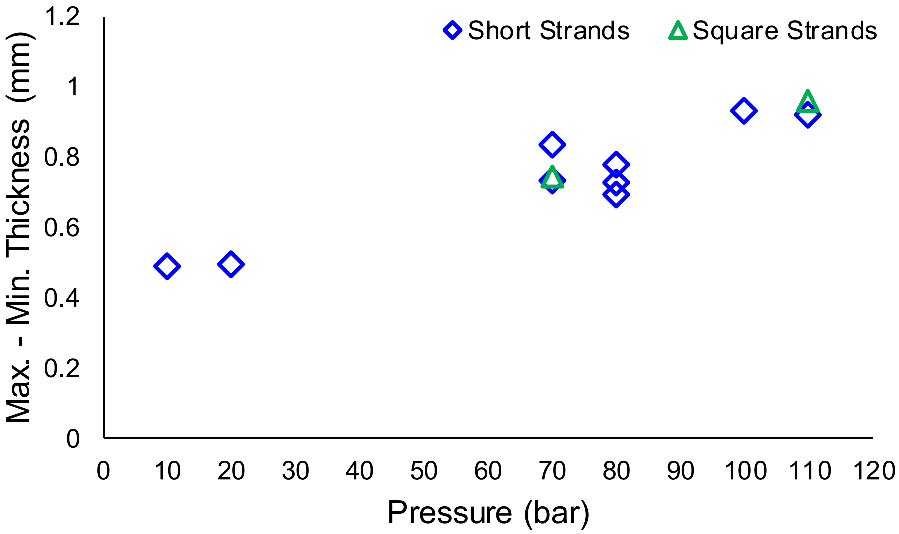

Figure 78: Thickness deviations in moulded ribbed parts as a function of moulding pressure.

This variation in thickness is believed to come from two sources. First, adding the additional inserts to the press appears to have introduced misalignment between platens. The inserts themselves have been verified to be flat. The additional height appears to be the source of error. This has been confirmed by taking imprints of the pressure applied by the press on pressure sensitive films (Fujifilm Prescale, Medium Pressure, Monosheet type). Regardless of insert orientation, a pressure gradient appeared with highest pressure at the corner corresponding with the thinnest part sections and the lowest pressure at the corner corresponding with the thickest part section. Analysis of these pressure films is detailed in Appendix B. This pressure gradient is not apparent when the inserts are not present.

Additionally, the variation in rib thickness is believed to have exacerbated the thickness gradient in the part. Material was distributed evenly within the mould, but more material was displaced to fill the larger ribs. So, it is unsurprising that the part thinned nearest the largest rib. To reduce thickness gradients within parts, it may be beneficial to skew the material distribution towards larger features, with slightly more material at the largest rib and the least material near the smallest rib.

3.2.2.4 Warpage Assessment

Parts made at 70 bar and uniform cooling as well as parts made at 110 bar with the most extreme cooling strategy were scanned using a FARO® ScanArm to assess their warpage. This was done to determine if the cooling strategy had a significant impact on the part's warpage. The process followed the same methodology seen in Section 2.1.2.1.

To determine the warpage in the back of the plate, the distance between the scanned and theoretical part was measured in the z-axis. Measurements were taken every 2 mm. This data was used to create the following contour images, presented as if the ribs are coming out of the page. The smallest rib is on the left and the largest rib is on the right, as indicated by the dotted white lines.

Comparing the parts made with 70 bar moulding pressure and uniform cooling to parts made with 110 bar moulding pressure and the prescribed cooling strategy from Figure 72, the warpage patterns seen are similar. As an example, parts made under these conditions with short strands are shown in Figure 79. In the 70 bar, uniformly cooled panel (left), the part sees 1.37 mm of warpage. This warpage is predominantly curling, parallel to the ribs, as the part is lowest in the centre, between Ribs B and C, and curls up at its edges, parallel to the ribs. Its highest point is located where the part is thinnest. Similarly, the second panel (right) made at 110 bar pressure with rib-side cooling sees 1.52 mm of warpage dominated by curling, parallel to the ribs. The cooling strategy does not appear to have affected the warpage pattern.

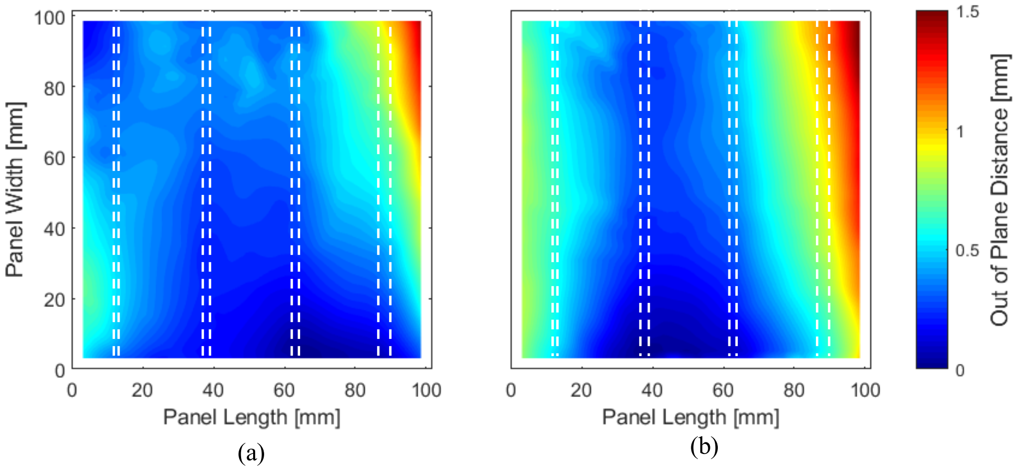

(a)

(b)

Figure 79: Warpage parts made with short strands at (a) 70 bar pressure and uniform cooling and (b) 110 bar pressure with prescribed cooling strategy.

Similarly, the warpage pattern appeared unaffected in parts made with square strands. This was sufficient verification to proceed to moulding parts with evenly-spaced, perpendicular ribs under the prescribed processing conditions. Since cooling strategy appeared to have negligible impact on part warpage, the perpendicularly ribbed parts processed with a rib-side first cooling strategy will be compared directly to the flat panels moulded in Section 2.1 under uniform cooling conditions.

3.3 Ribbed Panel Warpage Mitigation Assessment

With the successful filling and developed processing conditions found in Sections 3.2.1 and 3.2.2, investigation into the use of ribs for warpage mitigation moved forward. In this section, the selected processing conditions from Section 3.2.2 were used to create a part with evenly spaced ribs running orthogonal to each other. The objective was to determine if the addition of ribs reduced overall part warpage. First, the quality of the produced parts was assessed visually to affirm processing conditions. Then the part thickness was measured, to address alignment issues within the instrumented hot press. Finally, the part warpage will be observed, focussing first on the part as a whole, then on the part sections fully surrounded by ribs.

3.3.1.1 Mould Geometry

From the results of the flow study, the 1.0 mm x 3.0 mm ribs were shown to fill successfully. As these ribs were found to have potential for both reducing mass and increasing moment of inertia compared to 2.3 mm thick flat plates, a mould design using 1.0 mm x 3.0 mm ribs was explored.

Ribs were made 50.8 mm apart in both directions, as pictured in Figure 80. The mould was created at an offset such that future work could explore using ribs that are 25.4 mm apart.

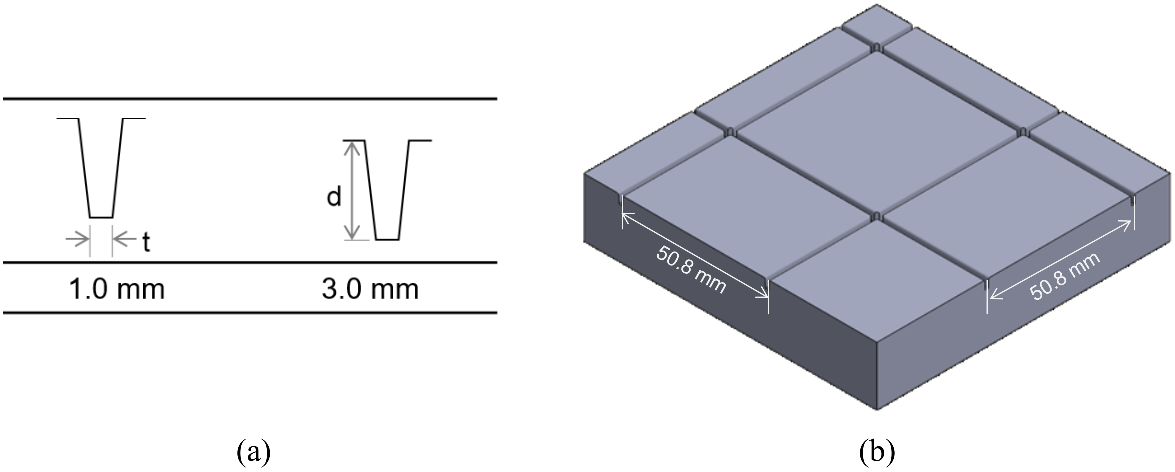

Figure 80: Ribs tested for warpage mitigation showing (a) dimensions and (b) placement within mould.

3.3.1.2 Procedure and Processing Conditions

The process cycle shown in Figure 72 and determined to yield the best surface finish for ribbed parts made on the instrumented hot press with inserts was used. Similar to the procedure followed in Sections 3.2.1 and 3.2.2, the ribs were moulded against gravity as pictured in Figure 81.

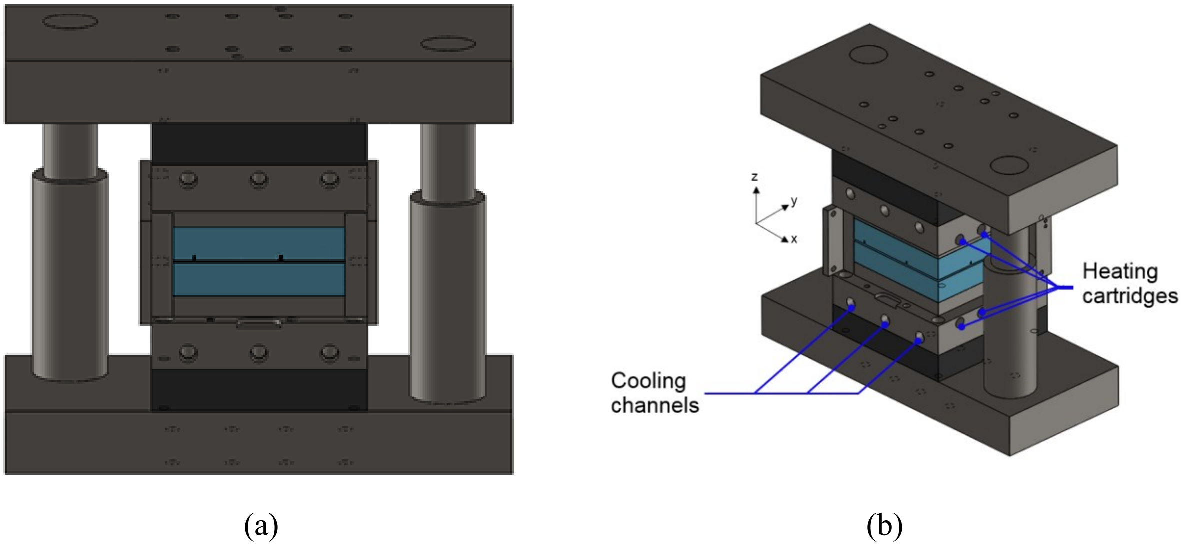

Figure 81: Rib moulding setup showing (a) front view and (b) isometric view.

The following test matrix was followed, selecting flange thicknesses to match previously moulded plate thicknesses from Section 2.1.

Table 6: Ribbed panel test matrix.

Strand Size	Quantity Moulded at Flange Thickness		
	1.5 mm	2.0 mm	2.3 mm
6.35 mm x 3.18 mm	2	2	-
12.70 mm x 12.70 mm	-	-	2

3.3.1.3 *Visual Assessment*

Ribs on all parts visually filled, with sharp radii at the entrance of the ribs. Small resin-rich regions are evident at the corner radii at the tip of the ribs, particularly in the parts made with the square strands. These resin-rich regions appeared as white areas at the tips of the ribs and at the entrance to the ribs, as shown in Figure 82.

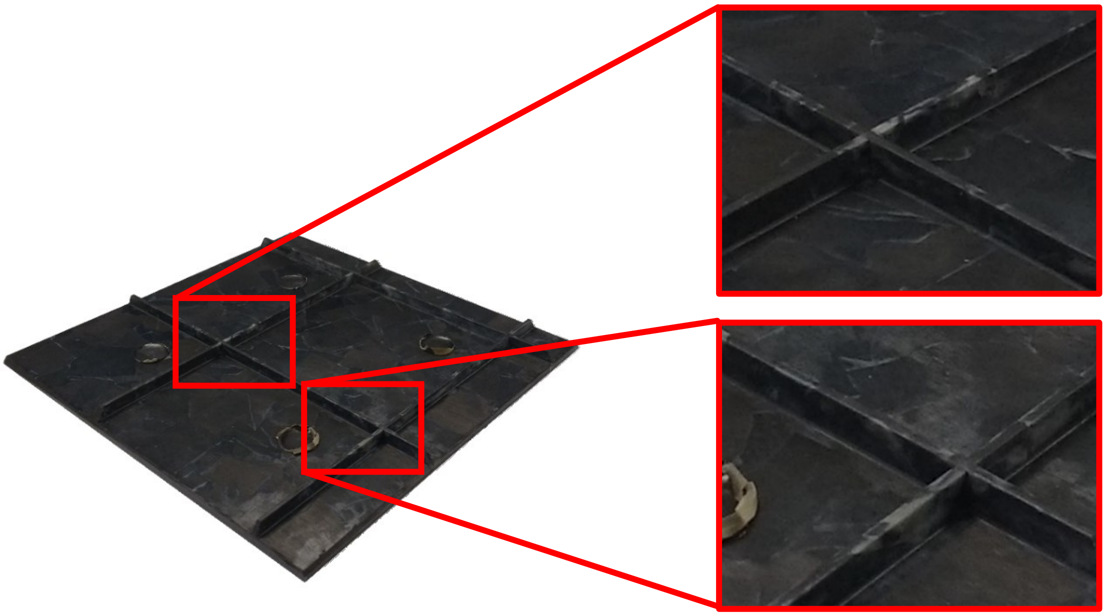

Figure 82: Appearance of resin rich regions at rib tips of 2.3 mm thick part made with square strands.

The back surfaces of all parts were black and smooth. Rib surfaces were smooth as well, indicating that the cooling strategy had the intended effect. Figure 83 shows the rib-side of one of the 1.5 mm thick parts made with short strands.

Figure 83: Parts made with short strands to be 1.5 mm thick.

3.3.1.4 Thickness Assessment

As done in Section 3.2.2.3, all parts were measured at 12.7 mm increments using an external micrometer from Mitutoyo. The same thickness gradient was seen in all parts, as shown in Figure 84 using the 1.5 mm thick panels made with short strands as an example. All parts were thinnest near the cooling channel inlet, and thickest near the cooling channel outlet. However, the total deviation in thickness was reduced, as emphasized in Figure 85, where thickness deviations for the perpendicularly ribbed parts are compared to the vertically ribbed parts moulded at 110 bar pressure from Section 3.2 and the flat plates from Section 2.1.

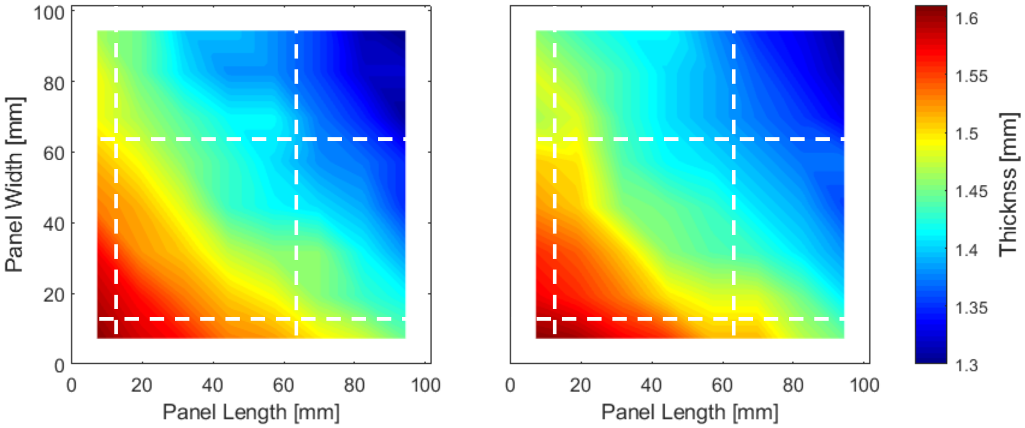

Figure 84: Thickness distribution in parts made with short strands to be 1.5 mm thick.

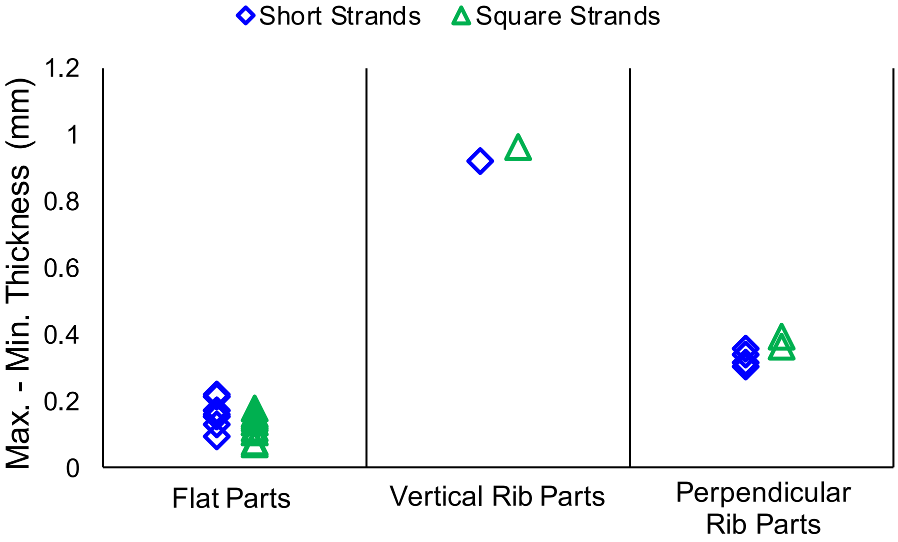

Figure 85: Thickness deviations in parts moulded at recommended processing pressures, comparing flat, vertically ribbed, and perpendicularly ribbed parts.

This thickness distribution further indicates a misalignment within the press when using these mould inserts. The reduction of overall deviation in thickness for the perpendicularly ribbed parts is likely due to the reduced rib volume.

3.3.1.5 Overall Part Warpage Assessment

The back surfaces of all parts were scanned and assessed for warpage. The 2.3 mm parts made with square strands sustained 0.49 mm and 0.35 mm of warpage on the part as a whole. The parts made with short strands sustained 0.43 mm and 0.52 mm of warpage, when made 2.0 mm thick, and sustained 0.57 mm and 0.97 mm of warpage when made 1.5 mm thick. A graph comparing the magnitude of part warpage in 101.6 mm x 101.6 mm flat and ribbed panels is displayed in Figure 86.

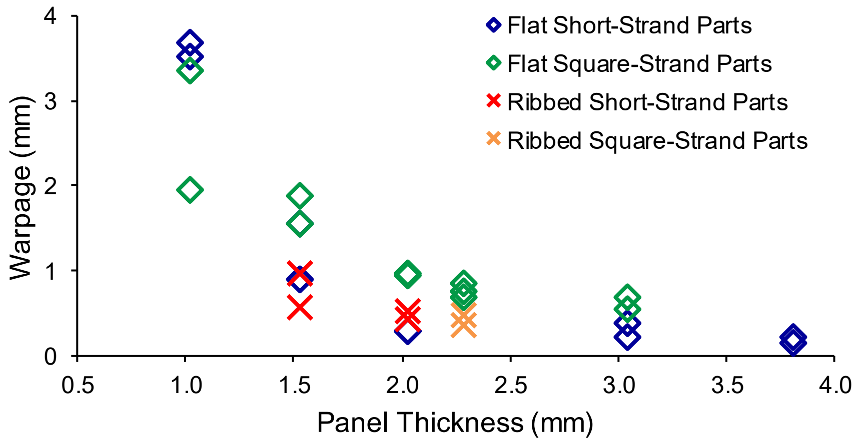

Figure 86: Warpage comparison of ribbed and flat 101.6 mm x 101.6 mm parts

Looking at Figure 86, the addition of ribs does not have a visibly positive effect on part warpage. The panels made with short strands did not show an improvement in overall magnitude of warpage when compared to flat plates. The magnitude of warpage in the 1.5 mm thick ribbed parts was reduced, but the variation in warpage was still significant. The magnitude of warpage in the 2.0 mm thick ribbed parts was larger than that seen in the 2.0 mm thick flat plates. Minimal reduction in magnitude of warpage was seen when adding ribbing to the 2.3 mm thick plates made of square strands. As well, the parts made with square strands appear to have warped magnitudes closer to those seen in parts produced with short strands, indicating that the part ribbing may be influencing warpage more than strand size. However, to best consider the addition of ribs, the section of the part that is fully supported by ribs must be considered. This section is isolated from the rest of the part and results are discussed in Section 3.3.1.6.

The more positive effect on the overall parts was in part shape. Unlike the flat plates shown in Section 2.1, where the largest deflections were seen at different points along the part edge, the maximum warpage in all ribbed panels was seen near the centre of the fully supported section. Figure 87 acts as an example of this trend, showing the parts with the ribs represented as dashed white lines, oriented such that they would be coming out of the page.

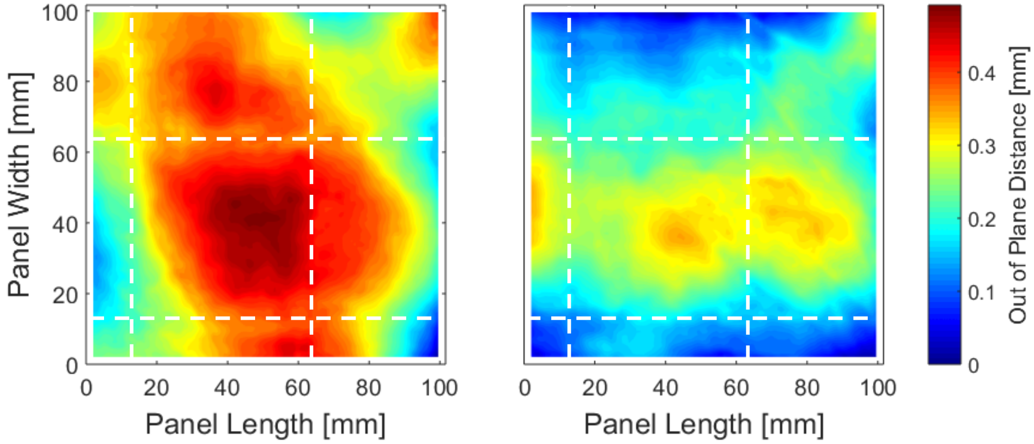

Figure 87: Warpage in parts made with square strands to be 2.3 mm thick

This relatively consistent shape appears to come predominantly from the addition of the ribs, particularly since local maxima appear within the sections supported on at least three sides by ribs. Adding ribs changes the dynamic during part cooling, restricting the in-plane shrinkage of the ribbed surface more than the flat surface. The flat surface experienced more shrinkage, causing the part to bow inwards, between ribbed sections.

Additionally, the parts are cooled on their top (ribbed) side first and the effective warped shape indicates that the part is curling towards the hotter bottom side of the tool. However, based on the comparison between vertically ribbed parts under uniform cooling and under rib-side cooling from Section 3.2.2.4, the cooling strategy is expected to have limited impact on the final warped shape.

3.3.1.6 Fully Supported Part Warpage Assessment

To consider only the fully supported section of each part, the point cloud data for this 50.8 mm x 50.8 mm area on each panel was isolated from the full panel scans. The data was then best fit with a plane in MATLAB to re-assess the total warpage of the section, as illustrated in Figure 88, using the first 2.3 mm thick ribbed part made with square strands as an example.

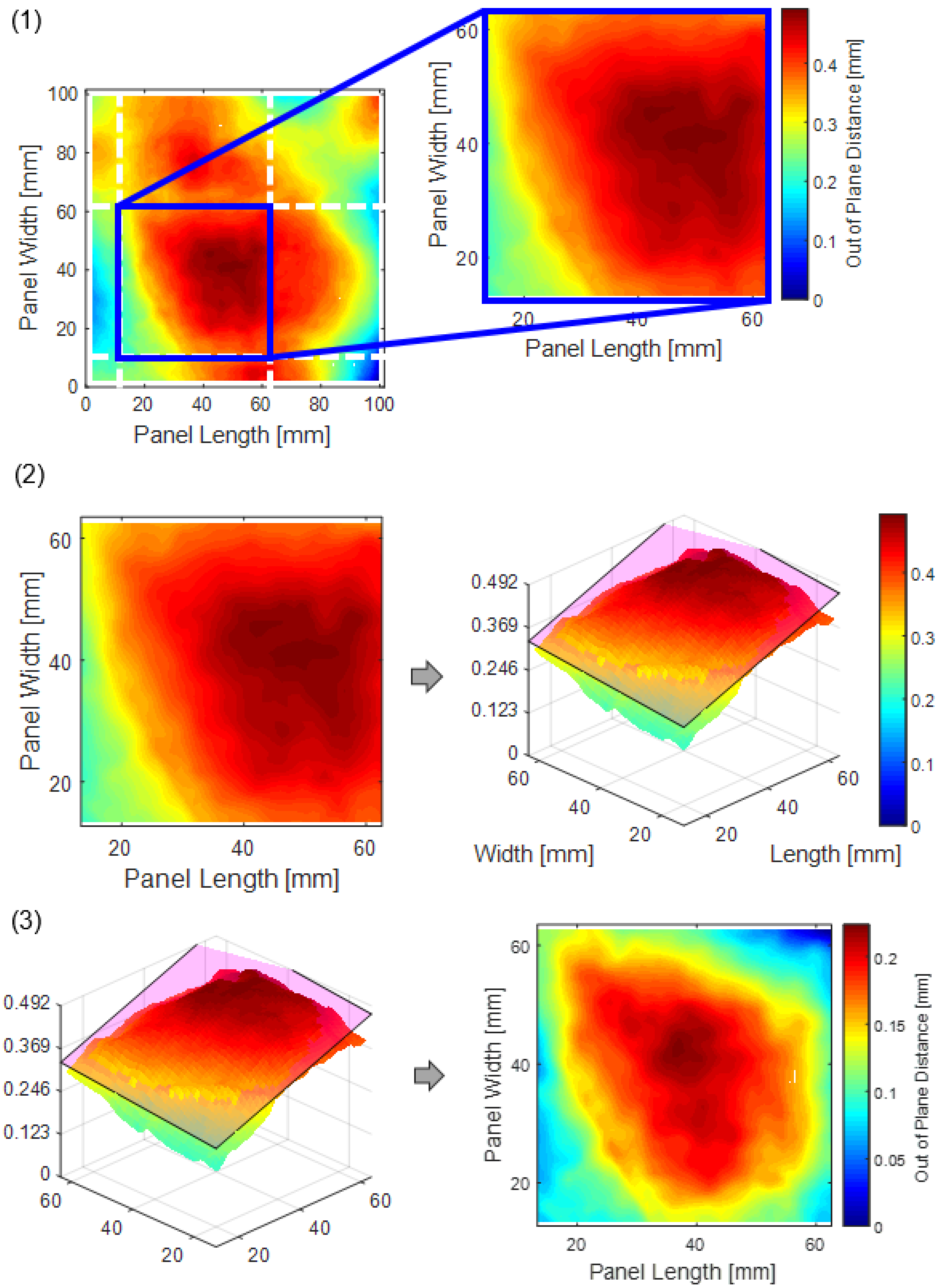

Figure 88: Steps to assess warpage of 50.8 mm x 50.8 mm section – (1) Isolate section; (2) Fit plane to section; (3) Determine warpage from distance from plane.

Looking at the 2.3 mm thick ribbed parts made with square strands in Figure 89, there is a clear pattern to the warped shape. Both are highest at their centres and lowest along the edges, indicating that the part is bowing inwards, towards the ribs. This is likely happening because the shell of the part shrinks significantly as it cools, and the ribs are constraining this movement. As well, the magnitude of warpage in both parts is relatively consistent with a value of 0.23 mm in the first part and 0.20 mm in the second.

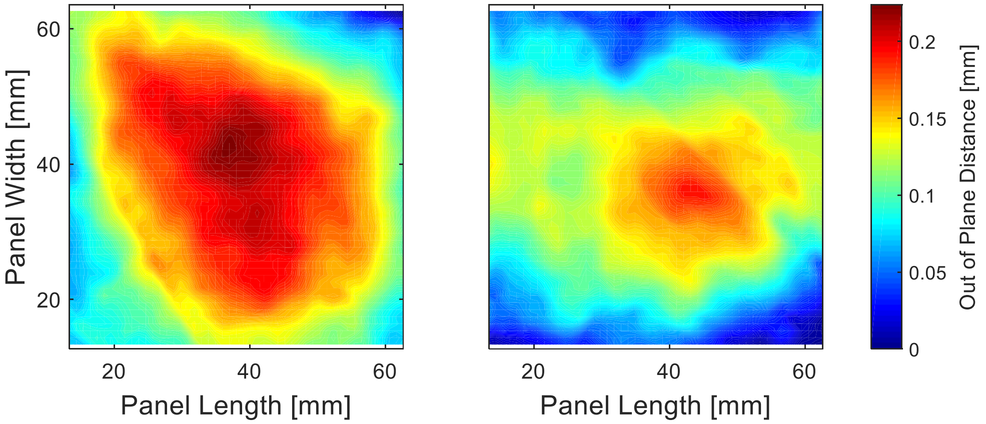

Figure 89: Warpage in supported section of 2.3 mm thick ribbed parts made with square strands.

The 2.0 mm thick and 1.5 mm thick ribbed parts made with short strands produced the same warped shape, creating a dome bowing inwards towards the ribs in each part. As well, the magnitude of warpage in both pairs parts is relatively consistent with a value of 0.15 mm in both 2.0 mm thick parts and a value of 0.25 mm in both 1.5 mm thick parts.

Looking at 50.8 mm x 50.8 mm sections of flat plates at the same part location gives very different results. Figure 90 is one example, showing a comparable section of 2.3 mm thick flat plates made with square strands. In all of the flat plates, the warped shape is different. As well, the value of warpage is very different in each. A comparison of the warpage magnitudes between supported sections of the ribbed plates and corresponding sections of the flat plates is captured in Figure 91.

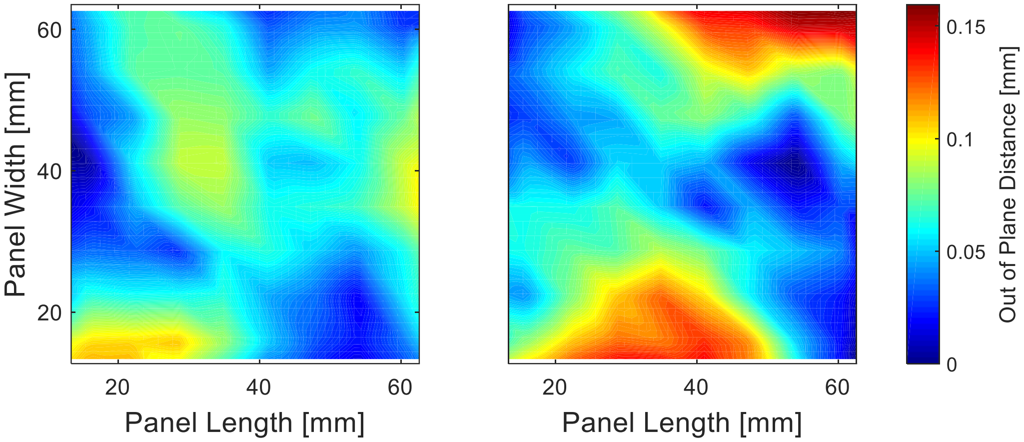

Figure 90: Warpage in the supported section of 2.3 mm thick flat parts made with square strands.

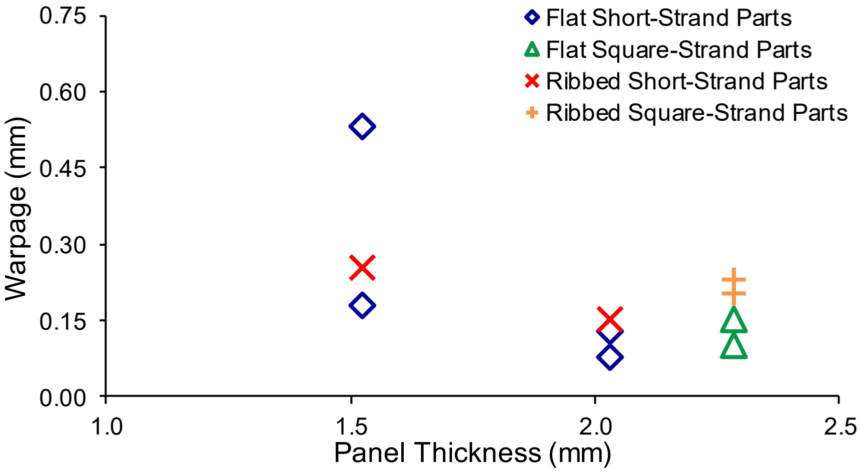

Figure 91: Warpage comparison of 50.8 mm x 50.8 mm supported section of ribbed parts to 50.8 mm x 50.8 mm sections of flat parts at the same part location.

In Figure 92, 50.8 mm x 50.8 mm sections were taken at 12.7 mm intervals across each flat plate. Results show varied patterns of warpage in every section and significant variation in the magnitude of warpage. The 2.3 mm thick plates varied from 0.11 mm – 0.30 mm of warpage, compared to 0.20 mm and 0.23 mm warpage in the ribbed parts. The 2.0 mm thick plates varied from 0.06 mm – 0.14 mm warpage, compared to the 0.15 mm warpage seen in ribbed parts. The first 1.5 mm thick plate varied from 0.44 mm – 0.68 mm of warpage, depending on the section and the second varied from 0.16 mm – 0.27 mm, compared to the 0.25 mm seen in ribbed parts.

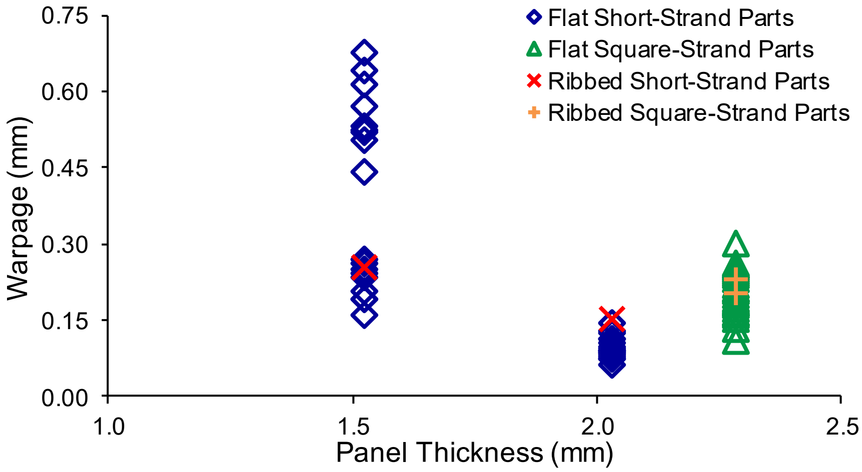

Figure 92: Warpage comparison of 50.8 mm x 50.8 mm supported section of ribbed parts to 50.8 mm x 50.8 mm sections throughout flat plates of equivalent thickness.

From this comparison, it is apparent that the addition of ribs in the DLF part creates a more consistent warped shape and warped magnitude part-to-part. However, the addition of ribs does not necessarily mean that the magnitude of warpage will be reduced. In the case of the 2.0 mm thick parts made with 6.35 mm x 3.18 mm strands, the magnitude of warpage was lower in all 50.8 mm x 50.8 mm sections of the flat plates than it was in the supported sections of the ribbed parts. It should be noted that, as shown previously in Figure 86, the magnitude of warpage in flat parts made with 6.35 mm x 3.18 mm strands is relatively consistent for parts 2.0 mm thick and thicker. So, this strand size and thickness is already relatively stable. Adding ribs does not appear to reduce this warpage, but rather creates a new source of warpage.

3.3.1.7 Warpage Assessment of Partially Supported 50.8 mm x 38.1 mm Sections

In the ribbed parts made, each had two sections 50.8 mm x 38.1 mm, supported by ribs on three sides, as highlighted in Figure 93. Looking only at these sections, a trend in warped shape was seen as well. Similar to the fully supported sections, the highest point on all sections observed was near its centre. An example of this for the 2.3 mm thick ribbed parts is seen in Figure 94 and Figure 95.

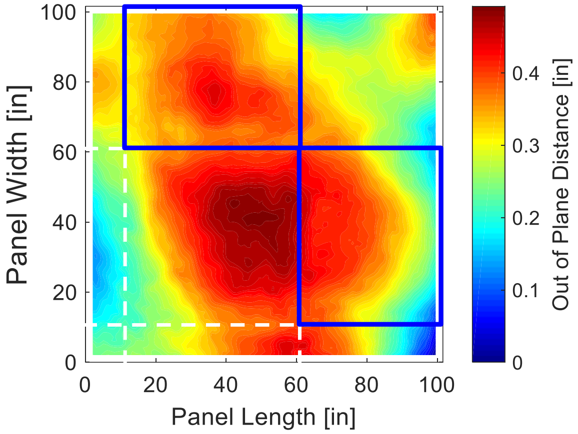

Figure 93: Location of 50.8 mm x 38.1 mm sections, indicated on warped image of first 2.3 mm thick ribbed part made with square strands.

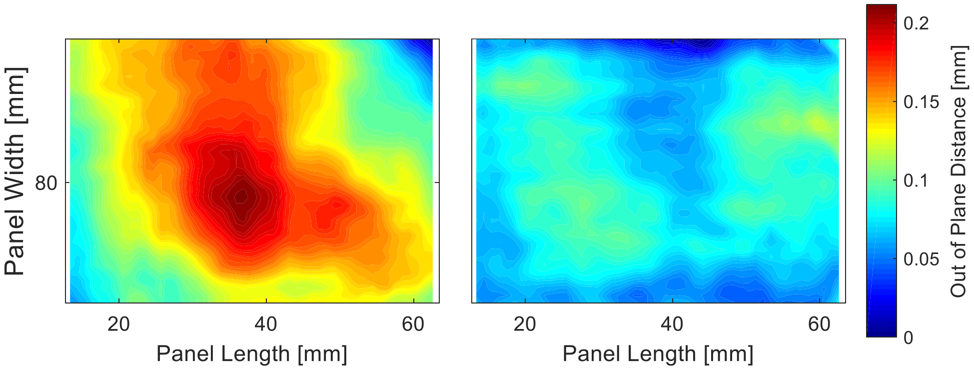

Figure 94: Warpage in 50.8 mm x 38.1 mm partially supported sections of 2.3 mm thick ribbed parts made with square strands.

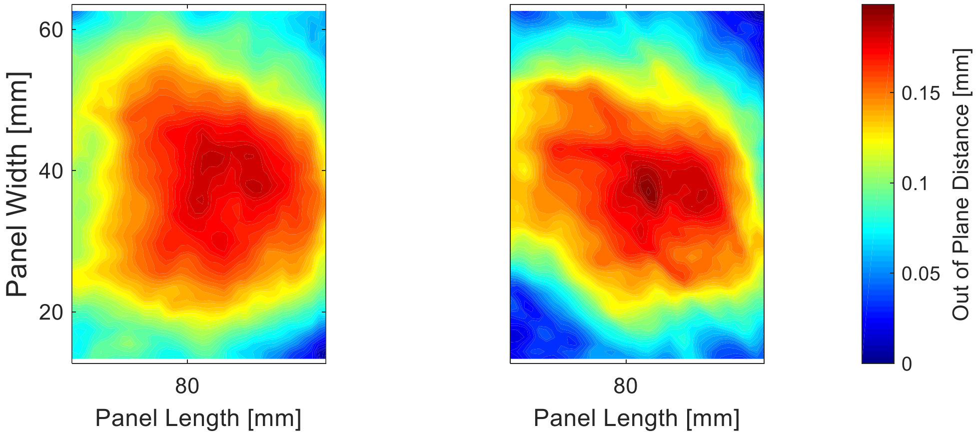

Figure 95: Warpage in 50.8 mm x 38.1 mm partially supported sections of 2.3 mm thick ribbed parts made with square strands.

Unlike the fully supported sections, there was significant variability in magnitude of warpage in these sections for the 1.5 mm thick parts. While the 2.3 mm and 2.0 mm thick parts maintained warpage values between 0.13 mm and 0.20 mm, the 1.5 mm thick part varied from 0.18 mm – 0.33 mm of warpage, indicating that, even with ribs, parts thinner than 2.0 mm may be unstable.

3.3.1.8 Warpage Assessment of Partially Supported 38.1 mm x 38.1 mm Sections

In the ribbed parts made, each had one 38.1 mm x 38.1 mm section, supported by ribs on two sides, as highlighted in Figure 98. Looking only at this section for each part, two distinct warped shapes were observed. Some curled down where the ribs met the free edge of the part, but up at the intersection of the ribs and at unsupported corner. Others did the opposite – curling upwards where the ribs met the free edge of the part, but downwards at the intersection of the ribs and at unsupported corner. In all cases, the warped shape resembled a saddle. An example of this for the 2.3 mm thick ribbed parts is seen in Figure 97. Both 2.3 mm thick parts experienced 0.30 mm of warpage in this section and warped in the same manner. To give an example of the other warped shapes seen, Figure 98 shows the 38.1 mm x 38.1 mm partially supported section in 1.5 mm thick parts.

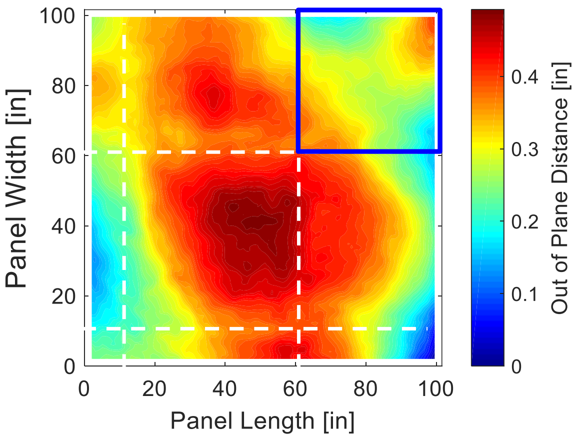

Figure 96: Location of 38.1 mm x 38.1 mm section, indicated on warped image of first 2.3 mm thick ribbed part made with square strands.

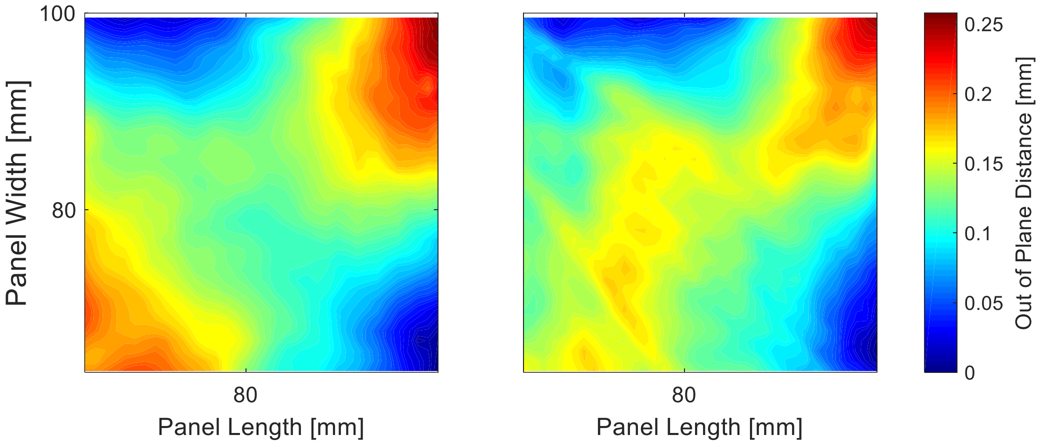

Figure 97: Warpage in 38.1 mm x 38.1 mm partially supported sections of 2.3 mm thick ribbed parts made with square strands.

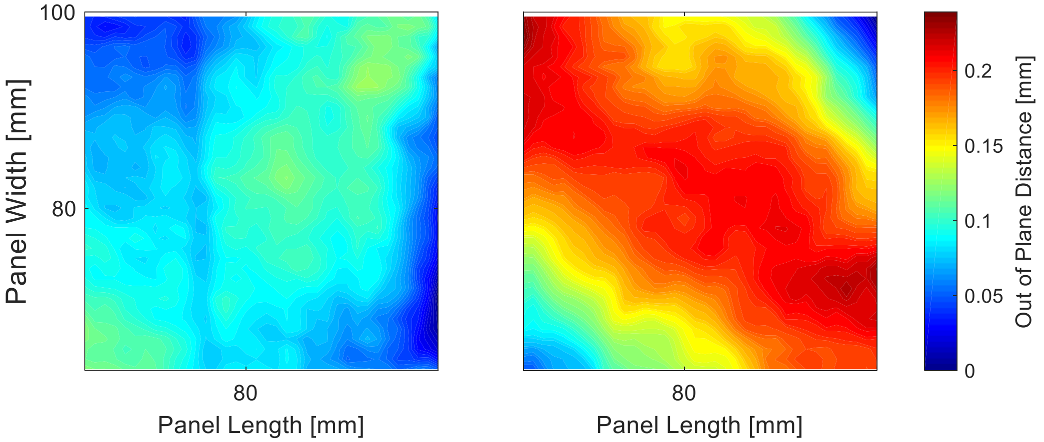

Figure 98: Warpage in 38.1 mm x 38.1 mm partially supported sections of 1.5 mm thick ribbed parts made with short strands.

This 38.1 mm x 38.1 mm section saw significant variability in warped magnitude in all parts, indicating that having two free edges allows for instability in both the magnitude and shape of the final part.

3.4 Summary and Conclusions

From exploring the incorporation of stiffening rib features in thin DLF parts, the following observations were made:

1. At a material temperature of approximately 380°C (controller temperature of 400°C) and pressures as low as 20 and 30 bar, ribs can fill with DLF material of 6.35 mm x 3.18 mm and 12.70 mm x 12.70 mm strand size, respectively. This affirms the findings seen in [68],

showing that the processing maps developed by LeBlanc can be extended to small ribs ranging from 1.0 mm wide x 3.0 mm deep to 2.5 mm wide x 7.6 mm deep.

2. To achieve the best quality surface finish, a combination of high moulding pressure and cooling strategy must be implemented, affirming work done in [68] and [63]. Applying 110 bar of pressure and heating the flat side of the part while the ribs cooled below 200°C provided good surface finishes on the flat sides of the parts as well as on the smallest two ribs (1.0 mm x 3.0 mm and 1.8 mm x 3.8 mm) in this particular moulding configuration. Under these processing conditions, some matrix tearing was still seen on the ribs, with the worst surface finish on the largest ribs (2.5 mm x 7.6 mm), indicating that a larger draft angle (>3°) would be necessary to maintain pressure on these large ribs throughout cooling.
3. From experimental results, adding evenly spaced ribs running in two perpendicular directions did not significantly decrease the magnitude of part warpage, but it appeared to reduce deviation between parts made with different strand sizes, compared to what was seen in flat plates.
4. Within thin sections fully surrounded by ribs, warpage appears to occur in a predictable, dome-like shape, with the centre of the supported section bowing in the direction of the ribs. As well, magnitude of warpage appears consistent within fully supported sections.
5. In partially supported sections – where three sides are surrounded by ribs, the warped shape bears some resemblance to that seen in fully supported sections, but the magnitude of warpage was more varied. In sections where only two sides are supported by ribs, magnitude and shape of warpage is variable, like what is seen in a fully free-edged flat part.

The main findings showed that ribbed features can be successfully implemented in flat parts. While adding ribs can help to control the shape of warpage, the magnitude of warpage is still significant. Residual stress induced from the ribbed geometry appeared to dominate, reducing the deviation in warpage between parts made with short strands and square strands. As well 2.0 mm thick parts made with short strands saw higher overall warpage in ribbed parts compared to flat plates.

4. Conclusions and Future Work

The main objective of this thesis was to advance the knowledge of warpage in DLF composites such that critical part size and thickness can be determined in the design stages for DLF parts with large, thin sections and tight dimensional stability requirements. In addressing this knowledge gap, processing investigations were performed for thin, flat parts as well as for thin parts with small ribbed features. The following conclusions were found:

Flat Plate Investigation

- Magnitude of plate warpage was assessed for 101.6 mm x 101.6 mm flat plates made with two different strand sizes across a range of thicknesses. Plates made <2.0 mm thick suffered from the most significant warpage, with significant variation part-to-part. Plates made with 6.35 mm x 3.18 mm strands warped less than plates made with 12.70 mm x 12.70 mm strands, leveling out with an average of 0.28 mm warpage for short-strand parts 2.0 mm and thicker, but still showing between 0.53 mm – 0.68 mm in 3.0 mm thick parts made with square strands.
- Each plate warped differently, indicating that the random strand distribution has a dominant effect on part warpage. While many of the parts took on saddle-like shapes, the orientation of the saddle was inconsistent. As well, approximately 40% of the parts did not resemble saddles, having several randomly-located local maxima and minima. Due to the inconsistency in part shape, plates of different sizes (101.6 mm x 101.6 mm and 304.8 mm x 355.6 mm) were compared by normalizing each plate’s warpage values against the distance between the absolute maximum and minimum on each plate. Three of the five discussed large plates had similar warpage metrics to the small plates of near-equivalent thickness. The remaining two plates had significantly higher warpage, despite consistent processing conditions.
- A preliminary simulation of processing conditions and warpage in the 101.6 mm x 101.6 mm plates was performed, again verifying that part warpage is dominated by strand distribution, as each simulated plate presented a different warped shape. As well, the simulation mimicked trends seen in experimental parts, showing a reduction in warpage for increasing plate thickness.

Ribbed Part Investigation

- Critical filling pressure and recommended processing conditions were verified for ribs ranging from 1.0 mm wide x 3.0 mm deep to 2.5 mm wide x 7.6 mm deep. For the mould setup used in this thesis, ribbed plates required 110 bar pressure and rib-side only cooling until the rib-side temperature controller dropped below 200°C to create parts with smooth, black surfaces.
- The addition of evenly spaced, orthogonal rib features altered how the parts warped. Residual stress induced from the ribbed geometry appeared to dominate, reducing the deviation in warpage between parts made with short strands and square strands, but actually increasing the overall warpage seen in 2.0 mm thick parts made with short strands. However, the shape of the warpage was consistent, particularly within the regions fully surrounded by ribs; the warpage appeared to take on a domed shape, bowing inwards, towards the ribs.

4.1 Future Work

Due to the time and material limitations in this study, several items remain to be explored. First, it would be interesting to explore the effect of more strand sizes and varied processing conditions on the warpage of flat plates. As well, it would be of interest to mould more large panels at varying thicknesses and with different strand sizes.

To develop a better representative predictive model for part warpage, it would be interesting to explore modelling the fibres as embedded solids within the matrix, to better capture the effects of micro-mechanical stresses.

As well, it would be of interest to explore the effects of annealing on part warpage. Observing continuous fibre composites in [56], warpage was found to reduce when parts were clamped flat and heated to T_g for extended periods of time. A similar approach could be taken for DLF plates.

5. References

[1] B. Cantor, P. Grant, and H. Assender, *Aerospace materials*. Bristol: Institute of Physics, 2001.

[2] J. Hale. (2008, Boeing 787 - From the Ground Up. *AERO Magazine (4.06),* 17-23. Available: http://www.boeing.com/commercial/aeromagazine/articles/qtr_4_06/AERO_Q406_article4.pdf

[3] G. Marsh. (2010, Airbus A350 XWB update. *Reinforced Plastics 54,* 20-24.

[4] Bombardier Inc. (2015, C Series. Available: http://commercialaircraft.bombardier.com/content/dam/Websites/bca/literature/cseries/Bombardier-Commercial-Aircraft-CSeries-Brochure-en.pdf.pdf

[5] Bombardier Inc. (2016, Building Aircraft Innovation with Advanced Materials. Available: http://news.commercialaircraft.bombardier.com/building-aircraft-innovation-with-advanced-materials/

[6] N. Eguémann, L. Giger, M. Roux, C. Dransfeld, F. Thiébaud, and D. Perreux, "Compression Moulding of Complex Parts for the Aerospace with Discontinuous Novel and Recycled Thermoplastic Composite Materials," presented at the The 19th International Conference on Composite Materials, Montreal, Canada, 2013.

[7] A. Miaris, K. Edelmann, and M. von Hayek Boelingen, "A350 WXB: Thousands of thermoplastic composite parts in an FRP aircraft," presented at the SAMPE, Seattle, WA, 2014.

[8] S. Black. (2015, Thermoplastic composites "clip" time, labor on small but crucial parts.

[9] UDASH. (2014). *Aircraft Hinges & Hing Pins*. Available: http://udash.com/wordpress/aircraft-hinge-components/

[10] T. L. Greene, "Discontinuous long fiber composites for complex shape metal replacement," presented at the The Composites and Advanced Materials Expo, Orlando, FL, 2014.

[11] M. van Wijngaarden, A. Jongbloed, and J. de Vries, "Thermoplastic Compound Compression Moulding," in *Proceedings of the SAMPE Conference*, Seattle, WA, USA, 2010.

[12] D. Howell and S. Fukumoto, "COMPRESSION MOLDING OF LONG CHOPPED FIBER THERMOPLASTIC COMPOSITES," 2014.

[13] N. Eguémann, L. Giger, M. Roux, C. Dransfeld, F. Thiébaud, and D. Perreux, "Manufacturing and Recycling of Complex Composite Thermoplastic Parts for Aerospace Application," in *Proceedings from 7th International Technical Conference and Table Top Exhibition*, Lucerne, Switzerland, 2012.

[14] M. Selezneva and L. Lessard, *Characterization of mechanical properties of randomly oriented strand thermoplastic composites* vol. 50, 2015.

[15] D. Howell and J. Gabriel, "Compression Molded Composites: Processes, Benefits and Applications - An Interview With TenCate," G. P. Thomas, Ed., ed: AZoM, 2014.

[16] T. L. Greene, C. Wonderly, H. Kilic, and B. Keller, "Complex-Shape Metallic Aircraft Engine Bracket Replacement using Compression Molded Discontinuous Long Fiber Thermoplastic Composites," presented at the CAMX Conference Proceedings, Dallas, TX, 2015.

[17] B. Landry and P. Hubert, "Experimental study of defect formation during processing of randomly-oriented strand carbon/PEEK composites," *Composites Part A: Applied Science and Manufacturing,* vol. 77, pp. 301-309, 10// 2015.

[18] N. Johnston, T. Towell, and P. Hergenrother, "Physical and mechanical properties of high-performance thermoplastic polymers and their composites," *Elsevier Science Publishers BV, Thermoplastic Composite Materials,* pp. 27-71, 1991.

[19] G. d. C. Vasconcelos, R. L. Mazur, E. C. Botelho, M. C. Rezende, and M. L. Costa, "Evaluation of crystallization kinetics of poly (ether-ketone-ketone) and poly (ether-ether-ketone) by DSC," *Journal of Aerospace Technology and Management,* vol. 2, pp. 155-162, 2010.

[20] A. Levy and P. Hubert, "Interstrand void content evolution in compression moulding of randomly oriented strands (ROS) of thermoplastic composites," *Composites Part a-Applied Science and Manufacturing,* vol. 70, pp. 121-131, Mar 2015.

[21] M. Lesueur, B. Pipes, and L. Adam, "Compression Molding of Discontinuous Fiber Composites, a Thermodynamics Approach to the Compaction Problem," presented at the American Society for Composites - 32nd Technical Conference, West Lafayette, Indiana, 2017.

[22] G.-P. Picher-Martel, A. Levy, and P. Hubert, "Compression moulding of Carbon/PEEK Randomly-Oriented Strands composites: A 2D Finite Element model to predict the squeeze flow behaviour," *Composites Part A: Applied Science and Manufacturing,* vol. 81, pp. 69-77, 2// 2016.

[23] B. R. Denos and B. Pipes, "Local Mean Fiber Orientation via Computer Assisted Tomography Analysis for Long Discontinuous Fiber Composites," presented at the American Society for Composites - 31st Technical Conference, Williamsburg, VA, 2016.

[24] Y. Wan and J. Takahashi, *Meso-structural quantification and visualization of ROS of thermoplastic composites*, 2017.

[25] R. Cole, D. Backman, and B. Barnett, "Strain Measurement Considerations for Discontinuous Carbon Fibre Reinforced Composite Parts," presented at the 10th Canadian-International Composites Conference, Ottawa, ON, 2017.

[26] Y. Nakashima, H. Suganuma, S. Yamashita, and J. Takahashi, *INFLUENCE OF STRAND DISPERSION METHOD ON MECHANICAL PROPERTIES OF RANDOMLY ORIENTED CARBON FIBER STRAND THERMOPLASTIC COMPOSITES*, 2017.

[27] Y. Nakashima, H. Suganuma, S. Yamashita, and J. Takahashi, *Evaluation of flexural modulus of ultra-thin chopped carbon fiber tape reinforced thermoplastics*, 2016.

[28] Y. Wan and J. Takahashi, *Effect of tape length and impregnation conditions on mechanical properties of carbon fiber tape reinforced thermoplastics*, 2015.

[29] P. Feraboli, E. Peitso, T. Cleveland, P. B. Stickler, and J. C. Halpin, "Notched behavior of prepreg-based discontinuous carbon fiber/epoxy systems," *Composites Part a-Applied Science and Manufacturing,* vol. 40, pp. 289-299, Mar 2009.

[30] P. Feraboli, E. Peitso, F. Deleo, T. Cleveland, and P. B. Stickler, "Characterization of prepreg-based discontinuous carbon fiber/epoxy systems," *Journal of reinforced plastics and composites,* vol. 28, pp. 1191-1214, 2009.

[31] B. C. Jin, X. Li, A. Jain, C. González, J. Llorca, and S. Nutt, "Optimization of microstructures and mechanical properties of composite oriented strand board from reused prepreg," *Composite Structures,* vol. 174, pp. 389-398, 8/15/ 2017.

[32] S. Yamashita, K. Hashimoto, H. Suganuma, and J. Takahashi, *Experimental characterization of the tensile failure mode of ultra-thin chopped carbon fiber tape-reinforced thermoplastics* vol. 35, 2016.

[33] P. R. Barnett, S. A. Young, and D. Penumadu, "Chopped Carbon Fiber Reinforced Thermoplastic Composites," presented at the American Society for Composites - 32nd Technical Conference, West Lafayette, Indiana, 2017.

[34] Y. Sato, J. Takahashi, T. Matsuo, I. Ohsawa, K. Kiriyama, and S. Nagoh, "Elastic modulus estimation of chopped carbon fiber tape reinforced thermoplastics using the Monte Carlo simulation."

[35] R. A. Cutting, A. J. Favaloro, J. E. Goodsell, and B. Pipes, "Determining Elastic Properties from the Dynamic Response of Discontinuous Fiber Composites," presented at the American Society for Composites - 32nd Technical Conference, West Lafayette, Indiana, 2017.

[36] M. Hashimoto, T. Okabe, T. Sasayama, H. Matsutani, and M. Nishikawa, *Prediction of tensile strength of discontinuous carbon fiber/polypropylene composite with fiber orientation distribution* vol. 43, 2012.

[37] L. Harper, C. Qian, R. Luchoo, and N. Warrior, "3D geometric modelling of discontinuous fibre composites using a force-directed algorithm," *Journal of Composite Materials,* vol. 51, pp. 2389-2406, 2017.

[38] H. Liu, D. Zeng, Y. Li, and L. Jiang, "Development of RVE-embedded solid elements model for predicting effective elastic constants of discontinuous fiber reinforced composites," *Mechanics of Materials,* vol. 93, pp. 109-123, 2016/02/01/ 2016.

[39] G. Twigg, A. Poursartip, and G. Fernlund, "Tool–part interaction in composites processing. Part I: experimental investigation and analytical model," *Composites Part A: Applied Science and Manufacturing,* vol. 35, pp. 121-133, 2004/01/01/ 2004.

[40] G. Jeronimidis and A. T. Parkyn, "Residual Stresses in Carbon Fibre-Thermoplastic Matrix Laminates," *Journal of Composite Materials,* vol. 22, pp. 401-415, 1988/05/01 1988.

[41] W. J. Unger and J. S. Hansen, "The Effect of Thermal Processing on Residual Strain Development in Unidirectional Graphite Fibre Reinforced PEEK," *Journal of Composite Materials,* vol. 27, pp. 59-82, 1993/01/01 1993.

[42] P. P. Parlevliet, H. E. Bersee, and A. Beukers, "Residual stresses in thermoplastic composites–a study of the literature. Part III: Effects of thermal residual stresses," *Composites Part A: Applied Science and Manufacturing,* vol. 38, pp. 1581-1596, 2007.

[43] P. P. Parlevliet, H. E. N. Bersee, and A. Beukers, "Residual stresses in thermoplastic composites—A study of the literature—Part I: Formation of residual stresses," *Composites Part A: Applied Science and Manufacturing,* vol. 37, pp. 1847-1857, 2006/11/01/ 2006.

[44] A. Johnston, "An Integrated Model of the Development of Process-Induced Deformation in Autoclave Processing of Composite Structures," Doctor of Philosophy, Department of Metals and Materials Engineering, University of British Columbia, 1997.

[45] F. N. Cogswell, "The experience of thermoplastic structural composites during processing," *Composites Manufacturing,* vol. 2, pp. 208-216, 1991/01/01/ 1991.

[46] T. A. Bogetti and J. W. Gillespie, "Process-Induced Stress and Deformation in Thick-Section Thermoset Composite Laminates," *Journal of Composite Materials,* vol. 26, pp. 626-660, 1992/03/01 1992.

[47] C. Albert and G. Fernlund, "Spring-in and warpage of angled composite laminates," *Composites Science and Technology,* vol. 62, pp. 1895-1912, 2002/11/01/ 2002.

[48] H. Hahn and N. Pagano, "Curing stresses in composite laminates," *Journal of Composite Materials,* vol. 9, pp. 91-106, 1975.

[49] H. T. Hahn, "Residual stresses in polymer matrix composite laminates," *Journal of Composite Materials,* vol. 10, pp. 266-278, 1976.

[50] I. Daniel and T. Liber, "Lamination Residual Stresses in Fiber Composites," IIT RESEARCH INST CHICAGO IL1973.

[51] I. Daniel and T. Liber, "Effect of laminate construction on residual stresses in graphite/polyimide composites," *Experimental Mechanics,* vol. 17, pp. 21-25, 1977.

[52] I. Daniel and T. Liber, "Measurement of Lamination Residual Strains in Graphite Fiber Laminates," presented at the Second International Conference on Mechanical Behaviour of Materials, ICM-II, Boston, MA, 1976.

[53] P. Hubert, "Aspects of flow and compaction of laminated composite shapes during cure," Doctor of Philosophy, Department of Metals and Materials Engineering, University of British Columbia, 1996.

[54] T. SREEKANTAMURTHY, T. HUDSON, T.-H. HOU, and B. GRIMSLEY, "Composite Cure Process Modeling and Simulations using COMPRO® and Validation of Residual Strains using Fiber Optics Sensors," in *Proceedings of the American Society for Composites: Thirty-First Technical Conference*, 2016.

[55] J. A. Barnes and G. E. Byerly, "The formation of residual stresses in laminated thermoplastic composites," *Composites Science and Technology,* vol. 51, pp. 479-494, 1994/01/01/ 1994.

[56] W. J. Unger and J. S. Hansen, "The Effect of Cooling Rate and Annealing on Residual Stress Development in Graphite Fibre Reinforced PEEK Laminates," *Journal of Composite Materials,* vol. 27, pp. 108-137, 1993/02/01 1993.

[57] (2005, Shrinkage and Warpage. Available: http://www.dc.engr.scu.edu/cmdoc/dg_doc/develop/process/physics/b3500001.htm#211482

[58] Q.-s. Jiang, H.-s. Liu, Z.-w. Xiao, S.-f. Chou, A.-h. Xiong, and H.-r. Nie, "Three-dimensional numerical simulation of total warpage deformation for short-glass-fiber-reinforced polypropylene composite injection-molded parts using coupled FEM," *Journal of Polymer Engineering,* 2017.

[59] SABIC Innovative Plastics. (2008, Understanding shrinkage and warpage of reinforced and filled thermoplastics. Available: http://www.pod-sabic-ip.com/KBAM/Reflection/Assets/Thumbnail/7107_17.pdf

[60] R. Zheng, P. Kennedy, N. Phan-Thien, and X. Fan, "Thermoviscoelastic simulation of thermally and pressure-induced stresses in injection moulding for the prediction of shrinkage and warpage for fibre-reinforced thermoplastics," *Journal of Non-Newtonian Fluid Mechanics,* vol. 84, pp. 159-190, 1999.

[61] S. Taghizadeh, A. Özdemir, and O. Uluer, "Warpage prediction in plastic injection molded part using artificial neural network," *Iranian Journal of Science and Technology. Transactions of Mechanical Engineering,* vol. 37, p. 149, 2013.

[62] W. Guo, L. Hua, H. Mao, and Z. Meng, "Prediction of warpage in plastic injection molding based on design of experiments," *Journal of Mechanical Science and Technology,* vol. 26, p. 1133, 2012.

[63] B. Landry, "Experimental study and numerical simulation of defect formation during compression moulding of discontinuous long fibre carbon/PEEK composites," Doctor of Philosophy, Department of Mechanical Engineering, McGill University, 2015.

[64] C. Wang and C. T. Sun, "Thermoelastic Behavior of PEEK Thermoplastic Composite during Cooling from Forming Temperatures," *Journal of Composite Materials,* vol. 31, pp. 2230-2248, 1997/11/01 1997.

[65] T. J. Chapman, J. Gillespie Jr, B. Pipes, J. A. E. Månson, and J. Seferis, *Prediction of Process-Induced Residual Stresses in Thermoplastic Composites* vol. 24, 1990.

[66] M. Selezneva, "Experimental and Theoretical Investigations of Mechanical Properties of Randomly-Oriented Strand (ROS) Composites," Doctor of Philosophy, Department of Mechanical Engineering, McGill University, 2015.

[67] Hexcel;, "HexTow AS4 Carbon Fiber," ed, 2016.

[68] D. LeBlanc, "Compression moulding of complex parts with randomly-oriented strand thermoplastic composites," Master's of Engineering, Department of Mechanical Engineering, McGill University, 2014.

[69] W. Hufenbach and M. Gude, "Analysis and optimisation of multistable composites under residual stresses," *Composite Structures,* vol. 55, pp. 319-327, 2002/02/01/ 2002.

[70] Bayer Corporation, "Part and Mold Design: Thermoplastics," 2000.

[71] S. Nykanen, "Ribs," in *Mould Design*, ed: Tampere University of Technology, 2007.

[72] H. Lee, C. Bi, S. Tang, T. Hayashi, and J. Takahashi, "Formability and flow front observation of carbon/polyamide 6 randomly oriented strand composites during compression molding," *Journal of Reinforced Plastics and Composites,* p. 0731684417725583, 2017.

[73] D. Kobayashi, Y. Wan, L. Hanchul, T. Nakamura, H. Wei, J. Takahashi*, et al.*, *Flow behavior of complex shaped hybrid CFRTP during compression molding*, 2016.

[74] D. LeBlanc, B. Landry, A. Levy, P. Hubert, S. Roy, and A. Yousefpour, "Compression moulding of complex parts using randomly-oriented strands thermoplastic composites," in *SAMPE Tech. Conf*, 2014, pp. 2-4.

[75] X. Gagné Brulotte, "Aspects of in-situ consolidation of thermoplastic laminates manufactured by automated tape placement: a material deformation study," Master of Engineering, Department of Mechanical Engineering, McGill University, Montreal, QC, 2012.

Appendix A

Flat Panel Data

A.1 Small Panel Warpage Plots

The panels were measured using a FARO® ScanArm. Each part's unique point cloud was converted into a 3D model in Geomagic Studio and exported as an STL file. Using InnovMetric's PolyWorks® inspection software, these unique part models were aligned with 3D models of perfectly flat panels using a best-fit approximation and electronically probed to determine their deviation from a flat surface. The deviations are captured in the following figures.

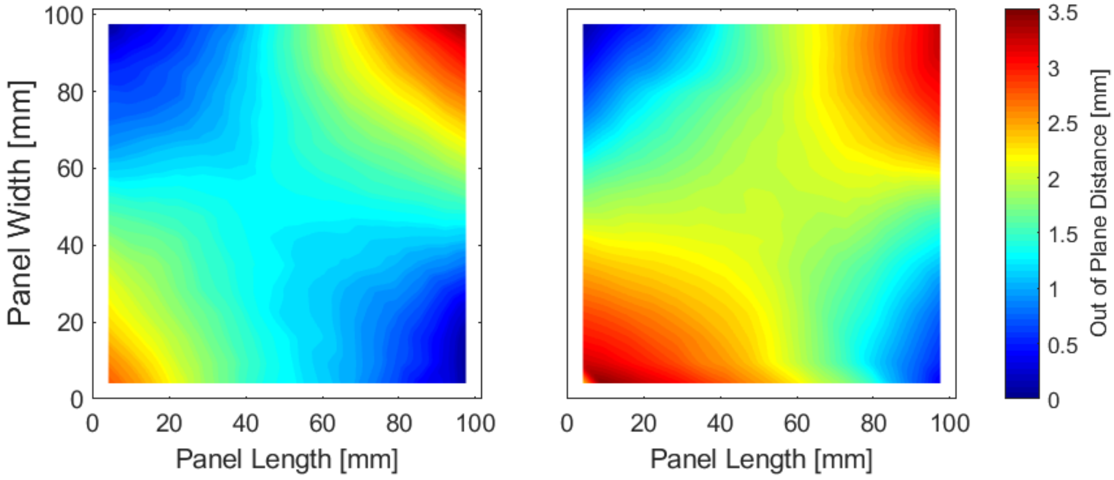

Figure A. 1: Warpage in 1.0 mm thick parts made with short strands.

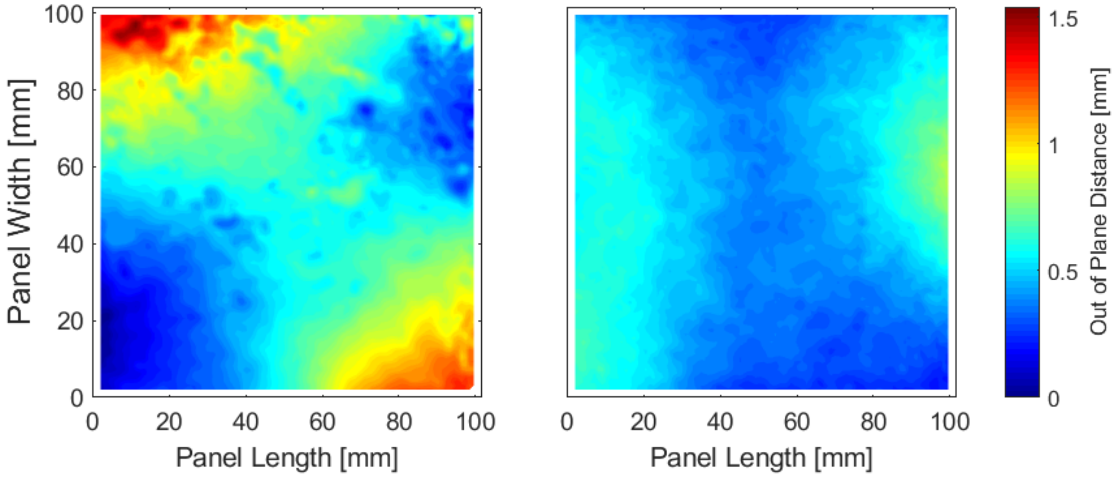

Figure A. 2: Warpage in 1.5 mm thick parts made with short strands.

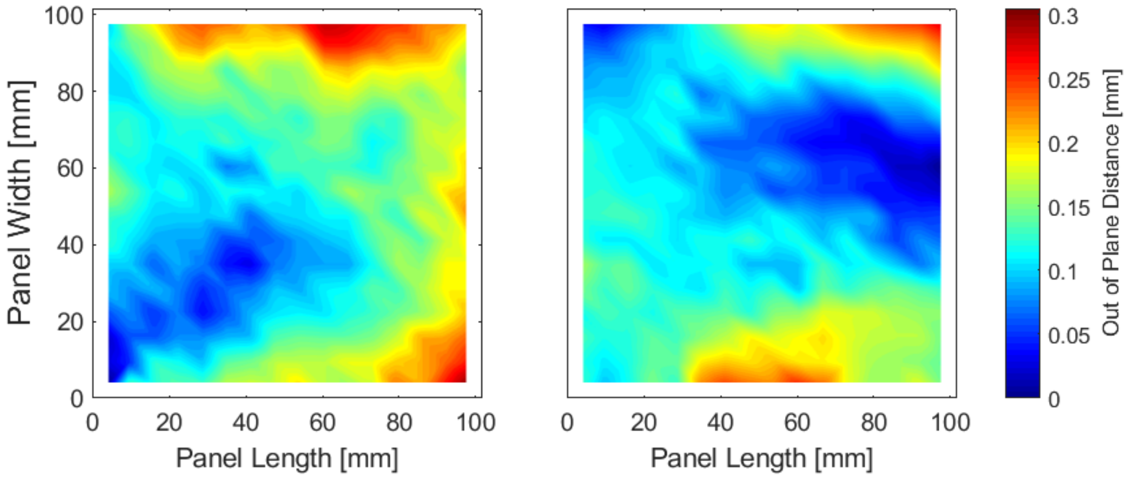

Figure A. 3: Warpage in 2.0 mm thick parts made with short strands.

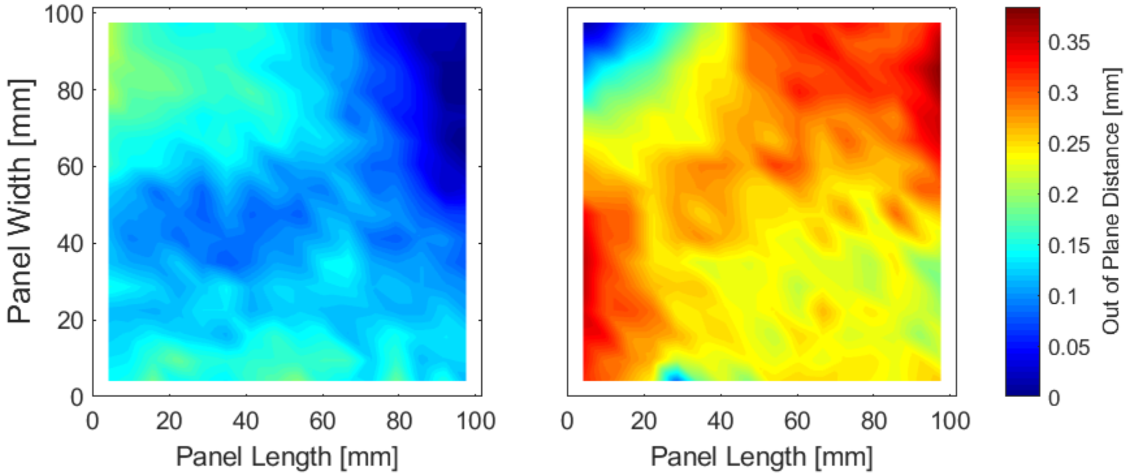

Figure A. 4: Warpage in 3.0 mm thick parts made with short strands.

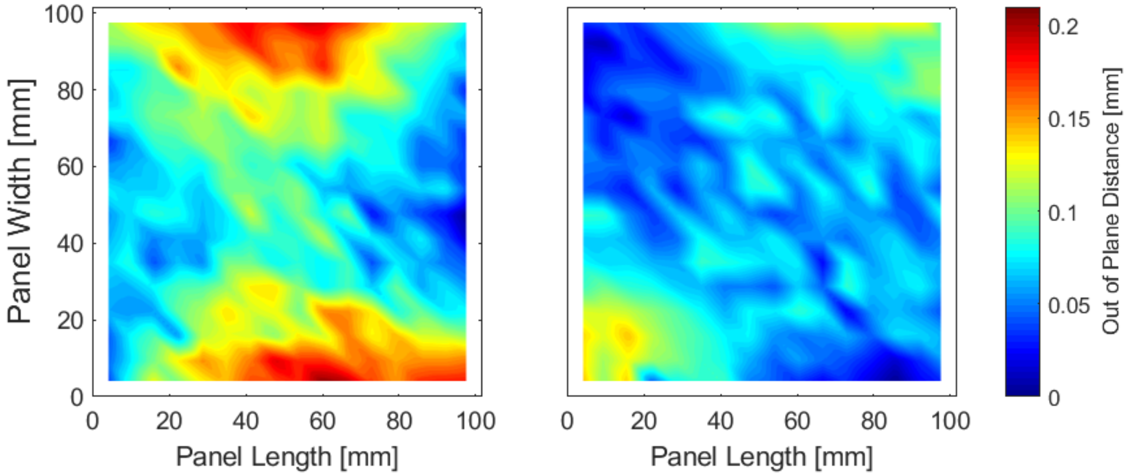

Figure A. 5: Warpage in 3.8 mm thick parts made with short strands.

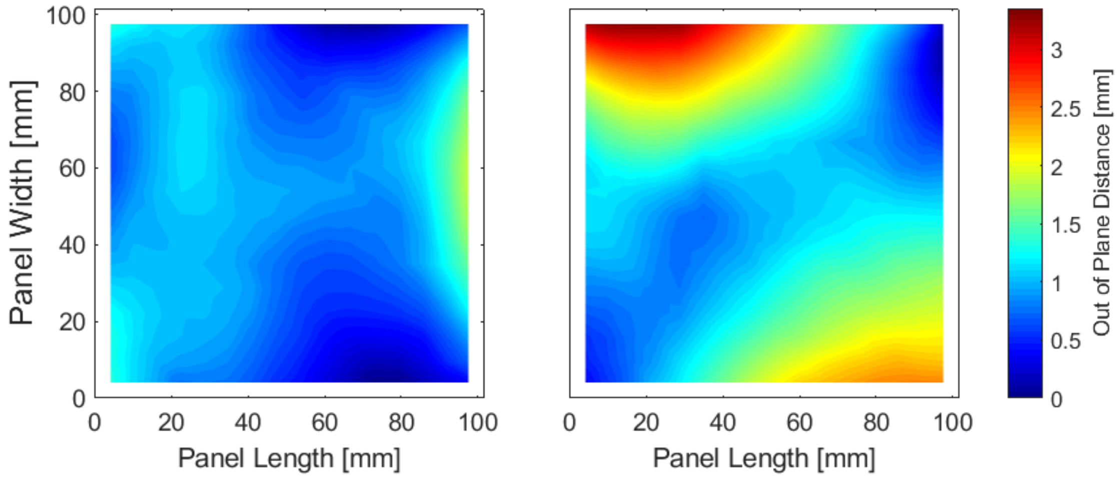

Figure A. 6: Warpage in 1.0 mm thick parts made with square strands.

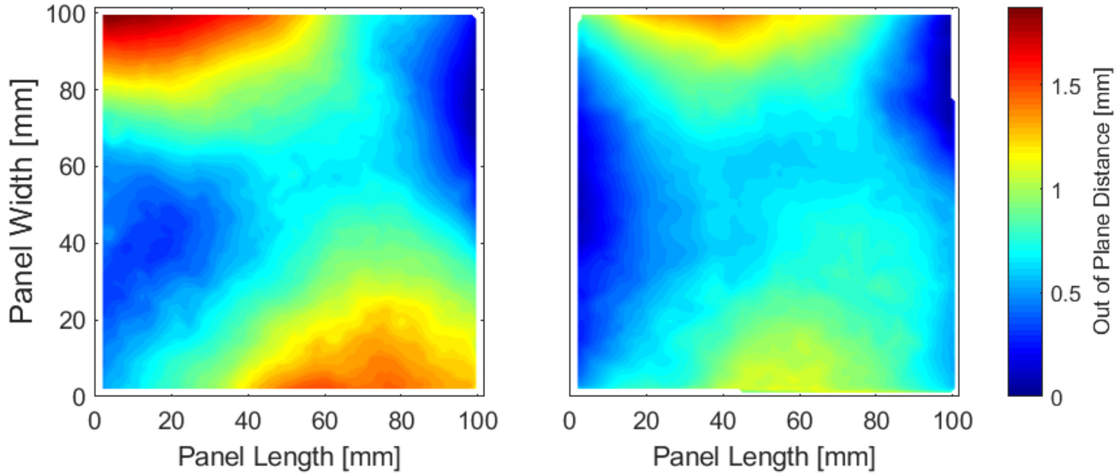

Figure A. 7: Warpage in 1.5 mm thick parts made with square strands.

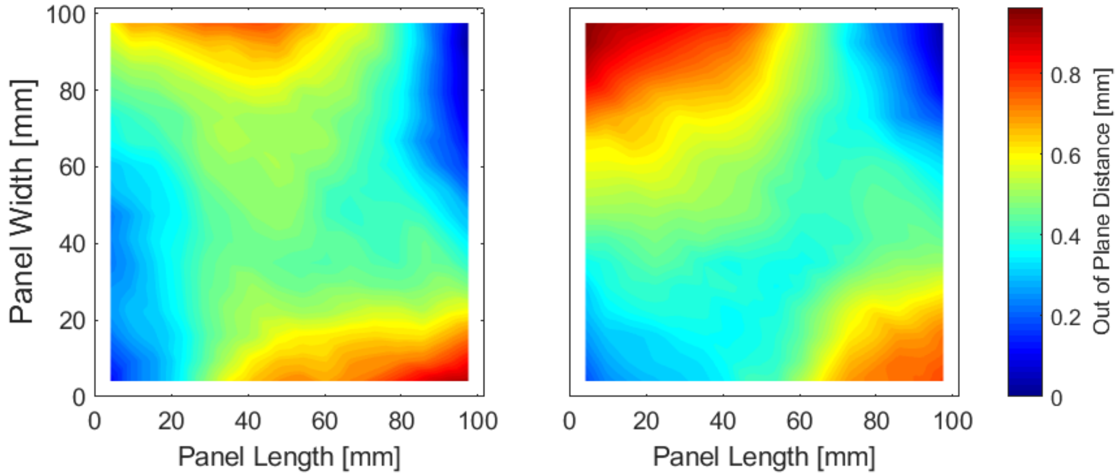

Figure A. 8: Warpage in 2.0 mm thick parts made with square strands.

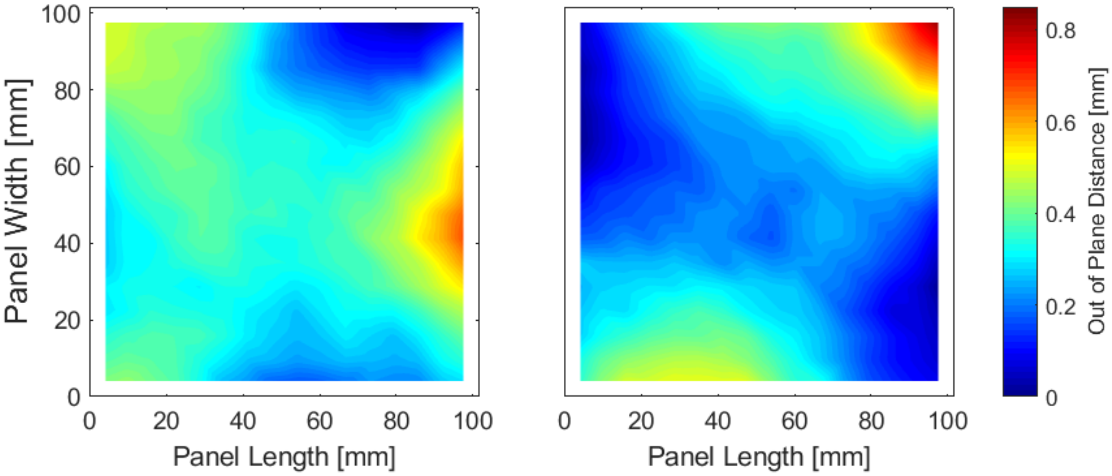

Figure A. 9: Warpage in 2.3 mm thick parts made with square strands.

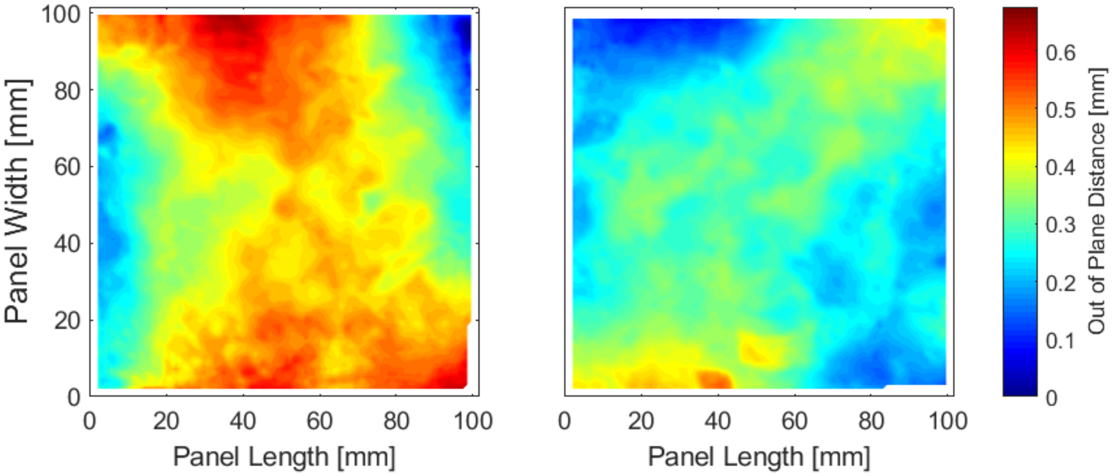

Figure A. 10: Warpage in 3.0 mm thick parts made with square strands.

A.2 Small Panel Thickness PlotsMeasurements

The results of the micrometer measurements of all panels are presented in the following figures.

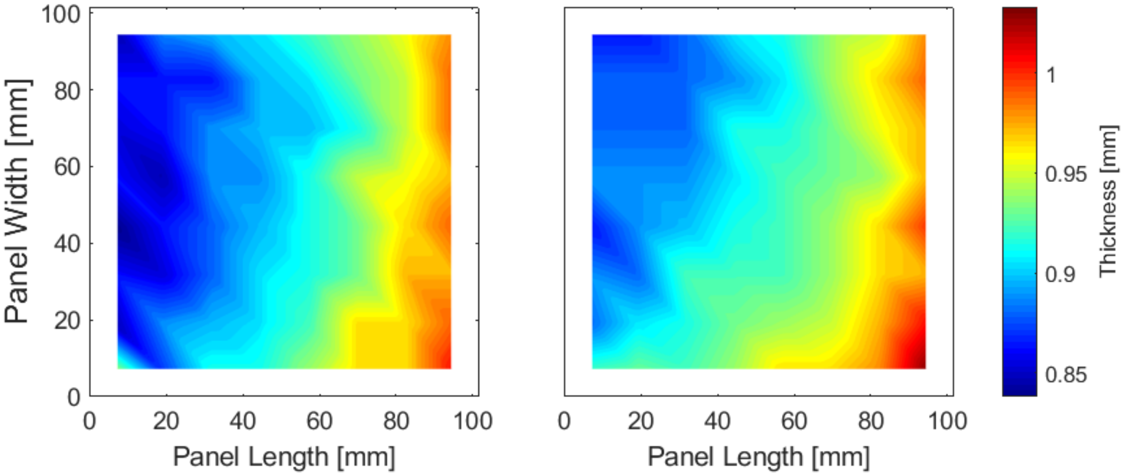

Figure A. 11: Thickness distribution in 1.0 mm thick parts made with short strands.

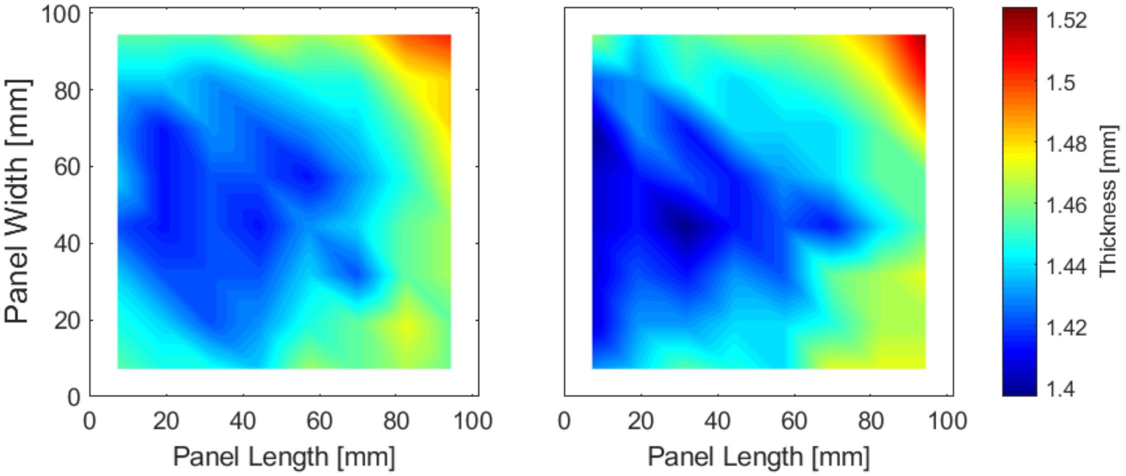

Figure A. 12: Thickness distribution in 1.5 mm thick parts made with short strands.

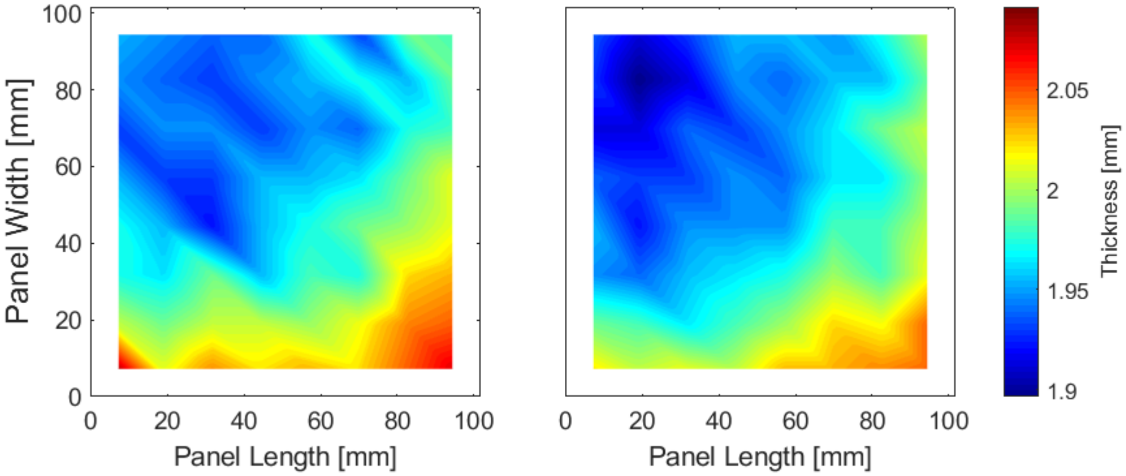

Figure A. 13: Thickness distribution in 2.0 mm thick parts made with short strands.

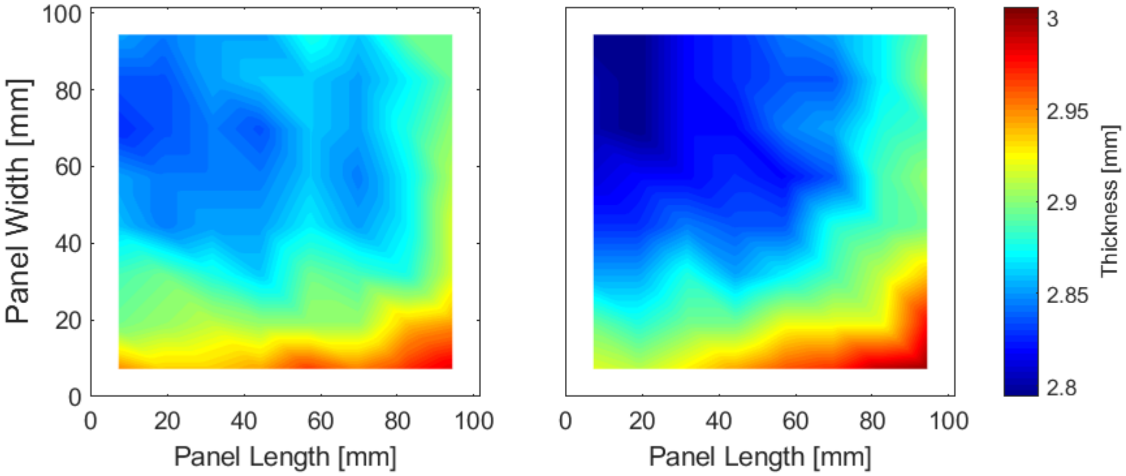

Figure A. 14: Thickness distribution in 3.0 mm thick parts made with short strands.

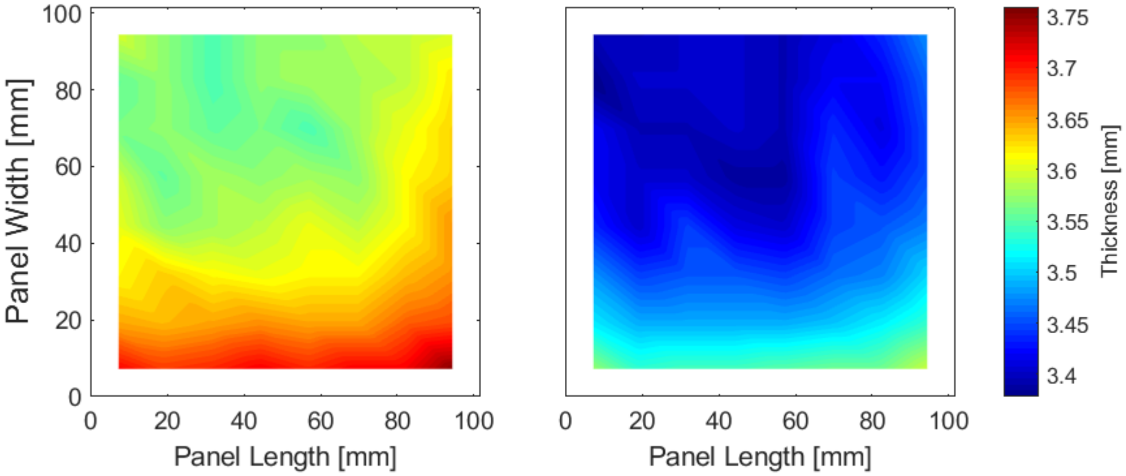

Figure A. 15: Thickness distribution in 3.8 mm thick parts made with short strands.

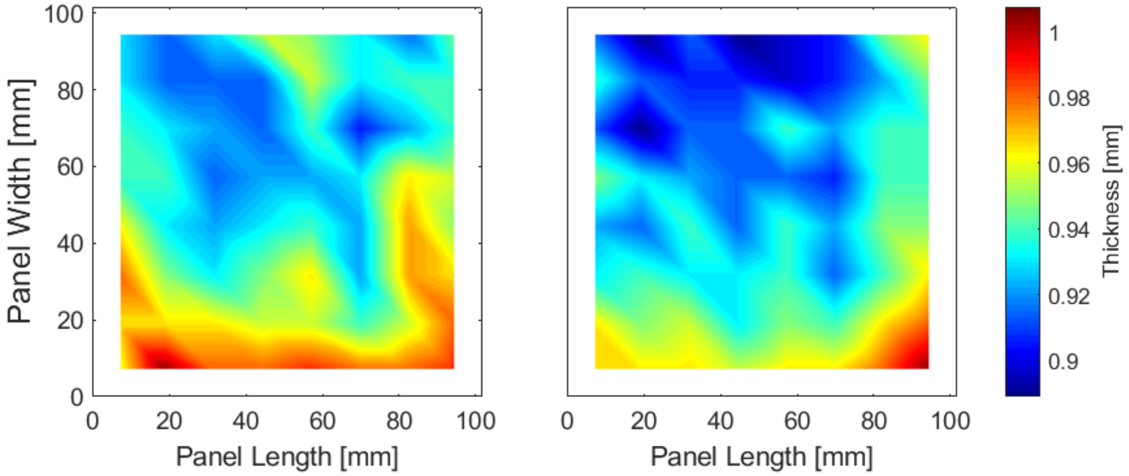

Figure A. 16: Thickness distribution in 1.0 mm thick parts made with square strands.

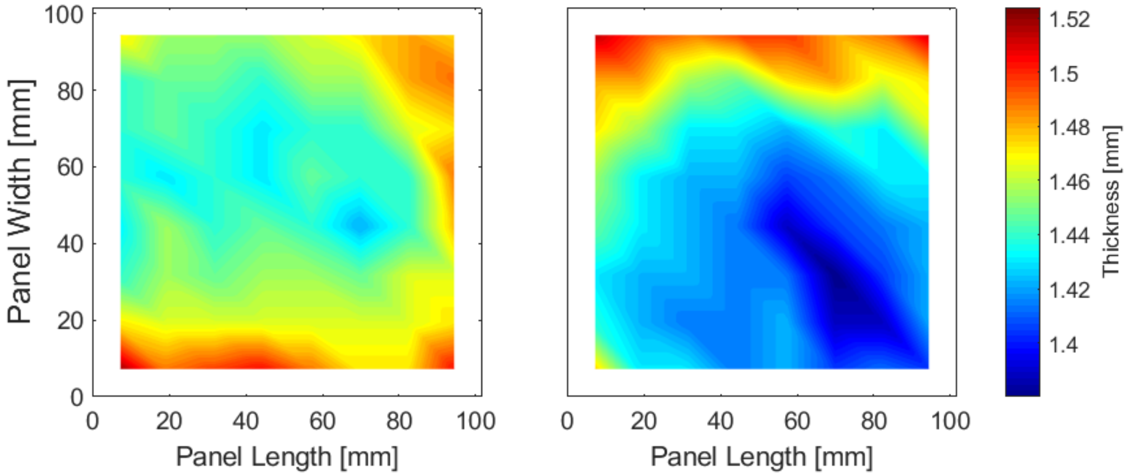

Figure A. 17: Thickness distribution in 1.5 mm thick parts made with square strands.

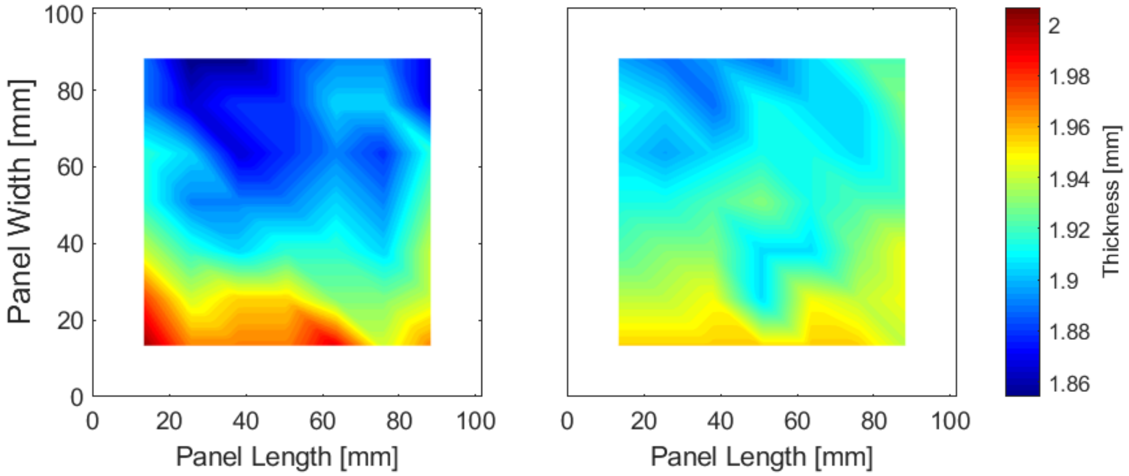

Figure A. 18: Thickness distribution in 2.0 mm thick parts made with square strands.

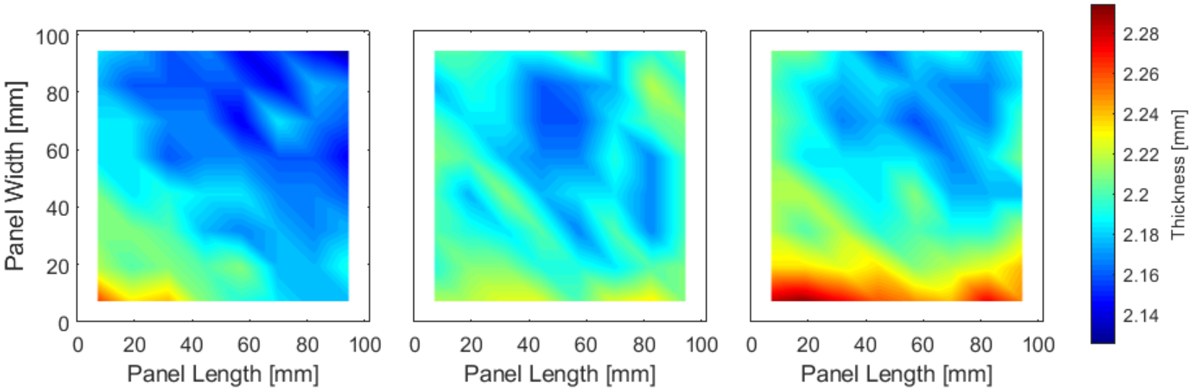

Figure A. 19: Thickness distribution in 2.3 mm thick parts made with square strands.

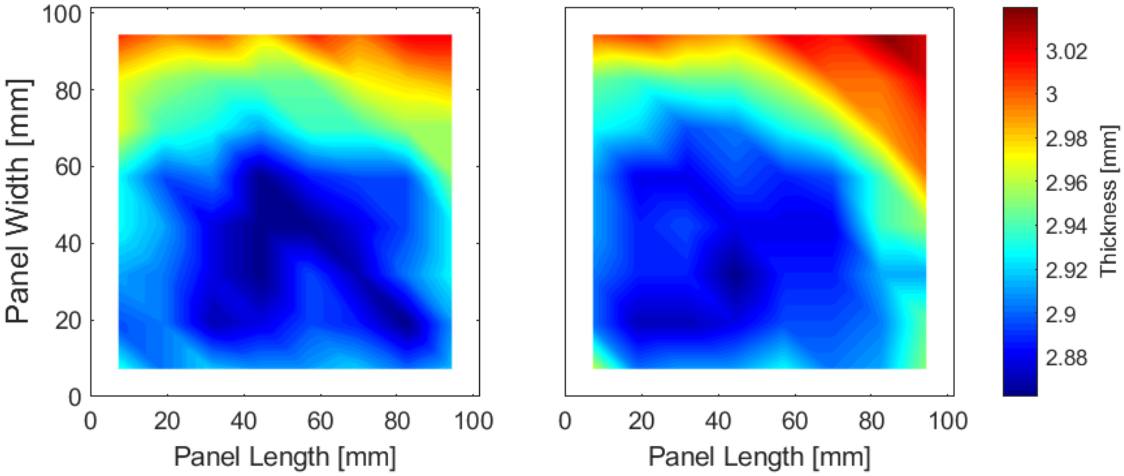

Figure A. 20: Thickness distribution in 3.0 mm thick parts made with square strands.

Appendix B

Instrumented Hot Press Pressure Distribution

B.1 Ribbed Part Thickness Assessment

Parts made in Chapter 3 – with parallel ribs of varying size and with evenly-spaced orthogonal ribs – were measured every 12.7 mm using an external micrometer from Mitutoyo (Part Number 118-107 with a 0-1” span) and all were found to have significant variations in thickness, with a distinctive thickness gradient, as seen in the following figures. In the figures, the ribs are oriented as if they are coming out of the page and indicated by the dotted white lines.

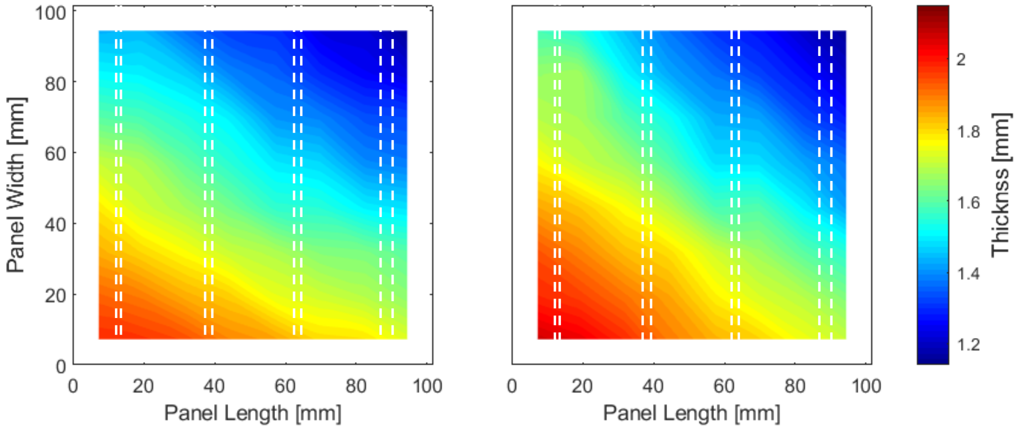

Figure B. 1: Thickness distribution in parts made with 6.35 mm x 3.18 mm strands at (a) 70 bar moulding pressure with uniform cooling and (b) 110 bar moulding pressure with cooling strategy.

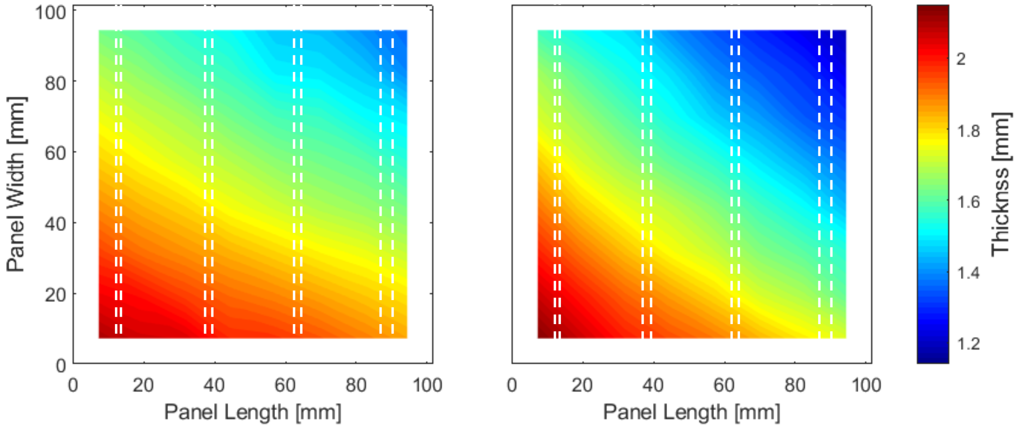

Figure B. 2: Thickness distribution in parts made with 12.70 mm x 12.70 mm strands at (a) 70 bar moulding pressure with uniform cooling and (b) 110 bar moulding pressure with cooling strategy.

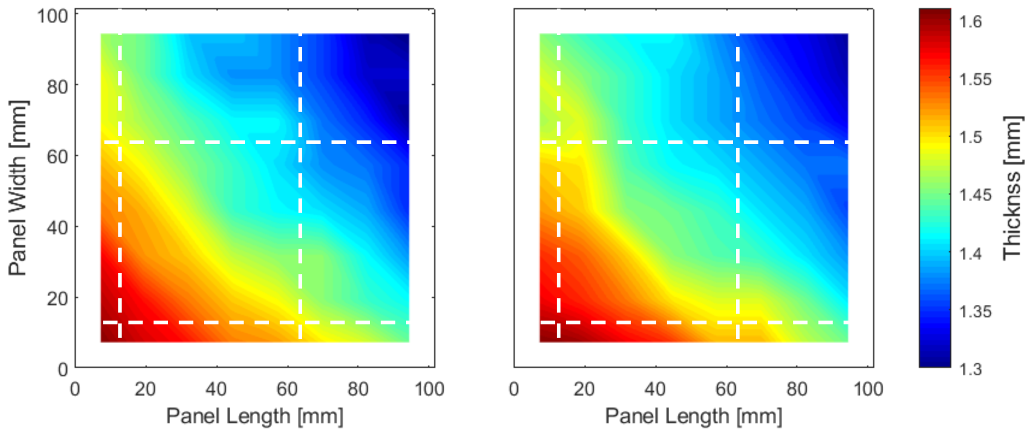

Figure B. 3: Thickness distribution in parts made with 6.35 mm x 3.18 mm strands to be 1.5 mm thick.

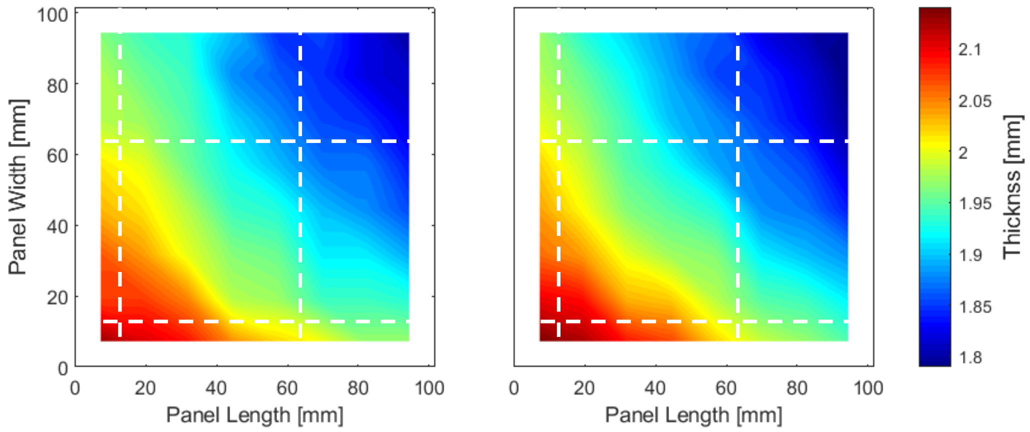

Figure B. 4: Thickness distribution in parts made with 6.35 mm x 3.18 mm strands to be 2.0 mm thick.

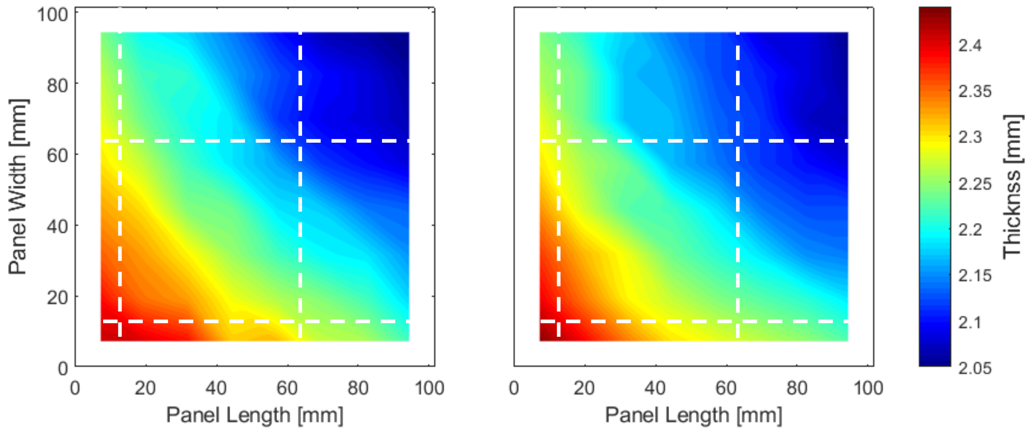

Figure B. 5: Thickness distribution in parts made with 12.70 mm x 12.70 mm strands to be 2.3 mm thick.

Since this thickness variation was not consistently seen in the flat panels manufactured in Chapter 2, and the inserts used to mould the ribbed parts were inspected and verified to be flat, the alignment of the instrumented hot press was questioned. To determine if there was an alignment issue, pressure sensitive films (Fujifilm Prescale, Medium Pressure, Monosheet type) were used to find the pressure distribution within the press.

B.2 Instrumented Hot Press Pressure Distribution Assessment

Imprints were taken on pressure films with the instrumented hot press in several configurations. First, imprints were taken directly between the press platens, as illustrated in Figure B. 6(a). Using the stacks of inserts in the configuration used for moulding, imprints were also taken between each insert and the platens as shown in Figure B. 6(b). Imprints were taken at ambient temperature and under approximately 110 bar of pressure (assuming even distribution in the press platens). The threshold for creating an imprint on the Fujifilm Prescale was 100 bar.

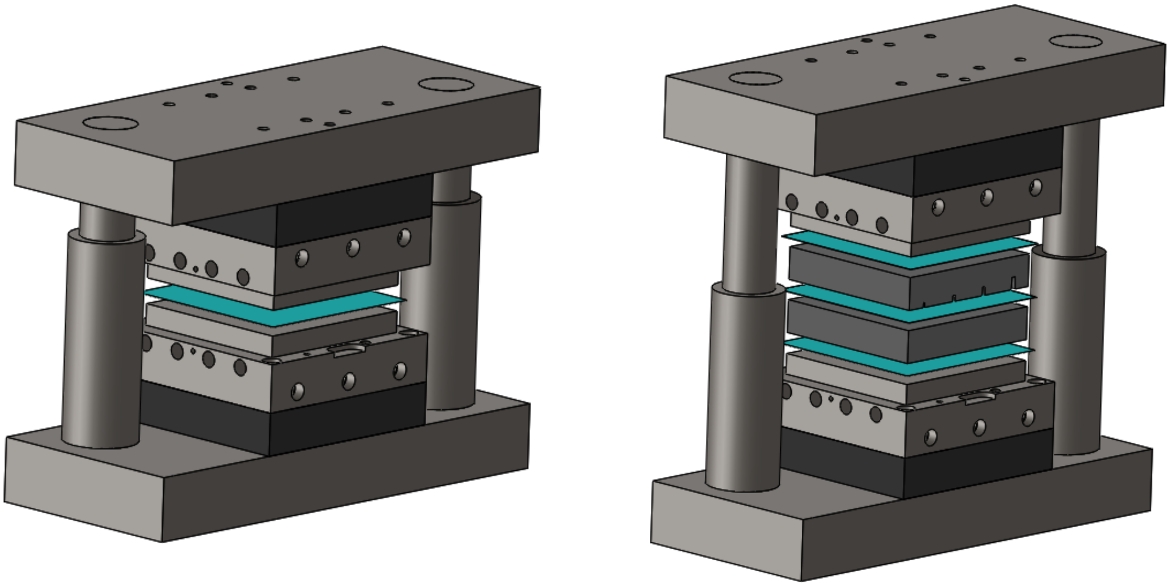
(a) (b)

Figure B. 6: Locations of pressure films for checking alignment of (a) press platens alone and (b) press platens with ribbed inserts. Pressure films are indicated in blue.

The imprints were scanned using a Xerox WorkCentre 7545. Images were captured at 600 dpi as TIFF files and read into MATLAB. Following a process similar to that described by Gagné Brulotte in [75], the images were converted to black and white, and inverted. Three scans of blank pressure films were taken and averaged to determine the average background intensity. The background was also inverted, and subtracted from the initial image. The images were smoothed using a gaussian filter and a standard deviation of 2, using the MATLAB command `imgaussfilt`. Finally, the intensity map left for the images could be converted to a pressure with Fujifilm's scale, represented in Equation 6.

$$P = 44.16479e^{0.025894(int)} \tag{6}$$

Where: P = Pressure

int = colour intensity of scanned image

The pressure images captured directly between press platens did not indicate the presence of a pressure gradient that would match the observed thickness gradient. The edges of the platen see the most pressure, as shown in the example in Figure B. 7.

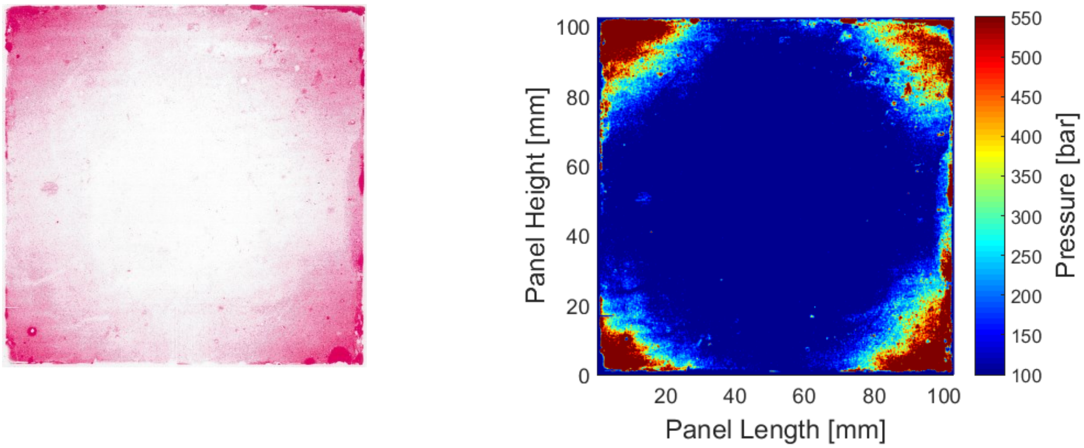

(a) (b)

Figure B. 7: (a) Prescale film imprint taken between platens and (b) resulting pressure map.

When assessing the pressure films taken with the mould inserts in place, a gradient similar to that seen in the thickness distributions is apparent – with the lowest pressure in the bottom, left corner, corresponding with the thickest section of the produced parts. Looking at each film individually, the gradient is subtle, particularly in Figure B. 8.

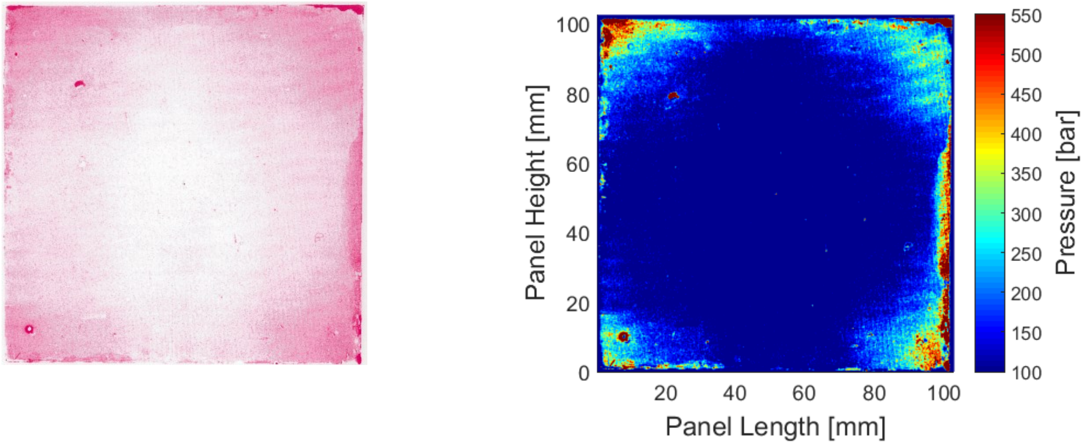

(a) (b)

Figure B. 8: (a) Prescale film imprint taken between bottom platen and flat insert. (b) Resulting pressure map.

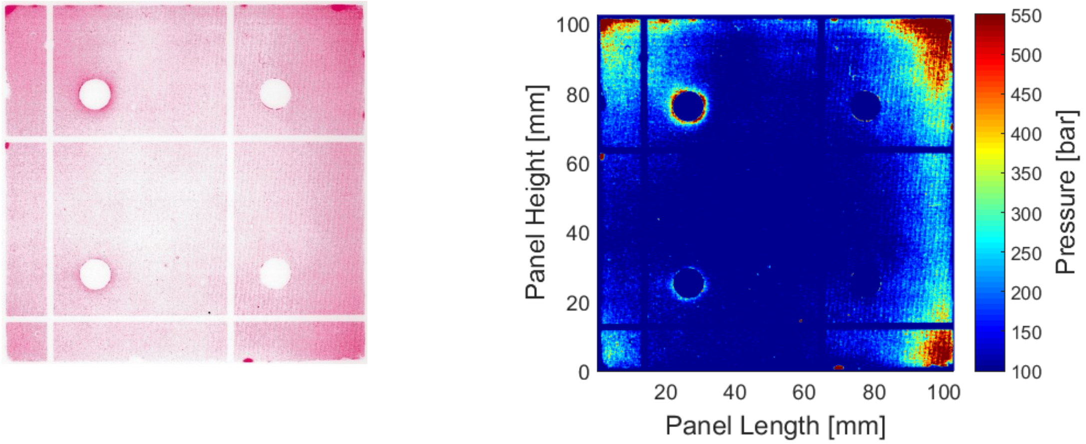

(a) (b)

Figure B. 9: (a) Prescale film imprint taken between flat insert and orthogonally ribbed insert. (b) Resulting pressure map.

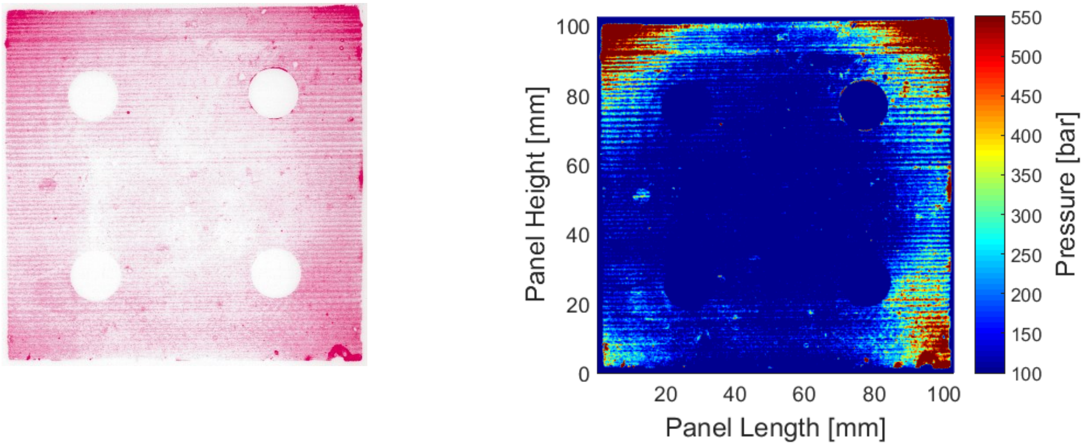

(a) (b)

Figure B. 10: (a) Prescale film imprint taken between orthogonally ribbed insert and top platen. (b) Resulting pressure map.

When comparing the topmost film (from between the top platen and ribbed insert) relative to the bottommost film (from between the bottom platen and the flat insert) via subtraction, the pressure gradient is very evident, as seen in Figure B. 11.

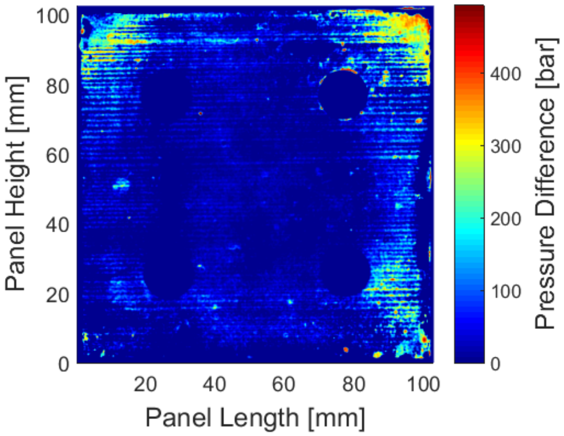

Figure B. 11: Pressure gradient at top platen, relative to pressure gradient at bottom platen.

This gradient exists regardless of insert orientation. For example, in Figure B. 12(a), the ribbed insert is rotated 90° from its orientation in Figure B. 11. In Figure B. 12(b), the flat block has been rotated 90° from the previous position as well (with ribbed block in the same position as in Figure B. 12(a)) and the same pressure distribution is seen, with the lowest pressure at the bottom left corner where the produced parts were thickest.

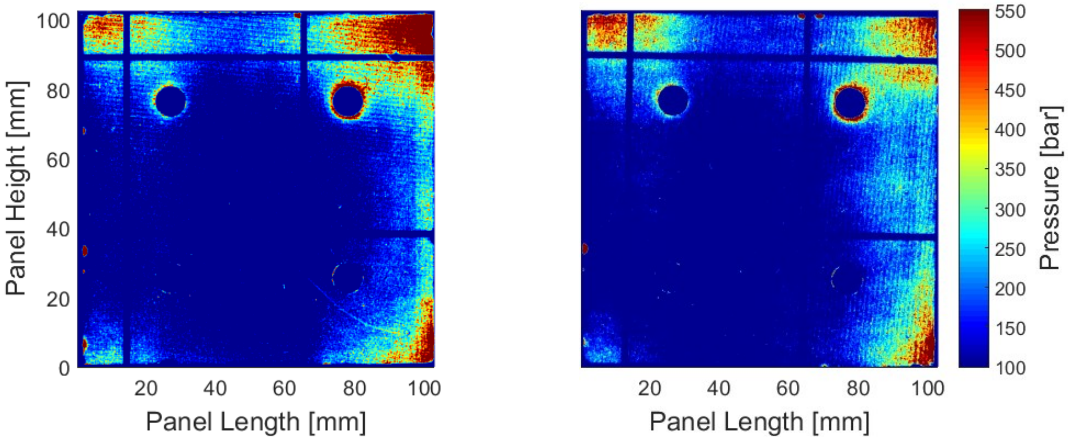

(a) (b)

Figure B. 12: Pressure gradients taken between block and orthogonally ribbed insert when (a) ribbed insert is rotated 90° relative to its position in Figure B. 9 and (b) both block and insert are rotated 90° relative to their positions Figure B. 9.

B.3 Summary

From the pressure distribution measurements taken using Fujifilm Prescale pressure films, it is apparent that the thickness gradients found in the produced ribbed parts were in part due to misalignment in the press. This misalignment does not appear to be present when moulding flat plates, but becomes apparent when the additional height of the ribbed inserts is added.

Appendix C

Ribbed Panel Data

C.1 Moulded Parts with Orthogonal Ribs

Ribbed parts of varying sizes were moulded with smooth surfaces, indicating that the cooling strategy had the intended effect. Figure C. 1 shows the rib-side of all parts.

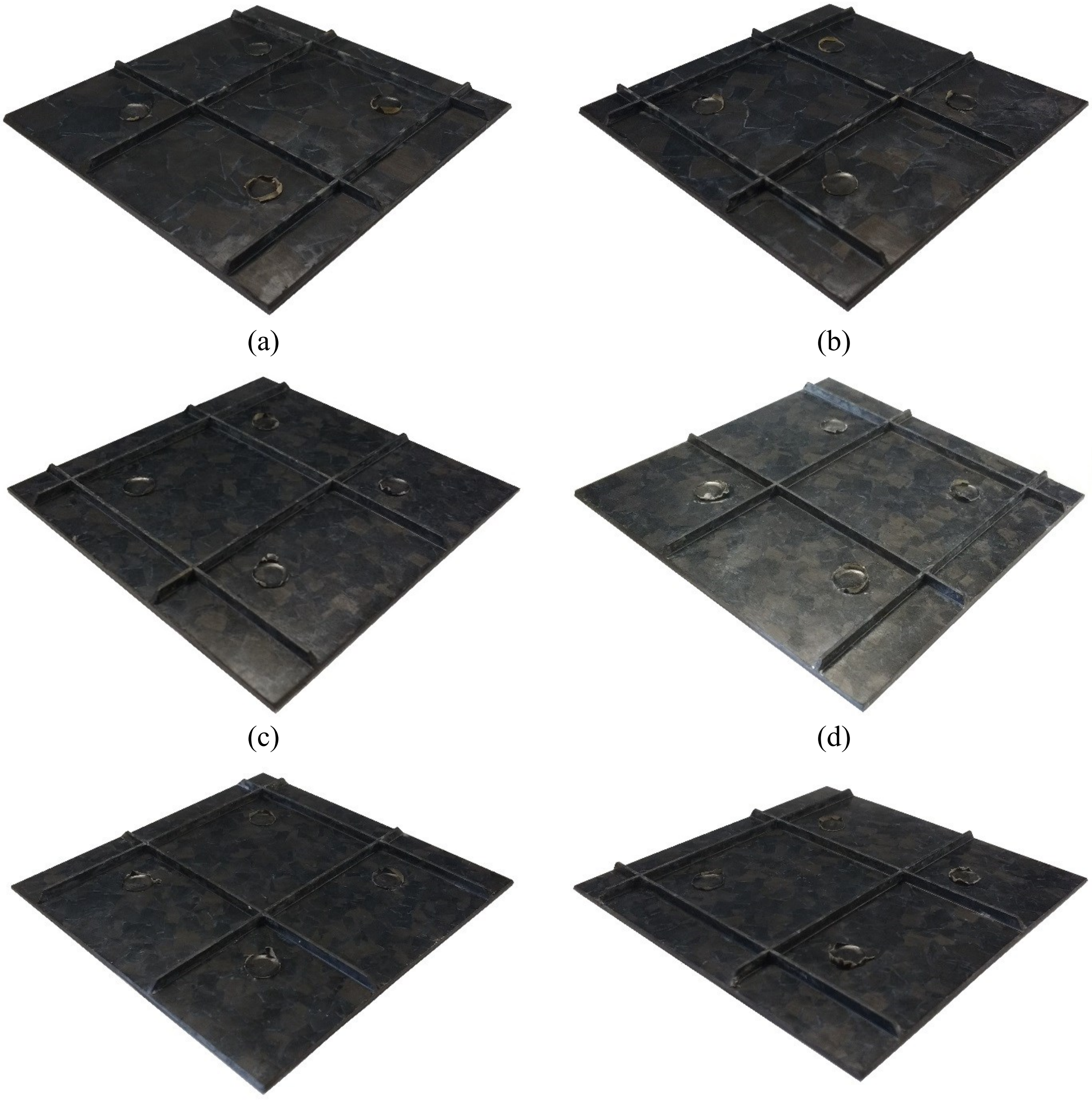

(a) (b)

(c) (d)

(e) (f)

Figure C. 1: Parts made (a,b) with square strands, 2.3 mm thick; (c,d) with short strands, 2.0 mm thick; (e,f) with short strands, 1.5 mm thick.

C.2 Ribbed Panel Warpage Measurements

The panels were measured using a FARO® ScanArm. Each part's unique point cloud was converted into a 3D model in Geomagic Studio and exported as an STL file. Using InnovMetric's PolyWorks® inspection software, these unique part models were aligned with 3D models of perfectly flat panels using a best-fit approximation and electronically probed to determine their deviation from a flat surface.

C.2.1 Full Part Warpage

The following images are oriented as if the ribs, represented by the white dashed lines, are coming out of the page.

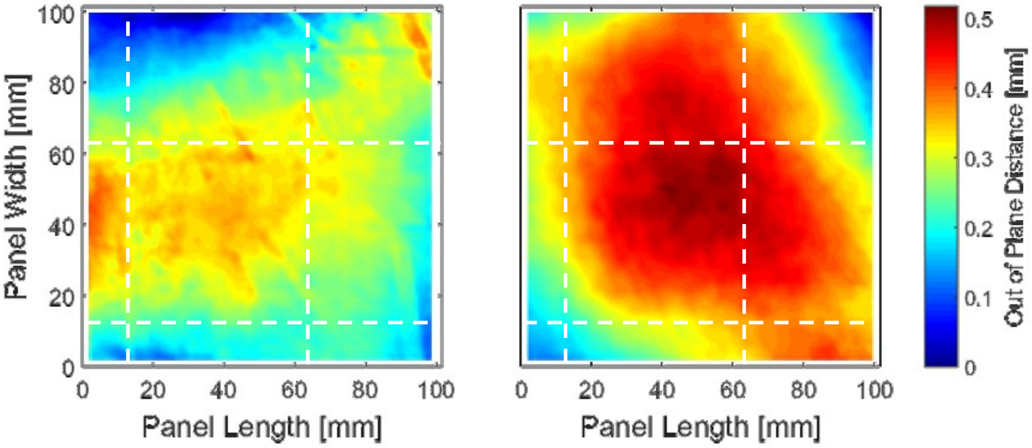

Figure C. 2: Warpage in parts made with short strands to be 2.0 mm thick.

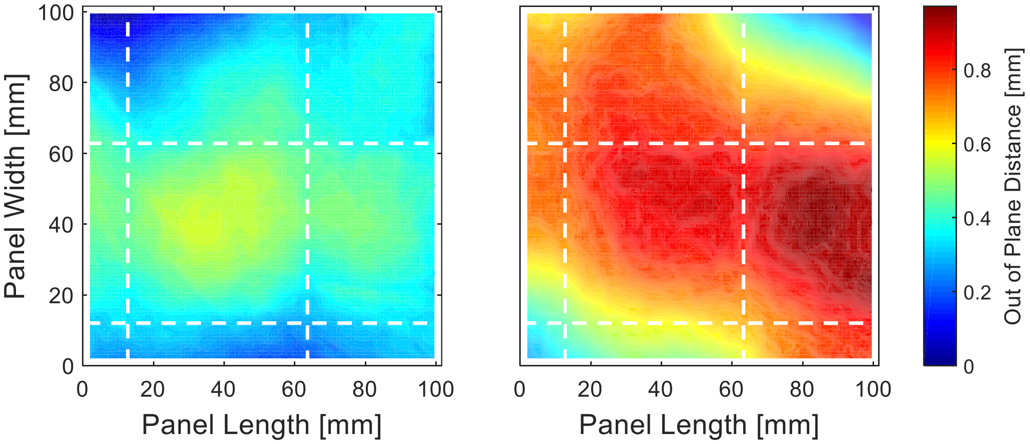

Figure C. 3: Warpage in parts made with short strands to be 1.5 mm thick.

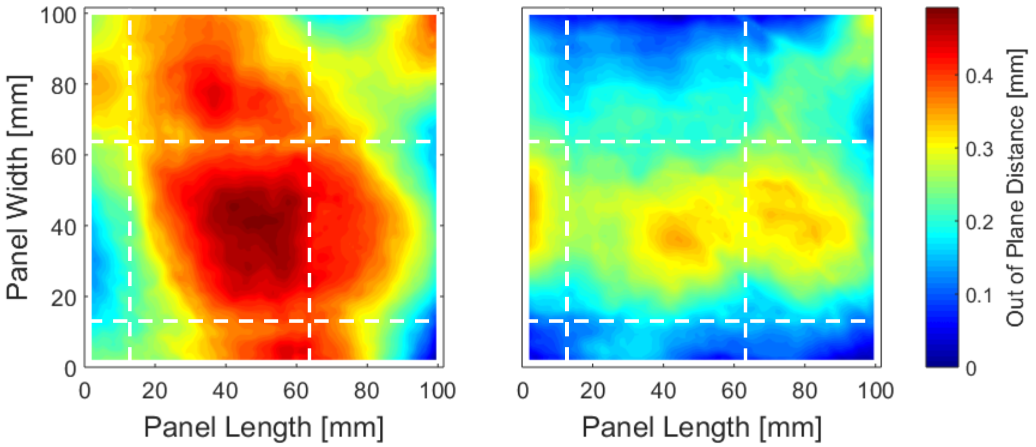

Figure C. 4: Warpage in parts made with square strands to be 2.3 mm thick.

C.2.2 Fully-Supported Section Warpage

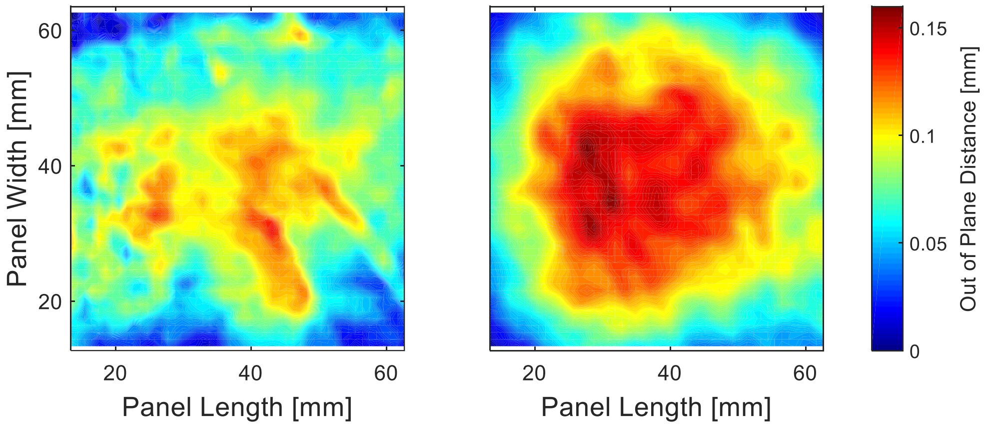

Figure C. 5: Warpage in supported section of 2.0 mm thick ribbed parts made with short strands.

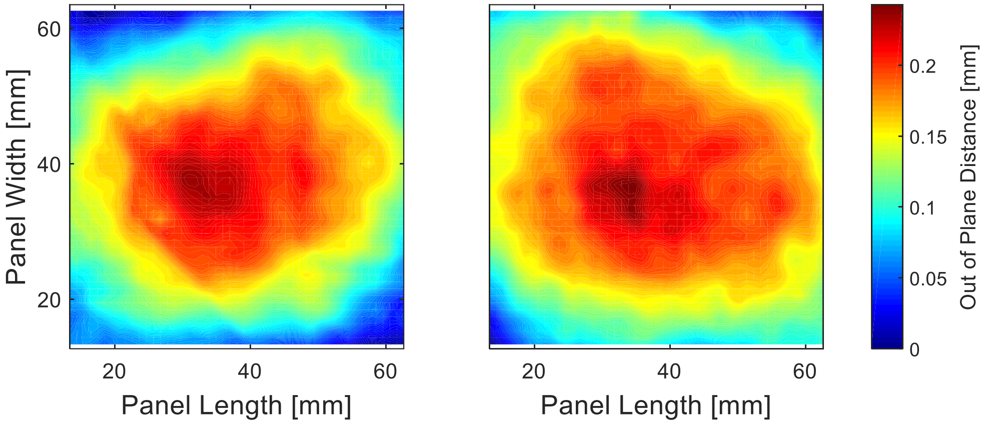

Figure C. 6: Warpage in supported section of 1.5 mm thick ribbed parts made with short strands.

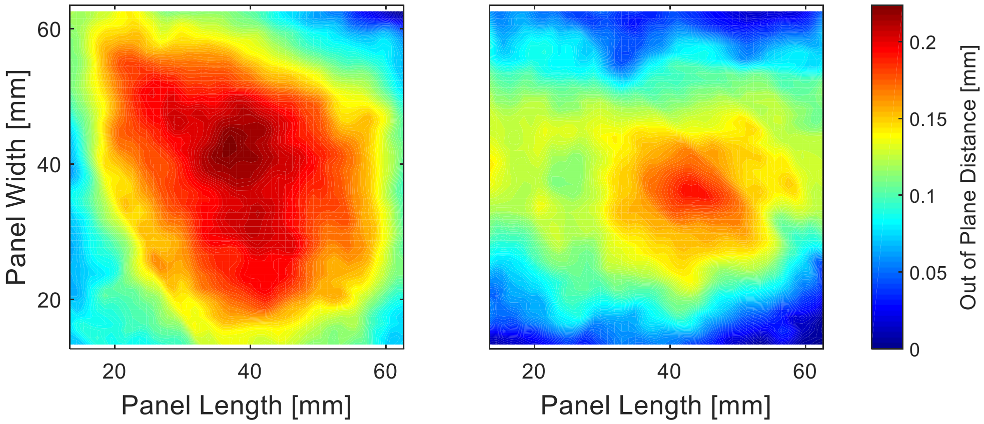

Figure C. 7: Warpage in supported section of 2.3 mm thick ribbed parts made with square strands.

C.3 Thickness Measurements

All parts were measured every 0.5 in using external micrometer from Mitutoyo (Part Number 118-107 with a 0-1” span) and all were found to have similar variations in thickness, with the thinnest sections along the side of the part where the cooling inlet would be and the thickest sections closest to the cooling outlet. The following figures show the thickness distributions. The images are oriented as if the ribs are coming out of the page, where indicated by the dotted white lines.

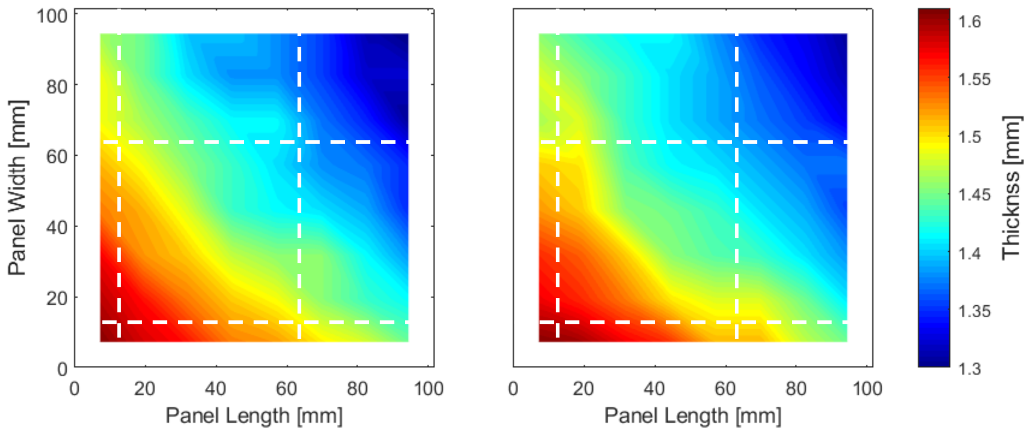

Figure C. 8: Thickness distribution in parts made with short strands to be 1.5 mm thick.

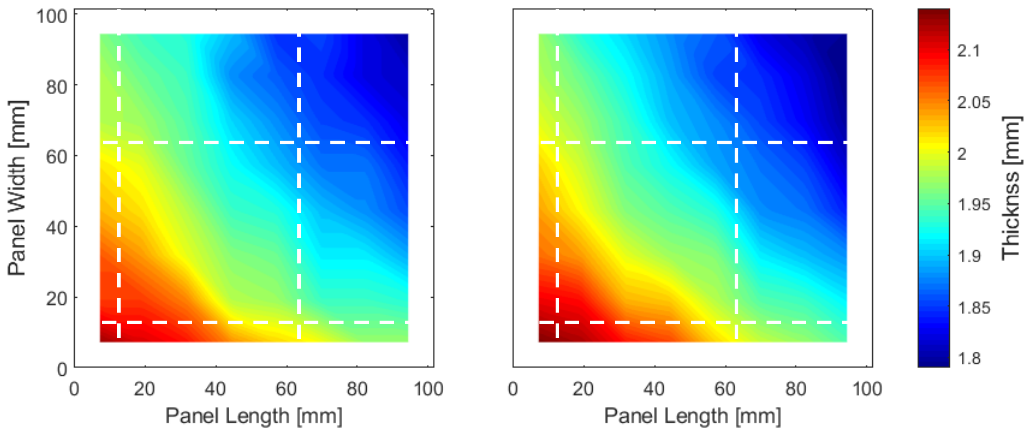

Figure C. 9: Thickness distribution in parts made with short strands to be 2.0 mm thick.

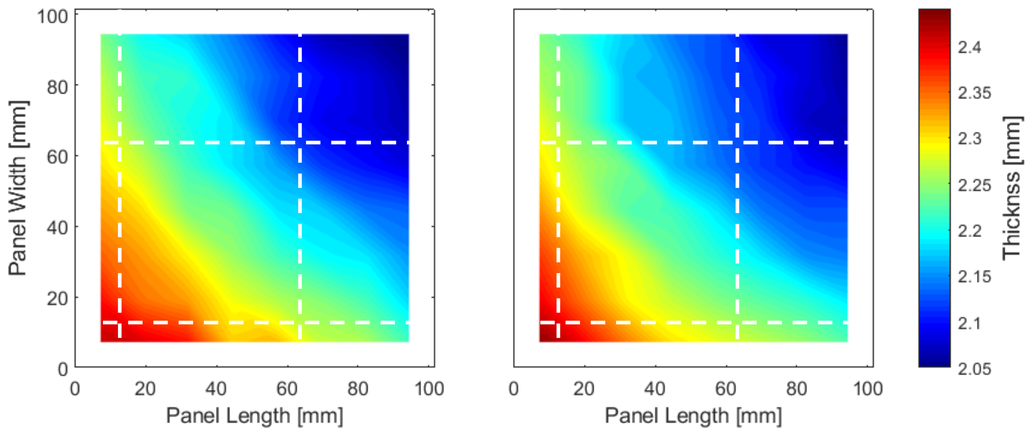

Figure C. 10: Thickness distribution in parts made with square strands to be 2.3 mm thick.